JETP Letters, Vol. 71, No. 9, 2000, pp. 351–354. Translated from Pis'ma v Zhurnal Éksperimental'noĭ i Teoreticheskoĭ Fiziki, Vol. 71, No. 9, 2000, pp. 513–518.

Attosecond High-Temperature Subnanometer Single Electronics on Transition-Metal Atoms

E. S. Demidov

Nizhni Novgorod State University, pr. Gagarina 23, Nizhni Novgorod, 630600 Russia

e-mail: ett@phys.unn.runnet.ru

Received March 14, 2000

Discrete electron tunneling through transition-metal atoms is considered. It is emphasized that a metal grain in the known single-electron systems can be replaced by a *d*- or *f*-atom. A response speed within the attosecond range, a working temperature on the order of the melting point of refractory substances, and an atomic level of integration are attainable in this case. Experimental realizations of single-electron solid-state structures with *d*- or *f*-atoms are discussed. © *2000 MAIK "Nauka/Interperiodica".*

PACS numbers: 73.40.Gk

The discrete tunneling of electrons (or holes) restricted by a Coulomb blockade attracts attention, because the features of current transport under conditions of significant unaveraged electron–electron interaction are far from being well understood. From the applied point of view, theoretical and experimental studies already made [1, 2] indicate that single electronics, together with high-temperature superconductivity promises to become the basis for the next generation of microelectronics. This future microelectronics will be nanoelectronics or quantum electronics characterized by limiting values of parameters [1] surpassing those of present-day semiconductor electronics: femtosecond response speed $\approx 10^{-14}$ s, nanosized level of integration, and extremely small expenditures of energy in recording an information bit. However, like up-to-date high-temperature superconductivity, the structures discussed and studied up to now that possess discrete tunneling through conducting (metal or semiconductor) grains embedded in a dielectric medium between metal plates are characterized by a finite temperature limit, which hardly reaches room temperature. Thus, according to the estimates [1], the limiting temperature for metal grains about 3 nm in diameter and 0.3 aF in capacitance is 60 K for a memory with data retention time of 10^5. This letter calls attention to the possibility of substantially extending the frequency, temperature, and size limits of single electronics if transition-metal atoms with partially filled *d* or *f* shells in a dielectric medium are used instead of conducting grains of thousands of metal atoms. In the case of rare-earth elements, the frequency limit is in the attosecond triad of orders and the working temperature is of the order of melting points of refractory substances. Extending the area of studying discrete electron tunneling many times through taking into consideration transition-metal atoms increases the probability that the charge oscillations caused by the Coulomb blockade will be detected directly through emission of electromagnetic waves. It should be noted that the prospects for the advance of single electronics to a molecular level were considered in [1].

The possibility of replacing a conducting grain in a dielectric medium with a transition-metal atom or ion is based on an intimate relationship between the properties of a granulated medium and those resulting from the Hubbard model of substances with narrow bands and strong electron correlation effects (characteristic of media containing elements with partially filled *d* or *f* shells), as was already mentioned in the pioneering work [3].

Consider M–G–M and M–A–M systems in which a metal grain G or atom A is placed between two metal sides M1 and M2. As in [3], the total Hamiltonian of the system is represented as a sum of three terms

$$H = H_0 + H_C + H_T, \tag{1}$$

where H_0 is the Hamiltonian of the set of noninteracting bodies; H_C is the correlation contribution of the Coulomb interaction, which, in the general case, does not depend on the voltage V applied across M1 and M2; and H_T is the tunneling term. It is evident that

$$H_0 = H_{01} + H_{02} + H_{0G,0A}, \tag{2}$$

where the first and the second terms are, respectively, the contributions from M1 and M2 and the last term is the Hamiltonian of a free grain or atom.

For an isolated grain, according to [3],

$$H_{0G} + H_{CG} = \frac{e^2}{2C_G}\left(\sum_\alpha b_\alpha^+ b_\alpha - N_0\right)^2, \tag{3}$$

0021-3640/00/7109-0351$20.00

where C_G is the capacitance of an isolated grain; b_α^+ and b_α are the creation and annihilation operators of particles in a grain; α is the set of electron quantum numbers, including spin; and N_0 is the equilibrium number of particles satisfying the neutrality condition. Hamiltonian (3) gives the following expression for the energy of an isolated grain as a function of the number of electrons n and the charge $Q = ne$:

$$E_n = \frac{e^2 n^2}{2C} - An + \text{const} = \frac{Q^2}{2C} - An + \text{const}, \quad (4)$$

where A is the work function of the grain metal.

If the dependence of the tunneling probability on the quantum states is neglected, the term H_T in (1) takes the standard form

$$H_T = T_1 \sum_{p\alpha} (\alpha_{1p}^+ b_\alpha + b_\alpha^+ a_{1p}) + T_2 \sum_{q\alpha} (\alpha_{2q}^+ b_\alpha + b_\alpha^+ a_{2q}), \quad (5)$$

where a_1^+ and a_2^+ are the creation operators of electrons in M1 and M2, respectively; and p and q, as well as α, are sets of quantum numbers. Conventional tunneling takes place at $H_T \gg H_C$ or $T_1, T_2 \gg Q^2/2C$, and single-electron Coulomb blockade occurs at $H_T \lesssim H_C$.

Like a grain in Eq. (3), the Hamiltonians of an isolated atom with an unfilled shell and with the binding energy E_d of an electron in this shell with the atomic core can also be represented as a sum of two terms in the form [4]

$$H_{0A} + H_{CA} = \sum_{\alpha\sigma} E_d \hat{n}_{\alpha\sigma} + \frac{1}{2}\sum_{\alpha\beta\sigma} (U_{\alpha\beta} - J_{\alpha\beta}) \hat{n}_{\alpha\beta}\hat{n}_{\beta\sigma} + \frac{1}{2}\sum_{\alpha\beta\sigma} U_{\alpha\beta}\hat{n}_{\alpha\sigma}\hat{n}_{\beta,-\sigma}, \quad (6)$$

where the operator of the number of electrons in the shell $\hat{n}_{\alpha\sigma} = b_{\alpha\sigma}^+ b_{\alpha\sigma}$, α and β are sets of (orbital and magnetic) quantum numbers, σ is the spin number, $U_{\alpha\beta}$ is the correlation energy of the electron Coulomb interaction, and $J_{\alpha\beta}$ is the correlation energy of the electron exchange interaction.

Considering that the exchange interaction is small compared to the Coulomb interaction (according to [4], $J \sim 4\%U$ for $3d$ elements and $J \sim (8\text{–}15)\%U$ in a crystal), one may neglect it and obtain within the conventional Hartree–Fock approximation

$$H_{0A} + H_{CA} = E_d \hat{n} + \frac{1}{2} U \hat{n}(\hat{n} - 1). \quad (7)$$

This equation gives the following dependence of the atomic energy on the occupation n of the shell:

$$E_n = nE_{d0} + \frac{1}{2}Un(n-1) + \text{const}, \qquad E_{d0} = E_d + n_0 U, \quad (8)$$

where n_0 is the initial equilibrium occupation of the shell, determined by the Fermi level.

Remarkable properties of transition elements that provide their metal-like behavior (like a metal grain) are as follows: (1) relatively large range of n, up to 10 in the d shell and 14 in the f shell; (2) starting from the valence 2+ and up (which commonly occurs in d and f atoms in crystals), U weakly depends on n and equals about 20 eV on average for free atoms of iron, palladium, and platinum groups and for $4f$ rare-earth metals [4, 6]; (3) as distinct from s and p shells, d and f electrons in a crystal retain their characteristic properties, in particular, a small radial extent; (4) d and f ions have a rich spectrum of excited states of intra-atomic electronic transitions starting from an energy $\ll U$.

Because of item (2) and Eq. (8), E_n almost quadratically depends on n, as in Eq. (4) for a grain. According to Eq. (8), the atomic "capacitance" equals

$$C = \partial^2 E / \partial Q^2 \big|_{Q = Q_0} = e^2/U, \quad (9)$$

where $Q = en$ and $Q_0 = en_0$. According to a comparison between Eqs. (4) and (8), the part of the atomic work function is played by the quantity

$$A_a = -E_{d0} + U/2. \quad (10)$$

For a given n_0, the Fermi level equals the work function of the metal of the plates, $F = -A_M$, and must lie in the range $A_a \pm U/2$. At $A_M \approx A_a$, the contribution of $n_0 A_a$ to Eq. (8) is compensated in an M–A–M system by the term $n_0 F$, which ensures proximity of the energies of the $en_0 + e/2$ and $en_0 - e/2$ states and, thus, the energy degeneration required for one-electron oscillations.

The tunneling Hamiltonian of form (5) is commonly used in the consideration of electron exchange between transition-metal atoms in the Hubbard model, and it can be applied on the same grounds to the M–A–M system. Thus, the M–G–M and M–A–M systems have similar starting mathematical descriptions and, hence, similar kinetics, whereas current transport through single atoms of d and f elements or sequential chains of such atoms can be considered to be of interest to single electronics. Because an atom, compared to a grain, is characterized by a larger correlation energy U and a smaller "capacitance" (9), the temperature and frequency limits in this case become considerably more extended.

Let us make estimates of the temperature and frequency limits for the M–A–M structure. As the time limit, the response time can be chosen:

$$\tau_0 = R_Q C, \quad R_Q = \pi\hbar/2e^2 \approx 6.5\ \text{k}\Omega. \quad (11)$$

In this case, $H_T \approx 0.6H_C$ and the working temperature

$$T_w = \Delta E/\beta \cdot \kappa_B, \quad \beta = 50 \ [1]. \tag{12}$$

It is natural that the smallest τ_0 and the greatest T_w are formally obtained for a purely speculative system of two metal plates with a vacuum gap, in the middle of which an atom is placed. For example, $\Delta E = U \approx 10$ eV between the second and third ionization potentials for rare-earth metals of the 4*f* series. According to Eqs. (9), (11), and (12), this value of U gives $C \approx 1.6 \times 10^{-20}$ F, $\tau_0 \approx 100$ as, and $T_w \approx 2.2 \times 10^3$ K. However, not only is this structure technically unfeasible but a suitable metal is absent in nature, which presents a physically insuperable obstacle. The second ionization potential corresponds to $E_{d0} = -10$ eV, and, according to Eq. (10), the metal of the contact plates M–A–M must have the work function $A_M \approx 15$ eV in order to provide the necessary occupation of the 4*f* shell.

The M–A–M structure, in which an atom is embedded in a dielectric layer between metal plates, corresponds to a quite real situation. According to calculations [5], for substitutional 3*d* atoms in diamond-type crystals, starting from iron, the charge state 3+ corresponds to the effective value $U \approx 1$ eV and $E_{d0} \approx -5$ eV with regard to crystal polarization. From here, it follows that $\tau_0 \approx 1000$ as, $T_w \approx 220$ K, and $A = 5.5$ eV; that is, the metal work function is quite realistic. The attosecond triad of orders in τ_0 can be reached using atoms of rare-earth 4*f* metals in a dielectric matrix. According to calculations [6], $U \approx 2.5$ eV and $E_{d0} \approx -7$ eV for triply charged substitutional ions in diamond-type crystals. In this case, $\tau_0 \approx 400$ as and $T_w \approx 560$ K. In dielectrics with lower polarizability, one should expect an increase in U by a factor of 1.5–2 and the corresponding increase in the response time limit. However, in this case, plates of a metal with an extremely high work function of 7–8 eV are necessary in the systems with a rare-earth metal. It is possible that metals with heavy fermions like $CeCu_6$, $CeCu_2Si_2$, or Upt_3 possess this property [7]. In both cases, the dielectric must have a band gap larger than U and the top of valence band must lie at a depth larger than A in reference to the vacuum zero of electrons. However, these restrictions can be weakened because of dimensional quantization of electrons in a subnanometer dielectric layer. In order that an M–A–M contact should exhibit electron oscillations, the value of β in Eq. (12) may probably be 5–10 times smaller and, respectively, T_w may be of the order of the highest melting points of refractory substances.

There is no need for one-by-one stacking of atoms in order to verify that M–A–M contacts are feasible, although advances have been already made in this field using a microprobe technique. A quite feasible structure can presently be manufactured. A metal layer is sputtered onto a smooth substrate and is coated with a dielectric layer several tenths of nanometer thick. Next, less than a monoatomic layer of *d* or *f* atoms is sputtered, which is then coated with a dielectric layer several tenths of nanometer thick and is finally sputtered with the second metal layer. The distance between *d* or *f* atoms must be larger than the total thickness of the dielectric. As a result, a heterostructure with a multitude of parallel-connected M–A–M junctions will be obtained. The metal coatings may serve as a waveguide or a Fabry–Perot resonator.

Another variant is a tunneling *p–n* junction in a semiconductor with transition-metal impurities. It is quite possible that the inflection points observed previously in the current–voltage characteristics of GaAs tunnel diodes with impurities of the iron group [8] were just evidence of discrete electron tunneling with retention on 3*d* ions in the spatial-charge region of the tunneling *p–n* junction. It is also not improbable that an alternate reason for the inflection points in the current–voltage characteristics of silicon diodes with an interlayer of porous silicon [9] was the presence of 3*d* ions of the iron group in the porous layer.

In the 3D variant, of interest are Hubbard systems, in which one-electron oscillations may be an alternative to the electron–phonon mechanism of current energy dissipation in a conductor. First of all, these are compounds in which anions (for example, oxygen ions in oxides) block the outer *s* electrons of atoms and the current is transferred by *d* and *f* electrons. However, metals with heavy fermions are also of interest. Anisotropic crystals with a chain arrangement of *d* and *f* atoms with a current along chains are preferable. Studies of deviations of a conductor with a current from the blackbody radiation in both the spectrum and the possible spontaneous polarization are of importance in this case. Optical one-electron emission can really occur only in a film or filamentary conductor with good heat removal and in the regime of very short current pulses. In a metal with a conventional transversal atomic density $N_a \approx 10^{15}$ cm^{-2} at $I_a/e \approx 6 \times 10^{14}$ Hz ($\lambda = 0.5$ μm), a supergiant current density $j = I_a N_a \approx 10^{11}$ A/cm^2 is necessary. A conductor explosion will not occur unless the current pulse duration is shorter than the minimum period of atomic oscillations $\approx 10^{-12}$ s.

Note in conclusion that the numerical values of the parameters given above are only estimations. Because of the stringent requirements on the work function of the metal plates of the M–A–M tunneling junction, calculations of higher accuracy are necessary. These refinements with regard to the multilayer structure of *d* and *f* shells or within the so-called extended Hartree–Fock approximation and with more accurate accounting for the polarization effect of the valence electrons of the dielectric [4–6] will be presented in another communication. Nevertheless, it is clear that searching for metals with a record-breaking high work function is required in order to make progress in the region of optical emission of contacts with discrete electron tunneling.

REFERENCES

1. K. K. Likharev, Mikroélektronika **16**, 195 (1987).
2. I. I. Abramov and E. G. Novik, Fiz. Tekh. Poluprovodn. (St. Petersburg) **33**, 1388 (1999) [Semiconductors **33**, 1254 (1999)].
3. O. I. Kulik and R. I. Shekhter, Zh. Éksp. Teor. Fiz. **68**, 623 (1975) [Sov. Phys. JETP **41**, 308 (1975)].
4. E. S. Demidov, Fiz. Tverd. Tela (St. Petersburg) **34**, 37 (1992) [Sov. Phys. Solid State **34**, 18 (1992)].
5. E. S. Demidov, in *Proceedings of X Feofilov Symposium on Spectroscopy of Crystals, Activated Ions of Rare-Earth and Transition Metals (St. Petersburg, 1995)*, p. 97.
6. E. S. Demidov, in *Proceedings of International Conference on Optics of Semiconductors (Ul'yanovsk State Univ., Ul'yanovsk, 1998)*, p. 135.
7. F. Steglich *et al.*, Phys. Rev. Lett. **43**, 1892 (1979).
8. V. I. Fistul' and A. M. Agaev, Fiz. Tverd. Tela (Leningrad) **7**, 3042 (1965) [Sov. Phys. Solid State **7**, 2461 (1965)]; Fiz. Tverd. Tela (Leningrad) **7**, 3691 (1965) [Sov. Phys. Solid State **7**, 2988 (1965)].
9. E. S. Demidov, V. V. Karzanov, and V. G. Shengurov, Pis'ma Zh. Éksp. Teor. Fiz. **67**, 794 (1998) [JETP Lett. **67**, 839 (1998)].

Translated by A. Bagatur'yants

JETP Letters, Vol. 71, No. 9, 2000, pp. 355–358. Translated from Pis'ma v Zhurnal Éksperimental'noĭ i Teoreticheskoĭ Fiziki, Vol. 71, No. 9, 2000, pp. 519–523.

The $e^+e^- \longrightarrow \pi^0\pi^0\gamma$ Process below 1.0 GeV

M. N. Achasov, K. I. Beloborodov, A. V. Berdyugin, A. G. Bogdanchikov, A. V. Bozhenok, A. D. Bukin, D. A. Bukin, S. V. Burdin, A. V. Vasil'ev, D. I. Ganyushin, V. B. Golubev, T. V. Dimova, A. A. Drozdetskiĭ, V. P. Druzhinin*, P. M. Ivanov, V. N. Ivanchenko, A. A. Korol', M. S. Korostelev, S. V. Koshuba, G. A. Kukartsev, E. V. Pakhtusova, A. A. Polunin, E. É. Pyata, A. A. Sal'nikov, S. I. Serednyakov, V. A. Sidorov, Z. K. Silagadze, V. V. Sharyĭ, and Yu. M. Shatunov

Budker Institute of Nuclear Physics, Siberian Division, Russian Academy of Sciences, pr. Akademika Lavrent'eva 11, Novosibirsk, 630090 Russia

Novosibirsk State University, ul. Pirogova 2, Novosibirsk, 630090 Russia

**e-mail: druzhinin@inp.nsk.su*

Received March 22, 2000

The $e^+e^- \longrightarrow \pi^0\pi^0\gamma$ reaction was studied in the energy range 0.36–0.97 GeV on a VEPP-2M e^+e^- collider with an SND detector. The decay probabilities were found to be $B(\omega \longrightarrow \pi^0\pi^0\gamma) = (7.8 \pm 2.7 \pm 2.0) \times 10^{-5}$ and $B(\rho \longrightarrow \pi^0\pi^0\gamma) = (4.8^{+3.4}_{-1.8} \pm 0.2) \times 10^{-5}$. © *2000 MAIK "Nauka/Interperiodica".*

PACS numbers: 13.65.+i; 14.40.Cs

This paper is devoted to the study of reaction

$$e^+e^- \longrightarrow \pi^0\pi^0\gamma \qquad (1)$$

at e^+e^- center of mass energy $E < 1$ GeV. In the vector dominance model, this process is described by the $\rho^0 \longrightarrow \omega\pi^0$ and $\omega \longrightarrow \rho^0\pi^0$ transitions followed by the $\rho^0, \omega \longrightarrow \pi^0\gamma$ decay. The model yields values of 1.0×10^{-5} and 2.8×10^{-5} [1] for the decay probabilities of the ρ^0- and ω-mesons, respectively. The electric dipole transition to the scalar $\pi^0\pi^0$ state is an alternative mechanism of the $\rho, \omega \longrightarrow \pi^0\pi^0\gamma$ decays. This mechanism was considered in [2, 3] in the framework of the chiral perturbation theory with the inclusion of pion and kaon loops. The value of $\sim 10^{-5}$ obtained for the pion-loop contribution in the case of the ρ-meson is comparable with the amplitude of the $\omega\pi^0$ mechanism; for the ω-meson, the contributions of the pion loops are suppressed due to G-parity conservation and therefore are negligible. Since the $\rho, \omega \longrightarrow \pi^0\pi^0\gamma$ decay probabilities are low, experimental data on reaction (1) in the range $E < 1$ GeV are virtually lacking. The only measured decay probability, $B(\omega \longrightarrow \pi^0\pi^0\gamma) = (7.2 \pm 2.5) \times 10^{-5}$ [4], is almost three times higher than the vector dominance prediction. There is no theoretical explanation of this discrepancy.

In this paper, an analysis is carried out of the experimental data collected in 1998 at a VEPP-2M e^+e^- collider with an SND detector [5] in the energy range $E =$ 360–970 MeV. The accumulated integrated luminosity of 3.6 pb^{-1} corresponded to the production of approximately 1.2×10^6 ω-mesons and 2×10^6 ρ-mesons.

Five-photon events with energy deposition higher than $0.7E$ in a calorimeter and with the total momentum smaller than $0.15E$, measured by the calorimeter, were selected for analysis. High rate of the beam background resulted in the appearance of extra photons in 4% of the events. As a result, some true events were lost and the additional background appeared from the $e^+e^- \longrightarrow 2\gamma$, 3γ, and 4γ processes. The superpositions of the beam background were analyzed for the events recorded with trigger from an external generator. The information on the fired detector channels was used for modeling the process of interest and the background processes in order to simulate the superpositions occurring in the real experiment. A considerable suppression of the background due to the spurious photon events was achieved by imposing the $E_{\min} > 30$ MeV and $30° < \theta_{\min} < 150°$ constraints on the energy and the polar angle of the smallest energy photon in an event. Another background source is the $e^+e^- \longrightarrow \eta\gamma \longrightarrow 3\pi^0\gamma \longrightarrow 7\gamma$ reaction whose events become five-photon mainly due to the merging of neighboring photons. To suppress this background, the parameter χ_γ was used, which characterized the transverse energy deposition profile of the detected photon showers [6]. The restriction $\chi_\gamma < 5$ halves the background from the $e^+e^- \longrightarrow \eta\gamma$ process, with a 5% loss of the true five-photon events.

Further selection was carried out through the kinematic reconstruction of the events. Compatibility of the kinematics of an event with the hypotheses for its belonging to the $e^+e^- \longrightarrow 5\gamma$ and $e^+e^- \longrightarrow 3\gamma$ processes was checked. When checking the second hypothesis,

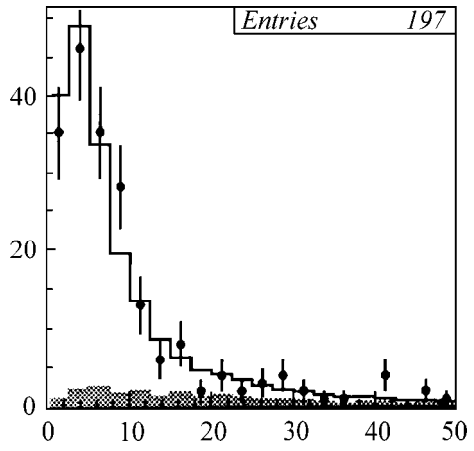

Fig. 1. Distribution over the $\chi_{5\gamma}$ parameter. The points with error bars are the experimental data. The histogram is the sum of events simulated for process (1) and background processes. The shaded histogram is the contribution of the background processes.

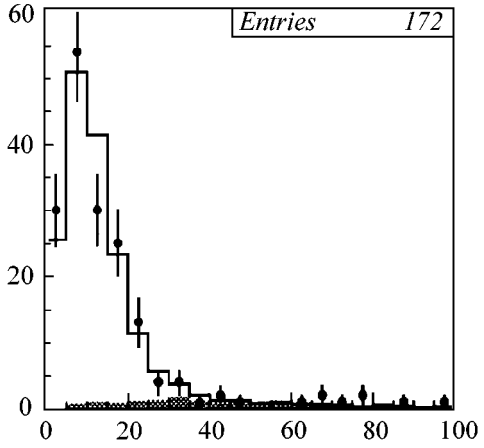

Fig. 2. Distribution over the $R_{\min}$ parameter (MeV). The points with error bars are the experimental data. The histogram is the sum of events simulated for process (1) and background processes. The shaded histogram is the contribution of the background processes.

two of five photons were treated as spurious. As a result of kinematic reconstruction, the χ^2 values, $\chi_{5\gamma}$ and $\chi_{3\gamma}$, were calculated for both hypotheses. The $\chi_{3\gamma} < 20$ restriction completely excludes the background caused by the $e^+e^- \longrightarrow 2\gamma, 3\gamma$ processes, with the loss of only 2.5% of the events for the process under consideration. Figure 1 shows the $\chi_{5\gamma}$ distribution of the experimental and simulated events. This parameter was constrained to be $\chi_{5\gamma} < 20$.

The ultimate selection was carried out on the condition that the event involves two π^0-mesons. For each of the 15 pairs of two-photon invariant masses (m_{1i}, m_{2i}) possible for a five-photon event, the quantity

$$R_i = \sqrt{(m_{1i} - m_{\pi^0})^2 + (m_{2i} - m_{\pi^0})^2}$$

was calculated. The quantity $R_{\min} = \min(R_1, R_2, \ldots, R_{15})$ was used as a selection parameter. Figure 2 demonstrates the $R_{\min}$-distribution for the events selected according to the above criteria, the distribution of the events simulated for process (1), and the calculated background. The restriction $R_{\min} < 25$ was imposed on the parameter $R_{\min}$.

A total of 153 events satisfying the above-listed conditions were selected with the calculated background of 3 ± 1 events. The background resulted from the $e^+e^- \longrightarrow \eta\gamma$ and $e^+e^- \longrightarrow 4\gamma$ processes. The selected events are mainly concentrated in two energy ranges: 63 events near the ω-meson and 83 events in the range 920–970 MeV. Figure 3 shows the photon spectrum of the events selected for the $e^+e^- \longrightarrow \pi^0\pi^0\gamma$ reaction in the ω-resonance region 760–800 MeV. The spectrum shape agrees well with the calculation for the $\rho \longrightarrow \omega\pi$ and $\omega \longrightarrow \rho^0\pi^0$ mechanisms, although the number of experimental events far exceeds the number predicted by this model. The angular distributions of photons and π^0-mesons also exhibit no appreciable deviations from the calculation. Nevertheless, because of the strong interference of all mechanisms under discussion, one cannot rule out even a considerable (~50%) contribution of the intermediate scalar state to the amplitude of the ω-meson decay at the available statistical level. The 920–970 MeV region is above the $e^+e^- \longrightarrow \omega\pi^0$ reaction threshold; the expected number of events and distribution in kinematic parameters agree with this model.

The cross section of the $e^+e^- \longrightarrow \pi^0\pi^0\gamma$ reaction for each energy point was calculated as $\sigma = N/\varepsilon L(1 + \delta)$, where N and L are the number of events and the integrated luminosity, respectively; ε is the detection efficiency; and δ is the radiative correction [7]. The detection efficiency for reaction (1) was calculated by simulation. The calculation was carried out making use of the differential cross section for the $e^+e^- \longrightarrow \pi^0\pi^0\gamma$ process in the vector dominance model [8]. The detection efficiency weakly depends on the energy and is equal to 27–30%. A systematic error of the detection efficiency, including the model error due to the possible contribution of the scalar state, is estimated at 10%. Figure 4 demonstrates the energy dependence of the resulting cross section. No events were detected below 650 MeV. To approximate the cross section, the amplitude of the $e^+e^- \longrightarrow \pi^0\pi^0\gamma$ process was parameterized as

$$A_{\pi\pi\gamma} = A_{\rho \to \omega\pi} + \beta A_{\rho \to S\gamma} + \alpha A_{\omega \to \pi^0\pi^0\gamma}, \qquad (2)$$

where $A_{\rho \to \omega\pi}$ and $\beta A_{\rho \to S\gamma}$ are the amplitudes of the ρ-meson decay through the intermediate ωπ [8] and scalar $S\gamma$ [2] states, respectively, and αA_ω is the ampli-

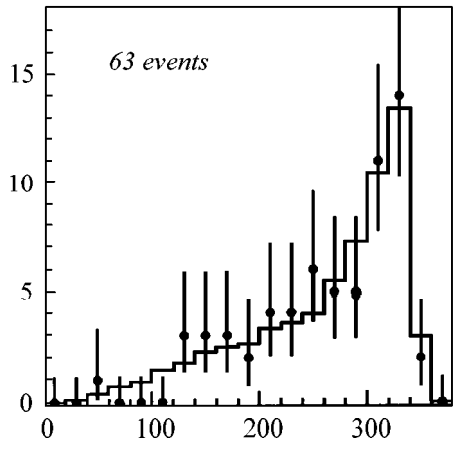

Fig. 3. Photon spectrum (energy in MeV) for the experimental events of reaction (1) from the ω-resonance region (points with error bars) and the result of simulation in the vector dominance model (histogram).

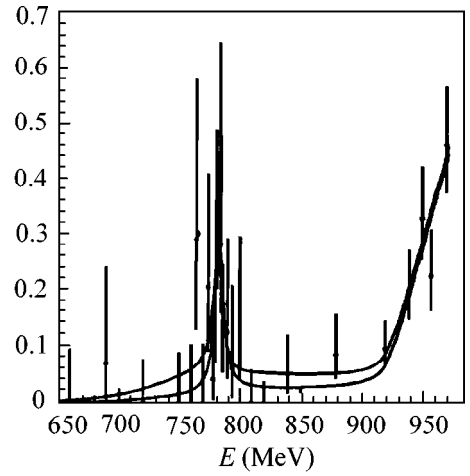

Fig. 4. Cross section (nb) for the $e^+e^- \longrightarrow \pi^0\pi^0\gamma$ reaction. The points with error bars are the experimental data. The curves are the results of approximation in the two models described in the text.

tude of the $\omega \longrightarrow \pi^0\pi^0\gamma$ decay. The parameters for the $A_{\rho \to \omega\pi}$ amplitude were extracted from the data on the $e^+e^- \longrightarrow \rho, \rho' \longrightarrow \omega\pi$ process at energies above 1 GeV [9]. This amplitude is determined by the coupling constant $g_{\rho\omega\pi}$, which was varied from 15.5 to 16.1 GeV^{-1}, depending on the ρ'-meson parameters. If the contribution of the ρ'-meson is disregarded, the $g_{\rho\omega\pi}$ constant could be determined without invoking the data for the energy range above 1 GeV: 15.5 ± 1.2 GeV^{-1}. The complex multiplier β in the transition amplitude via the scalar state was determined in the course of approximation. The amplitude was normalized in such a way that the probability of $\rho \longrightarrow S\gamma \longrightarrow \pi^0\pi^0\gamma$ decay was equal to 10^{-5} at $|\beta| = 1$. To estimate the model dependence for the α parameter, two mechanisms were considered for the $\omega \longrightarrow \pi^0\pi^0\gamma$ decay: the pure $\rho^0\pi^0$ transition and the sum of intermediate states $\rho^0\pi^0$ and $\sigma\gamma$, where σ is the 600-MeV scalar resonance with a width of 400 MeV. In the latter case, the calculated $\rho^0\pi^0$ contribution was used [1]. The amplitude was normalized so that $|\alpha| = 1$ corresponded to the tabulated value of the $\omega \longrightarrow \pi^0\pi^0\gamma$ decay probability [4].

Figure 4 shows the cross sections for the $e^+e^- \longrightarrow \pi^0\pi^0\gamma$ process approximated in the two models. The lower curve corresponds to the model ignoring the contribution of $\rho \longrightarrow \pi^0\pi^0\gamma$ decay through the scalar state; i.e., $\beta = 0$. The resulting $|\alpha| = 1.33 \pm 0.12 \pm 0.04$ corresponds to $B(\omega \longrightarrow \pi^0\pi^0\gamma) = (12.7 \pm 2.3 \pm 0.8) \times 10^{-5}$. The first and second errors are statistical and systematic, respectively. The main contribution to the systematic error comes from the difference between the results obtained for the two above-described assumptions about the ω-decay mechanism. The decay probability exceeds the tabulated value by 1.5 standard deviations. For this model, $P(\chi^2) = 5\%$.

The upper curve in Fig. 4 was obtained for the model in which the parameter β was determined in the course of approximation. This hypothesis agrees much better with the experimental data: $P(\chi^2) = 24\%$. The introduction of an additional amplitude $\rho \longrightarrow S\gamma$ considerably increases the errors of parameter $|\alpha| = 1.04 \pm 0.18 \pm 0.13$. Although the parameter $|\beta| = 1.4^{+1.4}_{-0.5} \pm 0.1$ is determined with an accuracy of ~100%, it differs from zero by 2.5 standard deviations. For this reason, the parameters of the second model are presented as a final result. The resulting $\omega \longrightarrow \pi^0\pi^0\gamma$ decay probability

$$B(\omega \longrightarrow \pi^0\pi^0\gamma) = (7.8 \pm 2.7 \pm 2.0) \times 10^{-5} \qquad (3)$$

is three times as great as the value calculated in the vector dominance model of the $\rho^0\pi^0$ mechanism [1] and confirms the only known measurement $B(\omega \longrightarrow \pi^0\pi^0\gamma) = (7.2 \pm 2.5) \times 10^{-5}$ [4]. The results of the approximation can be regarded as evidence for the existence of $\rho \longrightarrow S\gamma \longrightarrow \pi^0\pi^0\gamma$ decay. The $B(\rho \longrightarrow S\gamma \longrightarrow \pi^0\pi^0\gamma) = (1.9^{+6.0}_{-1.2}) \times 10^{-5}$ value obtained for the decay probability in this mechanism is of the same order of magnitude as the result $(1.0–1.4) \times 10^{-5}$ calculated in the chiral models [2, 3]. The total probability of ρ-meson decay through both mechanisms ($\omega\pi^0$ and $S\gamma$) is equal to

$$B(\rho \longrightarrow \pi^0\pi^0\gamma) = (4.8^{+3.4}_{-1.8} \pm 0.2) \times 10^{-5}. \qquad (4)$$

This is the first measurement of the $\rho \longrightarrow \pi^0\pi^0\gamma$ decay probability.

This work was supported by the STP Foundation "Integration" (grant no. 274) and by the Russian Foundation for Basic Research, project no. 00-02-17481.

REFERENCES

1. A. Bramon, A. Grau, and G. Pancheri, Phys. Lett. B **283**, 416 (1992).
2. A. Bramon, A. Grau, and G. Pancheri, Phys. Lett. B **289**, 97 (1992).
3. E. Marco, S. Hirenzaki, E. Oset, and H. Toki, Phys. Lett. B **470**, 20 (1999).
4. D. Alde, F. G. Binon, M. Boutemeur, *et al.*, Phys. Lett. B **340**, 122 (1994).
5. M. N. Achasov, V. M. Aulchenko, S. E. Baru, *et al.*, hep-ex/9909015 [Nucl. Instrum. Methods Phys. Res. (in press)].
6. A. V. Bozhenok, V. N. Ivanchenko, and Z. K. Silagadze, Nucl. Instrum. Methods Phys. Res. Sect. A **379**, 507 (1996).
7. E. A. Kuraev and V. S. Fadin, Yad. Fiz. **41**, 733 (1985) [Sov. J. Nucl. Phys. **41**, 466 (1985)].
8. M. N. Achasov, V. M. Aulchenko, A. V. Berdyugin, *et al.*, Nucl. Phys. B **569**, 158 (2000).
9. V. M. Aulchenko, M. N. Achasov, K. I. Beloborodov, *et al.*, Zh. Éksp. Teor. Fiz. (in press) [JETP (in press)].

Translated by R. Tyapaev

JETP Letters, Vol. 71, No. 9, 2000, pp. 359–361. Translated from Pis'ma v Zhurnal Éksperimental'noĭ i Teoreticheskoĭ Fiziki, Vol. 71, No. 9, 2000, pp. 524–527.

The Use of Quasielastic Pion–Proton Backward Scattering at 0.7 GeV/*c* for Studying Fermi Motion in Light Nuclei

B. M. Abramov, Yu. A. Borodin, S. A. Bulychjov, I. A. Dukhovskoy, A. P. Krutenkova, V. V. Kulikov, M. A. Matsyuk, I. A. Radkevich, E. N. Turdakina, and A. I. Khanov

Institute of Theoretical and Experimental Physics, Bol'shaya Cheremushkinskaya ul. 25, Moscow, 117259 Russia
e-mail: turdakina@vxitep.itep.ru

Received March 23, 2000

The plane-wave approximation was used to examine the proton Fermi-momentum distribution in experiments on quasielastic large-momentum-transfer pion–nucleon scattering in light nuclei ^{6}Li, ^{7}Li, and ^{12}C. It was found that, unlike the (*e*, *e*') reaction, the Fermi-gas model is in poor agreement with experiment, whereas the oscillator model adequately describes the spectrum shape. However, the parameters obtained for these distributions are sizably smaller than those derived from the (*e*, *e*') experiments. This suggests that the plane-wave approach is inadequate and that more complicated theoretical approaches, supposedly allowing for pion–nucleon amplitude modification in nuclear matter, are necessary for the analysis of experimental data. © *2000 MAIK "Nauka/Interperiodica".*

PACS numbers: 25.80.Hp

In recent years, considerable interest has arisen in the problem of modification of the interaction between elementary particles in nuclear matter. This was primarily initiated by the development of a new theoretical approach [1] to the calculation of the so-called "collision broadening" of baryon resonances interacting with nucleons in nuclear matter. An analysis of the new data on the total cross section for the interaction of tagged photons with nuclei lent serious support to the validity of this approach. Other interactions have yet to be tested. The quasielastic pion nuclear backward scattering in nuclei at resonance energies seems to be rather promising in the search for the effects of modification of the interaction amplitude in nuclear matter. Indeed, due to the presence of baryon resonances and their interference with the nonresonant background, the differential cross section for large-angle pion scattering by a free nucleon strongly depends on the kinematic variables in the resonance energy range. With this in mind, we undertook a systematic experimental study of quasielastic pion–proton backward scattering from the protons in nuclei. The results of this experiment are of importance for testing the other models of pion interaction with bound nucleons, e.g., models allowing for the nonnucleonic components in the wave functions of bound nucleons. In this paper, the experimental setup is briefly described and the first results of an analysis of the Fermi-momentum distribution are presented for light nuclei.

The experiment was carried out in the accelerator of the Institute of Theoretical and Experimental Physics on a three-meter magnet spectrometer equipped with spark chambers. Nuclear targets were placed in the center of a magnet with magnetic-field volume of $3 \times 1 \times 0.5$ m, and the momenta of all reacting particles (beam pions, backward scattered pions, and forward knocked-out protons) were measured with a high accuracy (ca. 10 MeV/*c*) in the spark chambers. Protons were identified by the time of flight. Data were collected for three momenta of the incident negative pions, 0.7, 0.9, and 1.25 GeV/*c*, at angles from 145° to 180° in the CMS of pion–nucleon scattering by the following targets: H_2O, D_2O, ^{6}Li, ^{7}Li, and ^{12}C. Despite the fact that the backward cross section was small, the use of a large-aperture magnetic spectrometer and an intense pion beam from the accelerator of the Institute of Theoretical and Experimental Physics allowed a large amount of data (ca. 0.5 million triggers) to be collected. An important feature of the experiment was that the data were simultaneously collected for free protons in a water target. The experimental arrangement was close to the scheme presented in [2].

The angular and momentum correlation spectra were measured for the recoil proton and backward scattered pion. Since the differential cross section for quasielastic pion–proton scattering is a function of five variables (momentum and angle of the knocked-out proton and momentum and two angles of the scattered pion), it is natural to analyze these data by invoking certain models. An adequate choice of models and their parameters is the first step in such a treatment. We have performed an analysis in the plane-wave approximation, in which all observables are expressed through the nuclear spectral functions and the differential cross sections for elastic pion–proton scattering by a free nucleon. Insofar as the momentum vectors of the inci-

0021-3640/00/7109-0359$20.00

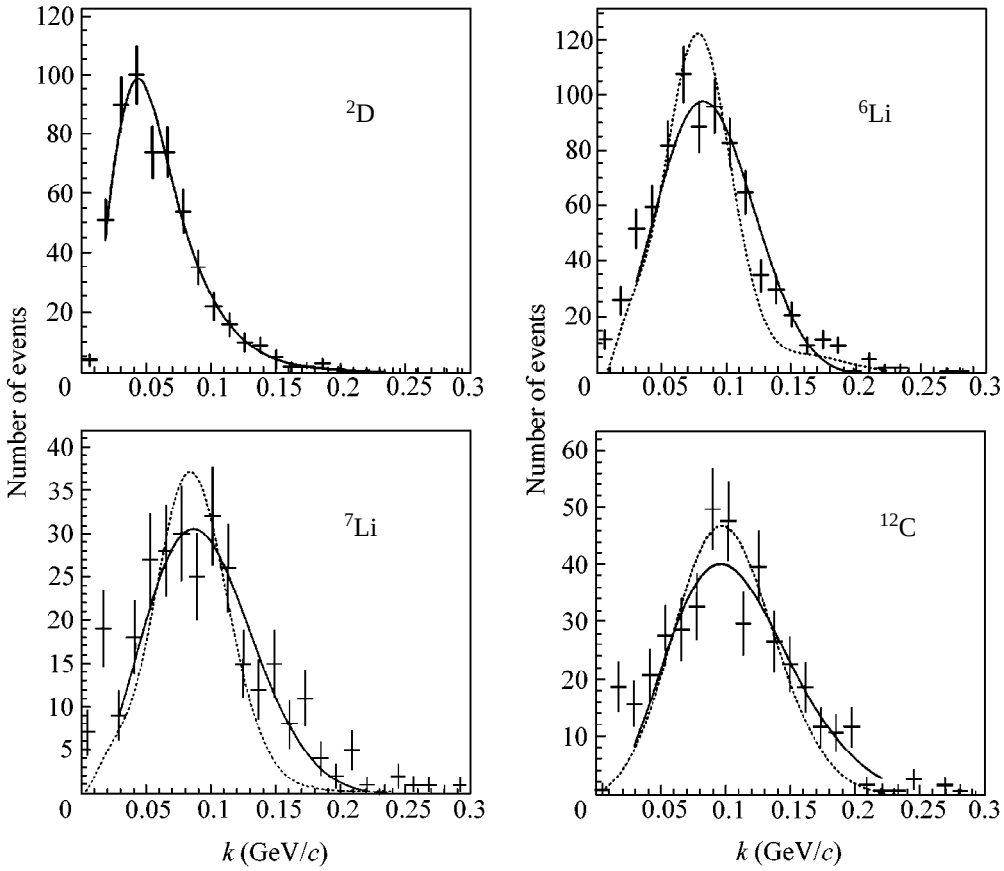

Experimental Fermi-momentum distributions and their description by the Hulthen wave function for ^{2}D (solid line) and the Fermi-gas (dotted lines) and oscillator (solid lines) models for ^{6}Li, ^{7}Li, and ^{12}C.

dent pion, recoil proton, and backward scattered pion are known in our experiment, the excitation energy of the residual nucleus and the momentum vector of the scattering intranuclear nucleon can be calculated for every event. A quasielastic peak with the width 30–40 MeV (for ^{6}Li–^{12}C) dominates in the excitation energy distributions for the residual nuclei at the experimental resolution of $\sigma = 12$ MeV. The resolution was determined from the data on hydrogen of the water target.

Fermi-momentum (MeV/c) distribution parameters

Nucleus	This experiment	Other measurements	Wave function
^{2}D	$\beta = 264 \pm 44$	260 ± 5 [4]	Hulthen
^{6}Li	$k_F = 96 \pm 16.0$	169 ± 5 [5]	Fermi gas
	$k_0 = 73 \pm 1.0$		Oscillator
^{7}Li	$k_F = 119 \pm 6.0$		Fermi gas
	$k_0 = 89 \pm 2.1$		Oscillator
^{12}C	$k_F = 137 \pm 3.2$	221 ± 5 [5]	Fermi gas
	$k_0 = 99 \pm 2.1$	131 [6]	Oscillator

The distributions of the probability $W(k)$ to observe a given Fermi-momentum magnitude k [$(W(k)dk = \epsilon(k)|\phi(k)|^2k^2dk$, where $\phi(k)$ is the nucleon wave function in the momentum representation and $\epsilon(k)$ is the efficiency of the apparatus] are presented in the figure for the ^{2}D, ^{6}Li, ^{7}Li, and ^{12}C nuclei. The solid line in the panel for ^{2}D shows the distribution calculated with the Hulthen wave function. The curves for the other nuclei are the ones best describing our data in the Fermi-gas (dotted line) and oscillator (solid line) models. The probability distribution in the oscillator model is taken in the form $|\phi(k)|^2 = [1 + 4/3(k/k_0)^2]\exp(-k^2/k_0^2)$, where k_0 is the model parameter. The parameters of the models best fitting our data are presented in the table together with the parameters derived from the (e, e') experiments. The Hulthen distribution parameter β [3] obtained for deuterium agrees well with the standard value $\beta = 260$ MeV/c. (The Hulthen distribution parameter α was fixed at $\alpha = 46$ MeV/c, because the sensitivity to this parameter is insignificant in the Fermi-momentum range studied.) Contrary to the (e, e') experiments, the Fermi-gas model for the other nuclei describes our data less adequately than the oscillator model does. Moreover, the distribution parameters for

both models are smaller than in the (*e*, *e*') experiments. Such a discrepancy may be due to the fact that the quasielastic pion–proton scattering is more peripheral, as compared to the (*e*, *e*') reaction. It is hoped that the more complicated calculations with a distorted-wave model allowing for the correlation of the Fermi momentum with the local nuclear density and pion and proton absorption in nuclear matter will better describe the data with the use of the standard model parameters. These calculations are also necessary for an analysis of the energy dependence of quasielastic pion–proton scattering, because it contains information about the modification of the pion–proton interaction amplitude in nuclear matter.

We are indebted to L.A. Kondratyuk for helpful discussions. This work was supported in part by the Russian Foundation for Basic Research, project no. 96-02-17617.

REFERENCES

1. N. Bianchi, E. De Sanctis, V. Muccifora, *et al.*, Nucl. Phys. A **579**, 453 (1994).
2. B. M. Abramov *et al.*, Nucl. Phys. A **542**, 579 (1992).
3. B. M. Golovin, G. I. Lykasov, A. M. Rozanova, *et al.*, Yad. Fiz. **16**, 1096 (1972) [Sov. J. Nucl. Phys. **16**, 602 (1973)].
4. A. Fridman, Fortschr. Phys. **23**, 243 (1975).
5. T. W. Donnelly and J. D. Walecka, Annu. Rev. Nucl. Sci. **25**, 329 (1975).
6. E. J. Moniz, Phys. Rev. **184**, 1154 (1969).

Translated by V. Sakun

JETP Letters, Vol. 71, No. 9, 2000, pp. 362–366. From Pis'ma v Zhurnal Éksperimental'noĭ i Teoreticheskoĭ Fiziki, Vol. 71, No. 9, 2000, pp. 528–533.

The Λ_b Lifetime in the Light Front Quark Model[1]

P. Yu. Kulikov, I. M. Narodetskiĭ*, and A. I. Onischenko

Institute of Theoretical and Experimental Physics, Bol'shaya Cheremushkinskaya ul. 25, Moscow, 117259 Russia

**e-mail: naro@heron.itep.ru*

Received March 30, 2000

The enhancement of the Λ_b decay width relative to B decay due to the difference in Fermi motion effects in Λ_b and B is calculated in the light front quark model with the simplifying assumption that Λ_b consists of a heavy quark and a light scalar diquark. In order to explain the large deviation from unity in the experimental result for $\tau(\Lambda_b)/\tau(B)$, it is necessary that the diquark be light and the ratio of the squares of the Λ_b and B wave functions at the origin be $\lesssim 1$. © *2000 MAIK "Nauka/Interperiodica".*

PACS numbers: 13.25.Hw; 13.30.-a; 14.20.Mr

The lifetimes of the b flavored hadrons H_b are related both to the CKM matrix elements $|V_{cb}|$ and $|V_{ub}|$ and to the dynamics of H_b decays. In the limit $m_b \longrightarrow \infty$, the light quarks do not affect the decay of the heavy quark and thus the lifetimes of all b hadrons must be equal. Taking account of the soft degrees of freedom generates the preasymptotic corrections which, however, have insignificant impact on the lifetimes and various branching fractions of B and B_s mesons. Inclusive N_b decays can be treated with the help of an operator product expansion (OPE) combined with the heavy quark expansion [1]. The OPE approach predicts that all corrections to the leading QCD-improved parton terms are of the order $1/m_b^2$ and higher. Thus, mesons and baryons containing the b quark are expected to have lifetimes differing by no more than a few percent. The result of this approach for the Λ_b lifetime is puzzling, because it predicts that $((\tau(\Lambda_b)/\tau(B))_{OPE} = 0.98 + \mathcal{O}(1/m_b^3)$ [2], whereas the experimental findings suggest a much smaller fraction $((\tau(\Lambda_b)/\tau(B))_{\exp} = 0.78 \pm 0.04$ [3] or, conversely, a much higher decay rate. The decay rates of B and Λ_b are $\Gamma(B) = 0.63 \pm 0.02$ ps^{-1} and $\Gamma(\Lambda_b) = 0.83 \pm 0.05$ ps^{-1} differing by $\Delta\Gamma(\Lambda_b) = 0.20 \pm 0.05$ ps^{-1}. The four-fermion processes of weak scattering and Pauli interference could explain, under certain conditions, only $(13 \pm 7)\%$ of this difference [4] (see, however, [2, 5]). In spite of great efforts of experimental activity, the Λ_b lifetime remains significantly low, which continues to spur theoretical activity. In this respect, the use of phenomenological models, like the constituent quark model, could be of interest as a complementary approach to the OPE resummation method.

In this paper, we shall compute the preasymptotic effects for the Λ_b lifetime in the framework of the light front (LF) quark model, which is a relativistic constituent quark model based on the LF formalism. In [6], this formalism was used to establish a simple quantum mechanical relation between the inclusive semileptonic decay rate of the B meson and that of a free b quark. The approach of [6] relies on the idea of duality in summing over the final hadronic states. It was assumed that the sum over all possible charm final states X_c can be modeled by the decay width of an on-shell b quark into an on-shell c quark folded with the b quark distribution function $f_B^b(x, p_\perp^2) = \left|\varphi_B^2(x, p_\perp^2)\right|^2$. The latter represents the probability of finding a b quark carrying an LF fraction x of the hadron momentum and a transverse relative momentum squared $p_\perp^2$. For the semileptonic rates, the above-mentioned relation takes the form

$$\frac{d\Gamma_{SL}(B)}{dt} = \frac{d\Gamma_{SL}^b}{dt} R_B(t), \tag{1}$$

where $d\Gamma_{SL}^b/dt$ is the free quark differential decay rate; $t = q^2/m_b^2$, q being the 4-momentum of the W boson; and $R_B(t)$ incorporates the nonperturbative effects related to the Fermi motion of the heavy quark inside the hadron. The expression for $d\Gamma_{SL}^b/dt$ for the case of nonvanishing lepton masses is given, e.g., in [6]. $R(t)$ in Eq. (1) is obtained by integrating the bound-state factor $\omega(t, s)$ over the allowed region of the invariant hadronic mass M_{X_c}:

$$R_B(t) = \int_{s_{\min}}^{s_{\max}} ds\,\omega(t, s), \tag{2}$$

[1] This article was submitted by the authors in English.

where $s = M_{X_c}^2/m_b^2$ and

$$\omega(t, s) = m_b^2 x_0 \frac{\pi m_b}{q^+}\frac{|\mathbf{q}|}{|\tilde{\mathbf{q}}|}\int_{x_1}^{\min[1, x_2]} dx\left|\varphi_B^b(x, p_\perp^{*2})\right|^2. \quad (3)$$

In Eq. (3), $x_0 = m_b/M_B$, $p_\perp^{*2} = m_b^2(\xi(1-\rho-t)-\xi^2 t-1)$ with $\xi = xM_B/q^+$, $\rho = (m_c/m_b)^2$, and the limits of integration $x_{1,2}$ are given by $x_{1,2} = x_0 q^+/\tilde{q}^\pm$. The plus component $q^+ = q_0 + |\mathbf{q}|$ is defined in the B-meson rest frame, whereas $\tilde{q}^\pm = \tilde{q}_0 \pm |\tilde{\mathbf{q}}|$ are defined in the b-quark rest frame. In Eq. (2), the region of integration over s is defined through the condition $x_1 \le \min[1, x_2]$; i.e., $s_{\min} = \rho$, $s_{\max} = x_0^{-2}(1 - x_0\sqrt{t})^2$. For other details, see [6].

In the quark model, the Fermi motion effect is due to the interaction with a valence quark. The LF wave function $\varphi_B^b(x, p_\perp^2)$ is defined in terms of the equal-time radial wave function $\psi_B(p^2)$ as [7]

$$\varphi_B^b(x, p_\perp^2) = \frac{\partial p_z}{\partial x}\frac{\psi_B(p^2)}{\sqrt{4\pi}},$$

where $p^2 = p_\perp^2 + p_z^2$,

$$p_z = \left(x - \frac{1}{2}\right)M_0 + \frac{m_{sp}^2 - m_b^2}{2M_0},$$

$$M_0 = \sqrt{p^2 + m_b^2} + \sqrt{p^2 + m_{sp}^2},$$

and m_{sp} is the constituent mass of the spectator quark. An explicit expression for $\partial p_z/\partial x$ can be found in [8]. In what follows, the B-meson orbital wave function is assumed to be the Gaussian function

$$\psi_B(p^2) = (1/\beta_{b\bar{d}}\sqrt{\pi})^{3/2}\exp(-p^2/2\beta_{b\bar{d}}^2), \quad (4)$$

where the parameter $1/\beta_{b\bar{d}}$ defines the confinement scale. We take $\beta_{b\bar{d}} = 0.45$ GeV, which is very close to the variational parameter 0.43 GeV found in the Isgur–Scora model [9] and corresponds to the value of the QCD parameter $-\lambda_1 = \langle p_b^2\rangle = 0.2$ GeV^2. For $|\Psi_B(0)|^2$, the square of the wave function at the origin, we have $|\Psi_B(0)|^2 = 1.64 \times 10^{-2}$ GeV^3. This value compares favorably with the estimation in the constituent quark ansätz [10] $|\Psi_B(0)|^2 = M_B f_B^2/12 = (1.6 \pm 0.7) \times 10^{-2}$ GeV^3 for $f_B = 190 \pm 40$ MeV.

The same formulas can be also applied to nonleptonic B-decay widths (corresponding to the underlying quark decays $b \longrightarrow cq_1q_2$), thus making it possible to calculate the B lifetime [11]. The lepton pair is replaced by a quark pair, so that $d\Gamma_{SL}^b/dq^2$ is replaced by $d\Gamma_{SL}^b/dq^2 = \eta|V_{q_1q_2}|^2 d\Gamma_{SL}^b/dq^2$, where (in the limit $N_c \longrightarrow \infty$) $\eta = \frac{3}{2}(c_+^2 + c_-^2)$, with c_- and $c_+ = c_-^{-1/2}$ being the standard short-distance QCD enhancement and suppression factors in a color antitriplet and sextet, respectively. We take $c_+ = 0.84$, $c_- = 1.42$.

Table 1. The branching fractions (percent) for the inclusive semileptonic and nonleptonic B decays calculated within the LF quark model for several values of the constituent quark mass m_{sp}^*

	m_{sp} = 100 MeV	m_{sp} = 200 MeV	m_{sp} = 300 MeV
$b \longrightarrow ce\nu_e$	10.65	10.98	11.46
$b \longrightarrow c\mu\nu_\mu$	10.59	10.93	11.40
$b \longrightarrow c\tau\nu_\tau$	2.47	2.51	2.57
$b \longrightarrow cd\bar{u}$	47.88	47.88	47.52
$b \longrightarrow c\bar{c}s$	14.07	14.31	14.63
$b \longrightarrow cs\bar{u}$	2.94	3.09	3.32
$B \longrightarrow \Xi_{cs}\bar{\Lambda}_c$	2.22	1.83	1.43
$B \longrightarrow \Lambda_c\bar{N}$	7.70	6.91	6.02
$b \longrightarrow u$	1.47	1.54	1.66
$\lvert V_{bc}\rvert$	38.3	39.3	40.7

* The heavy quark masses are $m_b = 5.1$ GeV, $m_c = 1.5$ GeV. The oscillator parameter in Eq. (4) is $\beta_{b\bar{d}} = 0.45$ GeV. The values of $|V_{cb}|$ in units of $10^{-3}\sqrt{1.56\ \text{ps}/\tau^{(\text{exp})}(B)}$ are also reported.

The constituent quark masses are the free parameters in our model. We have found that the τ_{Λ_b}/τ_B ratio is rather stable with respect to the precise values of the heavy quark masses m_b and m_c, provided $m_b - m_c \gtrsim 3.5$ GeV. From now on, we shall use the reference values $m_b = 5.1$ GeV and $m_c = 1.5$ GeV. The value of the CKM parameter $|V_{cb}|$ cancels in the ratio τ_{Λ_b}/τ_B, but is important for the absolute rates. Details of our calculations of $\Gamma(B)$ are given in Table 1 for the three different values of the constituent mass m_{sp}. The values $m_{sp} \sim 300$ (200) MeV are usually used in nonrelativistic (relativized) quark models [9, 12]. We have also considered a very low constituent quark mass $m_{sp} = 100$ MeV to see how much we can push up the theoretical prediction of the $\Gamma(\Lambda_b)/\Gamma(B)$ (see below). All semileptonic widths include the pQCD correction as an overall reduction factor equal to 0.9. Following [8], we included the transitions to baryon–antibaryon ($\Lambda_c\bar{N}$ and $\Xi_{cs}\bar{\Lambda}$) pairs. In addition, we added $BR \approx 1.5\%$ for the Cabbibo-suppressed $b \longrightarrow u$ decays with

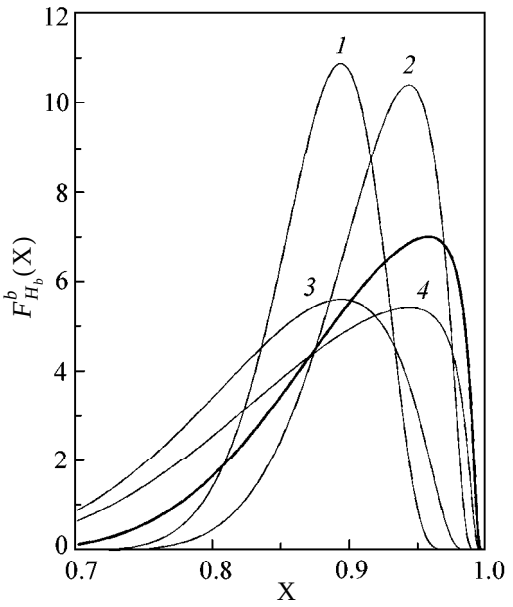

Fig. 1. The distribution functions $F^b_B(x)$ (solid line) and $F^b_{\Lambda_b}(x)$ (thin lines) defined by Eq. (7) versus the LF momentum fraction x. Labels *1* to *4* on the curves refer to the cases $\beta_{bu} = 0.3$ GeV, $m_{ud} = 600$ MeV; $\beta_{bu} = 0.3$ GeV, $m_{ud} = 300$ MeV; $\beta_{bu} = 0.3$ GeV, $m_{ud} = 600$ MeV; and $\beta_{bu} = 0.6$ GeV, $m_{ud} = 300$ MeV, respectively.

$|V_{ub}/V_{cb}| \sim 0.1$. The value of $|V_{cb}|$ is defined by the condition that the calculated B lifetime is 1.56 ps.

Now we turn to the calculation of the Λ_b decay rate. We shall analyze the inclusive semileptonic and nonleptonic Λ_b rates on the simplifying assumption that Λ_b is composed of a heavy quark and a light scalar diquark with the effective mass m_{ud}. Then the treatment of the inclusive Λ_b decays is simplified to a great extent, and we can apply the model considered above with minor modifications. For the heavy–light diquark wave function ψ_{Λ_b}, we again assume the Gaussian ansätz with the oscillator parameter β_{bu}. The width of Λ_b can be obtained from that of B by the replacements $M_B \longrightarrow M_{\Lambda_b}$, $m_{sp} \longrightarrow m_{ud}$, and $\beta_{b\bar{d}} \longrightarrow \beta_{bu}$. Note that the latter two replacements change $f^b_{\Lambda_b}$, the b quark distribution function inside the Λ_b, in comparison with f^b_B.

The inclusive nonleptonic channels for Λ_b are the same as for the B meson, except for the decays into baryon–antibaryon pairs, which are missing in the case of Λ_b. The absence of this decay channel leads to the reduction of $\Gamma(\Lambda_b)$ by ≈7%. This reduction cannot be compensated by the phase-space enhancement in Λ_b. The only way to get an enchancement of Γ_{Λ_b} is to enhance its nonleptonic rates. Altarelly *et al.* [13] have suggested that the increase in the nonleptonic rates could be due to the phenomenological factor $(M_{H_b}/m_b)^5$; then the 6% difference between M_{Λ_b} and M_B is enough to explain the experimentally observed enhancement. In our approach, the only distinction between two lifetimes τ_{Λ_b} and τ_B can occur due to the difference in Fermi motion effects encoded in $f^b_{\Lambda_b}$ and f^b_B.

The f_{Λ_b} is defined by the two parameters m_{ud} and β_{ub}. The latter quantity can be translated into the ratio of the squares of the wave functions determining the probability of finding a light quark at the location of the b quark inside the Λ_b baryon and B meson; i.e.,

$$r = |\Psi_{\Lambda_b}(0)|^2/|\Psi_B(0)|^2 = (\beta_{bu}/\beta_{b\bar{d}})^3. \qquad (5)$$

Estimates of the parameter r using the nonrelativistic quark model, the bag model [14–16], or QCD sum rules [17] are typically in the range 0.1–0.5. On the other hand, Rosner has estimated the heavy–light diquark density at zero separation in Λ_b from the ratio of hyperfine splittings between Σ_b and Σ_b^* baryons and B and B* mesons and finds [4]

$$r = (4/3)(m^2_{\Sigma_b^*} - m^2_{\Sigma_b^*}/m^2_{B^*} - m^2_B). \qquad (6)$$

This leads to $r \sim 0.9 \pm 0.1$, if the baryon splitting is taken to be $m^2_{\Sigma_b^*} - m^2_{\Sigma_b} \sim m^2_{\Sigma_c^*} - m^2_{\Sigma_c} = (0.384 \pm 0.035)$ GeV^2, or even to $r \sim 1.8 \pm 0.5$, if the surprisingly large and not yet confirmed DELPHI result $m_{\Sigma_b^*} - m_{\Sigma_b} = (56 \pm 16)$ MeV [18] is used.

On the other hand, the width $\Gamma(\Lambda_b)$ and, hence, the ratio $\tau(\Lambda_b)/\tau(B)$, is very sensitive to the choice of m_{ud} and r. In order to study the dependence on m_{ud} and r, we keep the values of the quark masses m_b and m_c fixed and vary the wave function ratio in the range $0.3 \le r \le 2.3$, which corresponds to $0.3\ \text{GeV} \le \beta_{bu} \le 0.6$ GeV. We take two representative values for the diquark mass: $m_{ud} = m_u + m_d$ corresponding to the zero binding approximation and $m_{ud} = m_* \approx \frac{1}{2}(m_u + m_d - m_\pi)$. In the latter relation inspired by the quark model, the factor 1/2 arises from the different color factors for u and $\bar{d}$ in the π meson (a triplet and antitriplet making a singlet) and u and d in the Λ_b (two triplets making an antitriplet).

In Fig. 1, we compare the one-dimensional distribution functions

$$F^b_{\Lambda_b}(x) = \pi\int_0^\infty dp_\perp^2 f^b_{\Lambda_b}(x, p_\perp^2) \qquad (7)$$

Table 2. The LF quark model results for the ratio τ_{Λ_b}/τ_B calculated for different sets of parameters. The diquark masses are given in units of MeV, and β_{bu} are in units of GeV

	m_{sp} = 100 MeV		m_{sp} = 200 MeV		m_{sp} = 300 MeV	
β_{bu}/m_{ud}	200	150	400	250	600	400
0.3	0.807	0.795	0.843	0.792	0.885	0.803
0.45	0.877	0.867	0.901	0.857	0.932	0.859
0.6	0.937	0.929	0.951	0.913	0.970	0.906

with that of the B meson. These functions exhibit a pronounced maximum at $m_b/(m_b + m_{sp})$ (in the case of the B meson) and $m_b/(m_b + m_{ud})$ (in the case of Λ_b). The width of F_{Λ_b} depends on β_{bu} and goes to zero when $\beta_{bu} \longrightarrow 0$. Note that the calculated branching fractions of Λ_b show marginal dependence on the choice of the model parameters: they are ~11.5% for the semileptonic $b \longrightarrow ce\nu_e$ transitions, ~2.8% for $b \longrightarrow c\tau\nu_\tau$, ~50% for the nonleptonic $b \longrightarrow cd\bar{u}$ transitions, and ~16% for the $b \longrightarrow c\bar{c}s$ transitions.

Our results for τ_{Λ_b}/τ_B are shown in Table 2 and Fig. 2. We also included the contribution of four-quark operators calculated using the factorization approach and the description of the baryon relying on the quantum mechanics of only the constituent quarks. This contribution leads to a small increase in the Λ_b decay rate by

$$\Delta\Gamma^{4q}(\Lambda_b) = \frac{G_F^2}{2\pi}|\Psi_{bu}(0)|^2|V_{ud}|^2|V_{cb}|^2 m_b^2(1-\rho)^2 \times [c_-^2 - (1+\rho)c_+(c_- - c_+/2)]. \quad (8)$$

This contribution scales like β_{bu}^3 and varies between 0.01 ps^{-1} and 0.03 ps^{-1} when β_{bu} varies between 0.35 and 0.55 GeV.

The quantity τ_{Λ_b}/τ_B is particularly sensitive to the light quark mass m_{sp}. We observe that to decrease the theoretical prediction for τ_{Λ_b}, one needs to decrease the value of the hadronic parameter r in Eq. (5) to 0.3–0.5 and the value of m_{sp} to ~100 MeV. For example, assuming that $r \sim 0.3$, we find that the lifetime ratio decreases from 0.88 to 0.81 if m_{sp} is reduced from 300 to 100 MeV and the diquark mass is chosen as $m_{ud} = m_u + m_d$. For the diquark mass $m_{ud} \sim m_*$, the ratio is almost stable (~0.8), so that reducing the diquark mass produces a decrease in the lifetime ratio by 1, 5, and 8% for m_{sp} = 100, 200, and 300 MeV, respectively. Varying the spectator quark mass in a similar way, we find that for the "central value" $r \sim 1$, the lifetime ratios are reduced from 0.93 to 0.88 for $m_{ud} = m_u + m_d$ and remain almost stable (~0.86) for $m_{ud} \sim m_*$. For the largest possible value of r suggested in [4], $r \sim 2.3$, the lifetime ratios are reduced from 0.97 to 0.94 in the former case and remain almost stable ~0.91–0.93 in the latter case.

If the current value of $(\tau(\Lambda_b)/\tau(B))_{\text{exp}}$ persists, the most likely explanation for this is that some hadronic matrix elements of four-quark operators are larger than the naive expectation (8) [2]. A recent lattice study of [5] suggests that the effects of weak scattering and interference can be pushed at the ~8% level for $r = 1.2 \pm 0.2$, i.e., for an r value significantly larger than the predictions of most quark models but smaller than the upper Rosner estimation. If a significant fraction, ~50%, of the discrepancy between the theoretical prediction for τ_{Λ_b}/τ_B and the experimental result can be accounted for by the spectator effects, then the reminder of the discrepancy

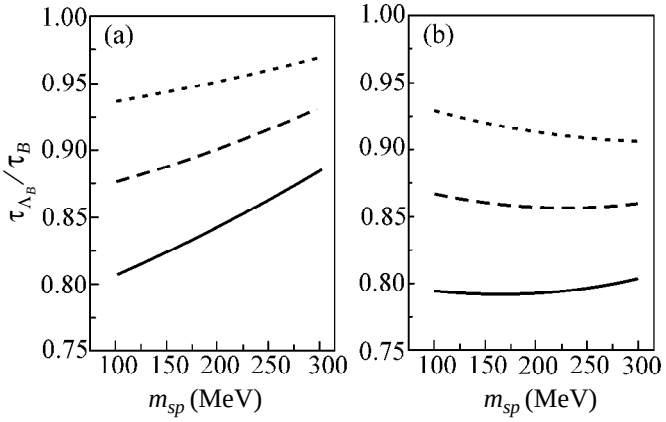

Fig. 2. The lifetime ratios τ_{Λ_b}/τ_B for β = 0.3 GeV (r = 0.3) (solid line), β = 0.45 GeV (r = 1) (long-dashed line), and β = 0.6 GeV (r = 2.37) (short-dashed line). (a) $m_{ud} = m_u + m_d$, and (b) $m_{ud} \sim \frac{1}{2}(m_u + m_d - m_\pi)$.

can be explained by the preasymptotic effect due to Fermi motion of the b quark inside Λ_b. Indeed, choosing the quite reasonable values of the spectator quark mass $m_{sp} = 200$ MeV and the diquark mass $m_{ud} = 250$ MeV and subtracting the small contribution (8), we find that the Fermi motion effect produces an additional reduction of τ_{Λ_b} by $12 \pm 2\%$ for $r = 1.2 \pm 0.2$.

This work was supported in part by the INTAS (grant no. 96-155) and the Russian Foundation for Basic Research (project nos. 00-02-16363 and 00-15-96786).

REFERENCES

1. I. Bigi, M. Shifman, and N. Uraltsev, Annu. Rev. Nucl. Part. Sci. **47**, 591 (1997).
2. M. Neubert and C. T. Sachrajda, Nucl. Phys. B **483**, 339 (1997).
3. T. Junk, Presented at the 2nd International Conference on B-Physics and CP-Violation, Honolulu, 1997; quoted in M. Neubert, hep-ph/9801269.
4. J. L. Rosner, Phys. Lett. B **379**, 267 (1996).
5. M. Di Pierro, C. T. Sachrajda, and C. Michael, hep-lat/9906031.
6. S. Ya. Kotkovsky, I. M. Narodetskiĭ, S. Simula, and K. A. Ter-Martirosyan, Phys. Rev. D **60**, 114024 (1999).
7. F. Coester, Prog. Part. Nucl. Phys. **29**, 1 (1992).
8. I. L. Grach, I. M. Narodetskiĭ, S. Simula, and K. A. Ter-Martirosyan, Nucl. Phys. B **502**, 227 (1997).
9. D. Scora and N. Isgur, Phys. Rev. D **52**, 2783 (1995).
10. E. V. Shuryak, Nucl. Phys. B **198**, 83 (1982).
11. P. Yu. Kulikov and I. M. Narodetskiĭ, Submitted to Yad. Fiz [submitted to Phys. At. Nucl.].
12. S. Godfrey and N. Isgur, Phys. Rev. D **32**, 189 (1985); B. Silvestre-Brac and C. Semay, Nucl. Phys. A **618**, 455 (1997).
13. G. Altarelli, G. Martinelli, S. Petrarca, and F. Rapuano, Phys. Lett. B **382**, 409 (1996).
14. M. B. Voloshin and M. A. Shifman, Yad. Fiz. **41**, 187 (1985) [Sov. J. Nucl. Phys. **41**, 120 (1985)]; Zh. Éksp. Teor. Fiz. **91**, 1180 (1986) [Sov. Phys. JETP **64**, 698 (1986)].
15. B. Guberina, S. Nussinov, R. Peccei, and R. Rückl, Phys. Lett. B **89**, 111 (1979); N. Bilić, B. Guberina, and J. Trampetić, Nucl. Phys. B **248**, 261 (1984); B. Guberina, R. Rückl, and J. Trampetić, Z. Phys. C **33**, 297 (1986).
16. I. Bigi *et al.*, in *B-decays*, 2ed., Ed. by S. Stone (World Scientific, Singapore, 1994), p. 134; I. Bigi, hep-ph/9508408.
17. P. Conangelo and F. De Fazio, Phys. Lett. B **387**, 371 (1996).
18. P. Abreu *et al.*, DELPHI 95-107 PHYS 542.

JETP Letters, Vol. 71, No. 9, 2000, pp. 367–369. Translated from Pis'ma v Zhurnal Éksperimental'noĭ i Teoreticheskoĭ Fiziki, Vol. 71, No. 9, 2000, pp. 534–538.

Charged-Surface Instability Development in Liquid Helium: An Exact Solution

N. M. Zubarev

Institute of Electrophysics, Ural Division, Russian Academy of Sciences, Komsomol'skaya ul. 34, Yekaterinburg, 620219 Russia

e-mail: nick@ami.uran.ru

Received March 20, 2000

The nonlinear dynamics of charged-surface instability development is investigated for liquid helium far above the critical point. It is found that, if the surface charge completely screens the field above the surface, the equations of three-dimensional (3D) potential motion of a fluid are reduced to the well-known equations describing the 3D Laplace growth process. The integrability of these equations in 2D geometry allows the analytic description of the free-surface evolution up to the formation of cuspidal singularities at the surface. © *2000 MAIK "Nauka/Interperiodica".*

PACS numbers: 67.55.Fa; 68.10.-m

It is known [1] that the flat electron-charged surface of liquid helium is unstable if the electric field strengths above (E_+) and inside (E_-) the fluid satisfy the inequality $E_+^2 + E_-^2 > E_c^2 = 8\pi\sqrt{g\alpha\rho}$, where g is the free-fall acceleration, α is the surface tension coefficient, and ρ is the fluid density. An analysis of the critical behavior of the system suggests that, depending on the dimensionless parameter $S = (E_-^2 - E_+^2)/E_c^2$, the nonlinearity leads either to the saturation of linear instability or, conversely, to an explosive increase in amplitude. The first situation may result in the formation of a stationary perturbed surface relief (hexagons [2] and many-electron dimples [3]) in liquid helium. The use of perturbation theory, with the surface slope as a small parameter, allowed a detailed analytic study of such structures in the critical region [4, 5]. In the second case, the small-angle approximation fails. The cinematographic study by Volodin, Khaĭkin, and Édel'man [6] has demonstrated that the development of surface instability culminates in this case in the formation of dimples and their sharpening in a finite time. The substantial nonlinearity of these processes calls for a theoretical model that is free from the requirement for smallness of surface perturbations and adequately describes the formation dynamics of a singular surface profile in liquid helium. This work demonstrates that such a model can be developed if the condition $E_- \gg E_+$ is fulfilled, i.e., if the field above liquid helium is fully screened by the surface electron charge and if the electric field far exceeds its critical value, i.e., $E_- \gg E_c$.

Let us consider the potential motion of an ideal fluid (liquid helium) in a region bounded by the free surface $z = \eta(x, y, t)$. We assume that the characteristic scale λ of surface perturbations is much smaller than the fluid depth. We also assume that $\alpha E_-^{-2} \ll \lambda \ll E_-^2/g\rho$, so that the capillary and gravity effects can be ignored. The electric field potential $\varphi(x, y, z, t)$ in a medium and the fluid velocity potential $\Phi(x, y, z, t)$ satisfy the Laplace equations

$$\nabla^2\varphi = 0, \quad \nabla^2\Phi = 0, \tag{1}$$

which should be solved jointly with the conditions at the surface

$$\varphi = 0, \quad \eta_t = \Phi_z - \nabla_\perp\eta\nabla_\perp\Phi,$$
$$8\pi\rho\Phi_t + 4\pi\rho(\nabla\Phi)^2 + (\nabla\varphi)^2 = E_-^2, \quad z = \eta(x, y, t), \tag{2}$$

and the conditions at infinity

$$\varphi \longrightarrow -zE_-, \quad \Phi \longrightarrow 0, \quad z \longrightarrow -\infty. \tag{3}$$

Let us pass to dimensionless variables, taking λ as a length unit, E_- as a unit of electric field strength, and $\lambda E_-^{-1}(4\pi\rho)^{1/2}$ as a time unit. It is convenient to rewrite the equations of motion of the free surface $z = \eta(x, y, t)$ in implicit form (not explicitly containing the η function). Let introduce the perturbed potential $\tilde{\varphi} = \varphi + z$ decaying at infinity. One has at the boundary $\tilde{\varphi}|_{z=\eta} = \eta$. It is then straightforward to obtain the following relationships:

$$\eta_t = \left.\frac{\tilde{\varphi}_t}{1 - \tilde{\varphi}_z}\right|_{z=\eta}, \quad \nabla_\perp\eta = \left.\frac{\nabla_\perp\tilde{\varphi}}{1 - \tilde{\varphi}_z}\right|_{z=\eta},$$

which allow one to eliminate the η function from Eq. (2). The kinematic and dynamic boundary conditions then

take the form

$$\tilde{\varphi}_t - \Phi_z = -\nabla\tilde{\varphi}\nabla\Phi,$$
$$\Phi_t - \tilde{\varphi}_z = -(\nabla\Phi)^2/2 - (\nabla\tilde{\varphi})^2/2, \quad (4)$$
$$z = \eta(x, y, t).$$

Let now introduce a pair of auxiliary potentials:

$$\phi^{(\pm)}(x, y, z, t) = (\tilde{\varphi} \pm \Phi)/2.$$

With these potentials, the fluid surface shape can be defined by the relationship

$$\eta = (\phi^{(+)} + \varphi^{(-)})\big|_{z=\eta}, \quad (5)$$

while equations of motion (1)–(3) are reduced to the following symmetric form:

$$\nabla^2\phi^{(\pm)} = 0, \quad (6)$$

$$\phi_t^{(\pm)} = \pm\phi_z^{(\pm)} \mp (\nabla\phi^{(\pm)})^2, \quad z = \eta(x, y, t), \quad (7)$$

$$\phi^{(\pm)} \longrightarrow 0, \quad z \longrightarrow -\infty, \quad (8)$$

where boundary conditions (7) are obtained by combining Eqs. (4) with plus and minus signs, respectively.

It is seen that the equations of motion are split into two systems of equations for the potentials $\phi^{(+)}$ and $\phi^{(-)}$, which are implicitly related by the equation for surface shape (5). An essential point is that these equations are compatible with either the $\phi^{(-)} = 0$ or $\phi^{(+)} = 0$ condition. One can readily see that the first condition corresponds to those solutions whose amplitude increases with time, while the second condition corresponds to decaying solutions that are of no interest to us.

Thus, an analysis of the equations of motion of a charged surface of liquid helium reveals a solution increasing with t and corresponding to the $\phi^{(-)} = 0$ condition or, which is the same, to the $\varphi + z = \Phi$ condition (the stability of this branch of solutions is proved below). The functional relation between the potentials can be used to eliminate the velocity potential Φ from initial Eqs. (1)–(3). In the moving system of coordinates $\{x', y', z'\} = \{x, y, z, -t\}$, one has

$$\nabla^2\varphi = 0, \quad (9)$$

$$\eta_t' = \partial_n\varphi\sqrt{1 + (\nabla_\perp\eta')^2}, \quad z' = \eta'(x', y', t), \quad (10)$$

$$\varphi = 0, \quad z' = \eta'(x', y', t), \quad (11)$$

$$\varphi \longrightarrow -z', \quad z' \longrightarrow -\infty, \quad (12)$$

where $\eta'(x', y', t) = \eta - t$ and ∂_n denotes the normal derivative. These equations explicitly describe the motion of a free charged surface $z' = \eta'(x', y', t)$. They coincide with the equations for the so-called Laplace growth process, i.e., phase boundary movement with velocity directly proportional to the normal derivative of a certain scalar field (φ in our case). Depending on the system, this may be the temperature (Stefan problem in the quasi-stationary limit), the electrostatic potential (electrolytic deposition), the pressure (flow through a porous medium), etc.

Note that the boundary movement described by Eqs. (9)–(12) is invariably directed inward from the surface. Let η' be a single-valued function of the variables x' and y' at zero time $t = 0$. Then the inequality $\eta(x', y', t) \le \eta(x', y', 0)$ holds for $t > 0$. In the initial notations,

$$\eta(x, y, t) \le \eta(x, y, 0) + t \quad (13)$$

for any x and y. This condition can be used to prove the stability of the ascending branch to small perturbations of potential $\phi^{(-)}$. Clearly, the boundary motion at small $\phi^{(-)}$ values is entirely controlled by the potential $\phi^{(+)}$ [one should set $\phi^{(-)} = 0$ in Eq. (5)] and hence obeys Eqs. (9)–(12). The evolution of the $\phi^{(-)}$ potential is described by Eqs. (6)–(8), with the following simple boundary condition in the linear approximation:

$$\phi_t^{(-)} = -\phi_z^{(-)}, \quad z = \eta(x, y, t).$$

Let the potential distribution at zero time $t = 0$ be determined by the expression $\phi^{(-)}\big|_{t=0} = \phi_0(x, y, z)$, where ϕ_0 is a harmonic function at $z \le \eta(x, y, 0)$ decaying as $z \longrightarrow -\infty$. It is then straightforward to show that the time dynamics of the $\phi^{(-)}$ potential is given by $\phi^{(-)} = \phi_0(x, y, z - t)$. This implies that the singularities of the $\phi^{(-)}$ function will drift in the z direction, so that they will occur only in the $z > \eta(x, y, 0) + t$ region. Taking into account inequality (13), one finds that the singularities always move away from the boundary $z = \eta(x, y, t)$ of liquid helium. Consequently, the perturbation $\phi^{(-)}$ will relax to zero, as we wished to prove.

Let now turn to the analysis of the dynamics of surface instability development in liquid helium. In the 2D case (all quantities are taken to be independent of the y variable), system of Eqs. (9)–(12) is reduced to the well-known Laplace growth equation (see, e.g., [7] and references therein)

$$\mathrm{Im}(f_t^* f_w) = 1.$$

In this expression, $f = x' + iz'$ is a complex function analytical in the lower half-plane of the complex variable $w = \psi - i\varphi$ and satisfying condition $f \longrightarrow w$ at $w \longrightarrow \psi - i\infty$. Note that the ψ function is a harmonic conjugate to φ, while the condition $\psi = \text{const}$ defines the electric field lines in a medium. The Laplace growth

equation is integrable in the sense that it allows for an infinite number of partial solutions

$$f(w) = w - it - i\sum_{n=1}^{N} a_n \ln(w - w_n(t)) + i\left(\sum_{n=1}^{N} a_n\right)\ln(w - \tilde{w}(t)),$$

where a_n are complex constants and $\mathrm{Im}(w_n) > 0$. The last term is added in order that the condition $\eta \longrightarrow 0$ be fulfilled at $|x| \longrightarrow \infty$. One can put $\mathrm{Im}\,\tilde{w} \gg \mathrm{Im}(w_n)$; in this case, the influence of this term on the surface evolution can be ignored. The functions $w_n(t)$ are defined by the following set of transcendental equations:

$$w_n + it + i\sum_{m=1}^{N} a_m^* \ln(w_n - w_m^*) = C_n,$$

where C_n are arbitrary complex constants.

Let us consider the simplest ($N = 1$) solution to the Laplace growth equation:

$$\begin{aligned} f(w) &= w - it + i\ln(w - ir(t)), \\ r(t) - \ln r(t) &= 1 + t_c - t, \end{aligned} \tag{14}$$

where t_c is a real constant and the real function $r(t) \geq 1$. The shape of a solitary perturbation corresponding to Eq. (14) is given parametrically by the expressions

$$\begin{aligned} z(\psi, t) &= \ln\sqrt{\psi^2 + r^2(t)}, \\ x(\psi, t) &= \psi - \arctan(\psi/r(t)). \end{aligned} \tag{15}$$

This solution holds only for a finite time period and culminates in the formation, at time $t = t_c$, of a singularity in the form of a first-kind cusp at the fluid surface. Indeed, setting $r = r(t_c) = 1$ in Eq. (15), one obtains $2z = |3x|^{2/3}$ in the leading order near the singular point (see also [8]). Note that the electric field strength goes to infinity at the cusp: $\partial_n\varphi \sim x_\psi^{-1}\big|_{\psi=0} \sim 1/\sqrt{t_c - t}$. The surface velocity also becomes infinite in a finite time: $\eta t = \eta_t = z_t\big|_{\psi=0} \sim 1/\sqrt{t_c - t}$. It is worth noting that the singular solution in the leading order is also true when the field above the surface is incompletely screened. The point is that the requirement that the field above the surface be small compared to the field in the fluid is naturally satisfied in the vicinity of the singularity.

Let us now discuss the influence of the capillary effects. One can readily estimate the surface and electrostatic pressures near the surface:

$$\alpha R^{-1} \sim \alpha\rho^{1/2} E_-^{-1}(t_c - t)^{-1},$$
$$(\partial_n\varphi)^2 \sim \lambda\rho^{1/2} E_-(t_c - t)^{-1}.$$

Insofar as we assumed that $\lambda \gg \alpha E_-^{-2}$, the capillary forces cannot compete with the electrostatic ones, so that there is no need to take into account the surface forces at the stage of cusp formation.

In summary, we succeeded in finding a broad class of exact solutions to the equations of motion of a charged surface of liquid helium. It is remarkable that the solutions obtained are not constrained by the condition for the smallness of surface perturbations: the model suggested describes free-surface instability development up to the formation of singularities (cusps) similar to those observed in experiment [6].

I am grateful to E.A. Kuznetsov for stimulating discussions. This work was supported by the Russian Foundation for Basic Research (project no. 00-02-17428) and the INTAS (grant no. 99-1068).

REFERENCES

1. L. P. Gor'kov and D. M. Chernikova, Dokl. Akad. Nauk SSSR **228**, 829 (1976) [Sov. Phys. Dokl. **21**, 328 (1976)].
2. M. Wanner and P. Leiderer, Phys. Rev. Lett. **42**, 315 (1979).
3. A. A. Levchenko, E. Teske, G. V. Kolmakov, *et al.*, Pis'ma Zh. Éksp. Teor. Fiz. **65**, 547 (1997) [JETP Lett. **65**, 572 (1997)].
4. V. B. Shikin and P. Leĭderer, Pis'ma Zh. Éksp. Teor. Fiz. **32**, 439 (1980) [JETP Lett. **32**, 416 (1980)].
5. V. I. Mel'nikov and S. V. Meshkov, Zh. Éksp. Teor. Fiz. **81**, 951 (1981) [Sov. Phys. JETP **54**, 505 (1981)]; Zh. Éksp. Teor. Fiz. **82**, 1910 (1982) [Sov. Phys. JETP **55**, 1099 (1982)].
6. V. P. Volodin, M. S. Khaĭkin, and V. S. Édel'man, Pis'ma Zh. Éksp. Teor. Fiz. **26**, 707 (1977) [JETP Lett. **26**, 543 (1977)].
7. M. B. Mineev-Weinstein and S. P. Dawson, Phys. Rev. E **50**, R24 (1994).
8. S. D. Howison, SIAM J. Appl. Math. **46**, 20 (1986).

Translated by V. Sakun

JETP Letters, Vol. 71, No. 9, 2000, pp. 370–372. Translated from Pis'ma v Zhurnal Éksperimental'noĭ i Teoreticheskoĭ Fiziki, Vol. 71, No. 9, 2000, pp. 539–543.

ATOMS, SPECTRA, RADIATIONS

Femtosecond Optical Pulse Compression in a One-Dimensional Thin Photonic Crystal

A. V. Andreev*, A. V. Balakin*, D. Boucher, P. Masselin**, I. A. Ozheredov*, and A. P. Shkurinov***

** Faculty of Physics, Moscow State University, Vorob'evy gory, Moscow, 119899 Russia*
e-mail: ilya@lasmed.ilc.msu.su
*** Laboratoire de Physicochimie de l'Atmosphère, Université du Littoral, 59140 Dunkerque, France*
Received March 20, 2000

The effect of femtosecond laser pulse compression is discovered, described, and experimentally studied for a one-dimensional 4.8-μm-thick photonic crystal. © *2000 MAIK "Nauka/Interperiodica".*

PACS numbers: 42.65.Re; 42.70.Qs; 42.70.Mp

1. In recent years, considerable interest has been expressed in the optical phenomena in photonic crystals [1]. A multilayer periodic structure (MPS) with modulated refractive index and/or nonlinear susceptibility is a particular case of a one-dimensional photonic crystal. Due to the periodic modulation, optical radiation in photonic crystals suffers total Bragg reflection in certain ranges of wavelengths and wave vectors [2], giving rise to the so-called "photonic band gaps." Many linear and nonlinear optical phenomena in the vicinity of or inside these gaps exhibit anomalous or specific behavior. For instance, it was demonstrated in our recent works [3–5] that specific amplification of nonlinear optical effects, such as second-harmonic and sum-frequency generation, is possible at the edge of Bragg selective reflection in MPSs.

Recently, particular interest has arisen in studying various dynamic effects associated with the propagation of ultrashort laser pulses in photonic crystals. It was demonstrated in [6] that optical pulse compression is possible in periodically modulated optical waveguides. More recently [7], studies were carried out on the effect of picosecond laser pulse compression caused by the simultaneous action of phase self-modulation and frequency dispersion in a Bragg grating induced in an optical fiber with Kerr-type nonlinearity. The studies carried out in [8] for one-dimensional submillimeter photonic crystals have shown that the dispersion properties of multilayer structures allow one to accomplish phase control and compensate the phase modulation (chirp) of femtosecond optical pulses.

2. This letter reports the results of experimental studies of the femtosecond optical pulse compression phenomenon in a one-dimensional photonic crystal fabricated as a thin multilayer structure with a periodically modulated refractive index. In our experiments, laser pulses of femtosecond duration and MPS samples with a deeply modulated refractive index ($\Delta n = 0.8$) were used. To date, experimental studies of the ultrashort pulse compression effects have been performed on the picosecond time scale, so that the question of experimental implementation of femtosecond laser pulse compression in photonic crystals remains open.

The frequency–angular dispersion of MPS was calculated with the use of the nonreduced equations of the dynamical theory of two-wave diffraction [9]. The calculations showed that the model suggested is applicable to describing the dispersion in photonic crystals and provides both qualitative and quantitative agreement with the experimental results.

3. A one-dimensional photonic crystal in the form of MPS (described in detail in [3]) was the object of experimental investigation. The sample was made up of eight ZnS layers ($n_{ZnS} = 2.32$) and seven SrF_2 layers ($n_{SrF_2} = 1.52$), the thickness of each of them being $d_i = 3\lambda/4n_i$ for the wavelength $\lambda = 790$ nm. The total MPS thickness was $L = 4.8$ μm. The Bragg reflection in the MPS occurred in the wavelength range from 745 to 830 nm for normal incidence on the structure.

The experimental setup was described in detail in our previous publications [5, 10]. The experiments were performed with femtosecond laser pulses from the output of a regenerative amplifier RegA 9000 (Coherent Inc.) at a wavelength of $\lambda = 815$ nm with an average power of 3 mW and a pulse repetition rate of 200 kHz. The pulse duration at the output of the regenerative amplifier was $\tau_0 = 270$ fs for FWHM $\Delta\lambda = 8$ nm, which was close to the parameters of spectrally limited pulses ($\tau_0\Delta\nu \approx 1$). The pulse duration and the chirp sign and magnitude were varied using a grating compressor at the output of the regenerative amplifier. The pulse parameters were measured immediately ahead of the

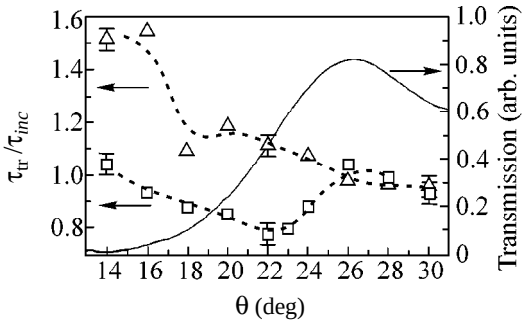

Fig. 1. Relative change in the duration of pulses transmitted through the MPS vs. the angle of incidence for (△) the negatively chirped and (□) the positively chirped pulses. The solid line indicates MPS transmission as a function of the angle of incidence.

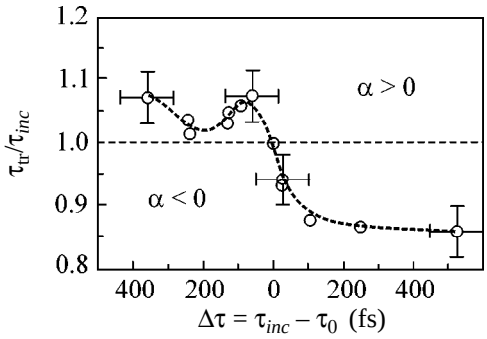

Fig. 2. Relative change in the duration of pulses transmitted through the MPS vs. the difference between the duration of the incident pulse and the τ_0 value. The $\alpha > 0$ and $\alpha < 0$ regions correspond to the different chirp signs of the incident pulse.

sample under study. The duration of femtosecond pulses was determined using the autocorrelation technique based on measuring the second-order autocorrelation function of the intensity.

4. In our experiments, we examined the spectral and temporal characteristics of pulsed radiation incident on the MPS at different angles θ and transmitted through the sample. The experiments consisted of measuring the pulse duration and recording the pulse spectrum. All measurements were made using a linearly polarized laser emission with the polarization perpendicular to the plane of incidence on the sample (*s*-polarization) [3].

To reveal the influence of MPS on the temporal parameters of the femtosecond laser pulses, two series of experiments were carried out.

Figure 1 presents the results of the first experimental series, in which the duration of the pulses transmitted through the MPS was measured as a function of the angle θ of incidence of the optical radiation on the sample. The measurements were carried out for two cases: in the first one, the chirp was negative; and in the second, it was positive. In both cases, the spectral width of the pulses and their duration were identical and equal to 8 nm and 550 fs, respectively.

The experimental dependences for the positive and negative chirps are tangibly different. With the positive chirp, the pulse duration sizably shortens and exhibits a well-defined minimum at $\theta = 22°$ corresponding to the edge of the Bragg selective reflection band. For the negative chirp, the pulse duration monotonically decreases with increasing angle of incidence θ and does not exhibit any distinct tendency to pulse compression.

In the second series of experiments (Fig. 2), the duration of the pulses transmitted through the MPS was examined as a function of the difference between the duration of the incident pulses and τ_0. The measurements were performed at a fixed angle of incidence $\theta = 22°$ on the MPS. In the course of measurements, the duration of the incident pulses was varied at fixed spectral widths for the $\alpha > 0$ (positive chirp) and the $\alpha < 0$ (negative chirp) cases, where α is the parameter characterizing the incident pulse chirp. As the chirp magnitude increases, the positively chirped pulses are effectively compressed to 0.85 of the incident pulse duration, whereas the negatively chirped pulses do not exhibit compression for any of the chirp magnitudes.

5. Let us apply the theory developed in [9] for dynamical diffraction in multilayer structures to describe the observed pulse compression. The electric-field strength in the one-dimensional MPS of interest can be written as

$$E(\mathbf{r}, t) = \sum_{i=1}^{4} \int E_i(\omega) \left\{ \exp\left[i\left(\frac{3}{2}H - \Delta k_i\right)\right] + c_i \exp\left[i\left(-\frac{3}{2}H - \Delta k_i\right)z\right]\right\} \exp[i(\boldsymbol{\kappa}_0\boldsymbol{\rho} - \omega t)]\, d\omega, \quad (1)$$

where $\boldsymbol{\kappa}_0$ is the wavevector of the incident beam, $\boldsymbol{\rho} = \{x, y, 0\}$ is the two-dimensional vector in the plane of the entrance face of the structure, $H = 2\pi/d$ is the reciprocal lattice vector of a structure with period d, and c_i is the amplitude ratio of the diffracted and refracted waves corresponding to the ith root of the dispersion equation.

In the two-wave approximation, the dispersion equation for the structure being considered has the form

$$\Delta k_i(\omega, \theta) = \pm\left[\left(\frac{3}{2}H\right)^2 + \left(\frac{\omega}{c}\right)^2(\gamma_0^2 + \chi_0) \pm \frac{\omega}{c}\sqrt{9H^2(\gamma_0^2 + \chi_0) + \left(\frac{\omega}{c}\right)^2 \chi_{\bar{3}}\chi_3}\right]^{1/2}, \quad (2)$$

where $\gamma_0 = \cos\theta$, θ is the angle of incidence measured from the normal, and χ_h is the Fourier component of the

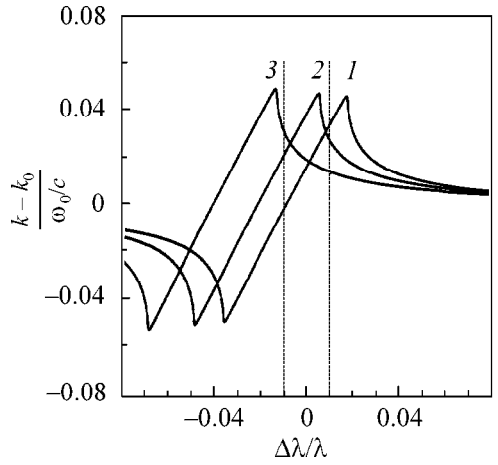

Fig. 3. The difference between the normal projections of the wavevectors in a periodic structure and in a continuous structure with polarizability χ_0 vs. the detuning ($\Delta\lambda / \lambda$) of the incident radiation for several angles of incidence: θ = (*1*) 10°, (*2*) 20°, and (*3*) 30°. The vertical dotted lines indicate the radiation spectral width used in the experiments.

structure polarizability

$$\chi_h = \frac{4\pi}{d}\int_0^d \chi(z)\exp[-iH_h z]dz.$$

The amplitudes E_i in Eq. (1) are determined from the boundary conditions. The E_i values corresponding to the solutions with a minus sign in the radicand in Eq. (2) are the largest. Hence, only the first term may be held in Eq. (1) for estimates. Let us expand Δk_1 in powers of the detuning from the carrier frequency ω_0:

$$\Delta k(\omega) = \Delta k(\omega_0) + \frac{\partial \Delta k}{\partial \omega}(\omega - \omega_0) + \frac{1}{2}\frac{\partial^2 \Delta k}{\partial \omega^2}(\omega - \omega_0)^2. \quad (3)$$

It is seen from Eqs. (2) and (3) that the largest dispersion occurs at the reflection curve edge, where $\Delta k_1 \approx 0$ and, hence, the terms with higher-order derivatives in Eq. (3) increase. The results of numerical calculations of the difference between the normal projections of wavevectors in the MPS with the above-listed parameters and in a continuous structure with polarizability $\chi_0 = (\chi_1 d_1 + \chi_2 d_2)/(d_1 + d_2)$ are presented in Fig. 3 as functions of the detuning ($\Delta\lambda / \lambda$) of incident radiation for several angles of incidence θ. Figure 3 clearly demonstrates that the largest compression is achieved at the incidence angle of $\theta = 22°$, while the compression magnitude depends on the angular width of the incident beam.

Assuming that the incident pulse profile is

$$E(t) = E_0\exp\left[i\omega_0 t - \frac{1}{2}(i\alpha + \tau_{inc}^{-2})t^2\right]$$

and using expansion (3), one obtains for the pulse duration at the output $z = L$

$$\tau_p(L) = \tau_{inc}\sqrt{(1 + \alpha\mu)^2 + \mu^2/\tau_{inc}^4}, \quad (4)$$

where $\mu = \partial^2\Delta k/\partial\omega^2$. Taking into account that $\mu < 0$, it is straightforward to see from Eq. (4) that the positively chirped ($\alpha > 0$) pulse shortens, while for the negative chirp ($\alpha < 0$) the pulse duration increases. Substituting the above-mentioned MPS parameters into Eqs. (2) and (3), one arrives at $\tau_p(L)$ = 300–400 fs, in fairly good agreement with the experimental results.

In summary, this letter reports studies of femtosecond laser pulse compression in a one-dimensional photonic crystal. A good agreement obtained between the theoretical and experimental results allows the conclusion to be drawn that femtosecond laser pulse compression in a one-dimensional photonic crystal prepared as an MPS with strongly modulated linear refractive index is possible for a crystal length as small as 4.8 μm.

This work was supported in part by the Russian Foundation for Basic Research, project nos. 99-02-16093 and 98-02-17544. The Laboratoire de Physicochimie de l'Atmosphère is a member of the Centre d'Etude et de Recherche Lasers et Applications, which is supported by the Ministère de la Recherche, the Région Nord/Pas de Calais, and the Fond Européen de Dévelopment Economique des Régions.

REFERENCES

1. E. Yablonovitch, J. Mod. Opt. **41**, 173 (1994).
2. A. Yariv and P. Yeh, *Optical Waves in Crystals, Propagation and Control of Laser Radiation* (Wiley, New York, 1984; Mir, Moscow, 1987).
3. A. V. Balakin, D. Boucher, V. A. Bushuev, *et al.*, Opt. Lett. **24**, 793 (1999).
4. A. V. Andreev, O. A. Andreeva, A. V. Balakin, *et al.*, Kvantovaya Élektron. (Moscow) **28**, 75 (1999) [Quantum Electron. **29**, 632 (1999)].
5. A. V. Balakin, D. Boucher, V. A. Bushuev, *et al.*, Pis'ma Zh. Éksp. Teor. Fiz. **70**, 718 (1999) [JETP Lett. **70**, 725 (1999)].
6. B. J. Eggleton, R. E. Slusher, C. Martijn de Sterke, *et al.*, Phys. Rev. Lett. **76**, 1627 (1996).
7. B. J. Eggleton, G. Lenz, R. E. Slusher, and N. M. Litchinitser, Appl. Opt. **37**, 7055 (1998).
8. A. M. Zheltikov, N. I. Koroteev, S. A. Magnitskiĭ, and A. V. Tarasishin, Kvantovaya Élektron. (Moscow) **25**, 885 (1998).
9. A. V. Andreev, Yu. V. Ponomarev, Yu. Ya. Platonov, and N. N. Salashchenko, Proc. SPIE **2801**, 75 (1996).
10. A. V. Balakin, D. Boucher, N. I. Koroteev, *et al.*, Zh. Éksp. Teor. Fiz. **112**, 97 (1997) [JETP **85**, 52 (1997)].

Translated by V. Sakun

JETP Letters, Vol. 71, No. 9, 2000, pp. 373–376. Translated from Pis'ma v Zhurnal Éksperimental'noĭ i Teoreticheskoĭ Fiziki, Vol. 71, No. 9, 2000, pp. 544–549.

CONDENSED MATTER

Phase Diagram of a Thin Ferromagnetic Film on the Surface of an Antiferromagnet

V. D. Levchenko*, A. I. Morosov, and A. S. Sigov****

** Keldysh Institute of Applied Mathematics, Russian Academy of Sciences, Miusskaya pl. 4, Moscow, 125047 Russia*

*** Moscow State Institute of Radio Engineering, Electronics, and Automation (Technical University), pr. Vernadskogo 78, Moscow, 117454 Russia*

e-mail: morosov@eot-gw.eot.mirea.ac.ru

Received February 8, 2000

Magnetic characteristics of a thin ferromagnetic film on the surface of an antiferromagnet are examined. Due to the roughness of the film–substrate interface, the system is frustrated, giving rise to domain walls of new type. The distributions of the order parameters in the domain walls are studied by mathematical modeling, and the phase diagram is obtained. © *2000 MAIK "Nauka/Interperiodica".*

PACS numbers: 75.70.-i; 75.30.Kz

In the decade since the discovery of the giant magnetoresistance phenomenon [1], a great many publications have been devoted to multilayer magnetic structures. In recent years, the attention of researchers has been focused on multilayer ferromagnet–layered antiferromagnet structures. Atomic steps at the interfaces change the antiferromagnet thickness by one monatomic layer, giving rise to frustrations in the ferromagnet–antiferromagnet system. As a result, the homogeneous distribution of order parameters in the layers no longer corresponds to the energy minimum.

If the separation between the atomic steps (terrace length R) at the layer surface exceeds a certain critical value, the formation of magnetic domains inside the ferromagnetic layers becomes energetically favorable [2, 3]. The domain walls in the layer planes coincide with the step edges.

Recent studies of the state of a ferromagnetic iron film on a rough Cr (001) surface suggested the presence of several magnetic phases, depending on the film thickness and the degree of roughness (R value) [4].

It follows from the foregoing that the determination of the "thickness–roughness" phase diagram for the simplest magnetic structure, ferromagnet–layered antiferromagnet, is a topical problem. The present work is devoted to this issue.

1. Description of the model. In describing the multilayer structure, we restrict ourselves to the mean-field approximation. Let us introduce the order parameter for each layer. These are the magnetization vector for the ferromagnetic layers and the antiferromagnetic vector, i.e., the difference in the sublattice magnetizations, for the antiferromagnetic layers.

It is known that the atomic spins in a thin magnetic layer (of thickness no greater than tens of angstroms) are aligned in the layer planes. For this reason, at $T < (T_C, T_N)$, where T_C is the Curie temperature of the ferromagnetic layers and T_N is the Néel temperature of the antiferromagnetic layers, the local order parameter is aligned in the layer plane and can thus be characterized by the angle θ it forms with a certain preferred axis also lying in the layer plane. The absolute value of the order parameter is assumed to be virtually constant in each layer.

With the approximations adopted, the exchange energy W_i due to the inhomogeneity in the ith layer is written as

$$W_i = \frac{J_i S_i^2}{2b_i}\int(\nabla\theta_i)^2 dV, \qquad (1)$$

where the integral is taken over the layer volume, J_i is the exchange hardness, S_i is the mean atomic spin, and b_i is the interatomic distance. Variation of Eq. (1) with respect to θ_i yields the following equation for the distribution of the order parameter in the layer:

$$\Delta\theta_i = 0. \qquad (2)$$

To formulate the boundary conditions, the interaction energy for the spins located near the interface should be represented in discrete form and differentiated with respect to the rotation angle of a particular spin, whereupon turning back to the continuous representation gives

$$\Delta\theta_i - \frac{\partial\theta_i}{\partial n} = \pm\frac{J_{f,af}S_{i+1}}{J_i S_i}\sin(\theta_i - \theta_{i+1}), \qquad (3)$$

where Δ is the two-dimensional Laplacian in the plane of the layer, $\partial/\partial n$ is the directional derivative along the outer normal to the layer, and the exchange constant

$J_{f,af}$ stands for the interaction between the spins belonging to different layers; all distances are dimensionless and given in units of $b_i = b$ taken to be the same for all layers. On the different sides of atomic step at the interface, the signs of the right-hand side of Eq. (3) are opposite. For a free surface, the expression on the right-hand side of Eq. (3) is zero.

The variation with respect to θ_i of the interfacial interaction energy written in the continuous representation yields an equation differing from Eq. (3) by the absence of the first term on the left-hand side. This makes the transition from Eq. (3) to Eq. (2) impossible if the interfacing layers are identical.

The energy of exchange interaction between the neighboring layers is

$$W_{i,i+1} = \pm\frac{J_{f,af}S_iS_{i+1}}{b^2}\int\cos(\theta_i - \theta_{i+1})dS, \qquad (4)$$

where the integral is taken over the interface, while the sign of the right-hand side of Eq. (4) corresponds to that in Eq. (3). The atomic steps divide the interface into regions of two types. In regions of the first type, the boundary energy is minimum at $\theta_i = \theta_{i+1}$, while in regions of the second type, at $\theta_i = \pi - \theta_{i+1}$.

The solution to the system of differential equations (2) with boundary conditions (3) gives the distribution of the order parameters in a multilayer structure. The continuous representation applies if the characteristic distances of the problem are large on the interatomic distance scale. The layer thicknesses in the multilayer structures and the distances between the atomic steps are typically equal to several tens of angstroms. One can thus consider these distances as being much larger than the interatomic distances and use the continuous representation for the qualitative analysis and estimates of the orders of magnitude.

In the model considered, the exchange interaction is assumed to be isotropic, i.e., the same in the layer planes and the perpendicular direction. A model with anisotropic exchange is reduced to ours by renormalizing the length scale for one of the two nonequivalent directions.

The interdiffusion of atoms of the neighboring layers results in mere renormalization of the $J_{f,af}$ constant, provided that the mixing zone encloses one or two monolayers, i.e., is of atomic-scale width. The value of this constant is determined by microcalculations [5].

Although Eqs. (2) and (3) are written in the exchange approximation, it is straightforward to generalize them to systems with weak anisotropy in the layer planes.

Therefore, the suggested model allows the qualitative description of the magnetic characteristics of multilayer ferromagnet–antiferromagnet structures.

2. Thin ferromagnetic film on an antiferromagnet. Let us consider a thin ferromagnetic film of thickness a (in dimensionless units) on the surface of a layered antiferromagnet. Let the edges of the atomic steps be mutually parallel straight lines. The x-axis of the coordinate system lies in the layer plane perpendicular to the step edges, while the z-axis is perpendicular to the layers (the two-dimensional case). The numerical solution to the system of Eqs. (2) and (3) is obtained by method [6] similar to the method of integral transformations. The solution depends on the a value, the characteristic length R (dimensionless, in units of interatomic distance b) between the step edges, and the parameter

$$\alpha_f = J_{f,af}S_{af}/J_fS_f \qquad (5)$$

characterizing the ratio of exchange energies of the nearest lying spins belonging to the different layers and to the ferromagnetic layer, respectively.

Depending on the ratio of the indicated parameters, the film–substrate system may occur in different states. If the atomic steps at the interface are sufficiently far apart from each other, the frustrations induce the formation of magnetic domains in the film [2, 3]. The film magnetization in each domain is oriented in such a way as to minimize the boundary energy. Consequently, the magnetizations in the neighboring domains are antialigned. The structure of the Néel domain walls separating domains essentially depends on the parameter

$$\gamma = J_fS_f^2/J_{af}S_{af}^2, \qquad (6)$$

which is equal to the ratio of exchange energies in the film and the substrate.

Earlier, we considered the case where the distortions of the order parameter in the substrate were negligible [6]. This approximation corresponds to $\gamma \ll 1$. In the case of an iron film on a chromium substrate, we are interested in, $\gamma \gg 1$ and the structure of domain wall is more complicated, because the distortions of the order parameter also spread to the substrate.

If $\gamma^2 a\alpha_f \ll 1$, the distortions in the substrate are small and the domain wall width is equal to

$$\delta_f \approx (a/\alpha_f)^{1/2}, \qquad (7)$$

while its energy per unit length is

$$w \approx \frac{J_fS_f^2}{b}(a\alpha_f)^{1/2} \sim \frac{S_f}{b}(aJ_fJ_{f,af}S_fS_{af})^{1/2}. \qquad (8)$$

At $\gamma^2 a\alpha_f \gg 1$, two characteristic lengths appear:

$$\delta_0^{af} \approx (1 + \gamma\alpha_f)/\gamma\alpha_f \qquad (9)$$

and the domain wall width in the ferromagnetic layer

$$\delta_f \approx \gamma a, \qquad (10)$$

with $\delta_f \gg \delta_0^{af}$. Since $\delta_f \gg a$, the domain wall widening in the ferromagnetic layer can be ignored.

Let now consider the behavior of the antiferromagnetic parameter and the situation at the film–substrate interface. Let the edge of atomic step at the interface coincide with the *y*-axis of the Cartesian system. If $x \ll -\delta_f$, then the conditions $\theta_{af} = \theta_f = 0$ are fulfilled; and if $x \gg \delta_f$, then $\theta_{af} = 0$ and $\theta_f = \pi$. It follows from the symmetry considerations that $\theta_{af} = 0$ and $\theta_f = \pi/2$ at $x = 0$. The width of the film–substrate interface area where the $\theta_f - \theta_{af}$ value differs from its optimum value (0 at $x < 0$ and π at $x > 0$) is equal to δ_0^{af}. In the region $|x| \lesssim \delta_f$ and $|z| \lesssim \delta_f$, the order parameter in the substrate is distorted (Fig. 1a). The corresponding wall energy per unit length is equal to

$$w = \frac{\pi}{2}\frac{J_{af}S_{af}^2}{b}\ln\frac{\delta_f}{\delta_0^{af}}, \quad (11)$$

with the main contribution coming from the distortions of the order parameter in the substrate.

The above estimates relate to the case where the separation between the steps is large enough. As the separation R between the steps decreases and reaches a critical value $R_c \approx \delta_f$, the domain walls start to overlap and the film forms a single magnetic domain. If $\gamma^2 a\alpha_f \ll 1$ and $R \ll \delta_f$, the distortions are small in both film and substrate.

Finally, if $\gamma^2 a\alpha_f \gg 1$ and R falls in the range $\delta_0^{af} \ll R \ll \delta_f$, static spin vertices are formed in the substrate near the film boundary (Fig. 1b) at $|z| \lesssim R$. At smaller R values, the system is weakly distorted.

As is mentioned above, the steps divide the whole interface into regions of two types. Whereas the mean magnetization of the ferromagnetic film forms an angle of ψ with the antiferromagnetic order parameter in the substrate bulk, θ_{af} changes from zero to ψ in a vortex occupying a region of the first type and from ψ to π for the vertices in regions of the second type.

By analogy with the Slonczewski "magnetic proximity" model [7], the energy of the system can be written as

$$W = C_1\psi^2 + C_2(\pi - \psi)^2, \quad (12)$$

where the ratio of phenomenological constants C_1 and C_2 is proportional to the ratio of areas occupied by regions of both types. If the size distribution and the frequency of occurrence are the same for both types, then

$$C_1 = C_2 \approx \frac{\pi}{2}\frac{J_{af}S_{af}^2}{b}\ln\frac{R}{\delta_0^{af}}. \quad (13)$$

Without regard for the step-induced anisotropy energy, the equilibrium film magnetization in both the vortex phase and the weak-distortion region should be perpendicular to the antiferromagnetic order parameter.

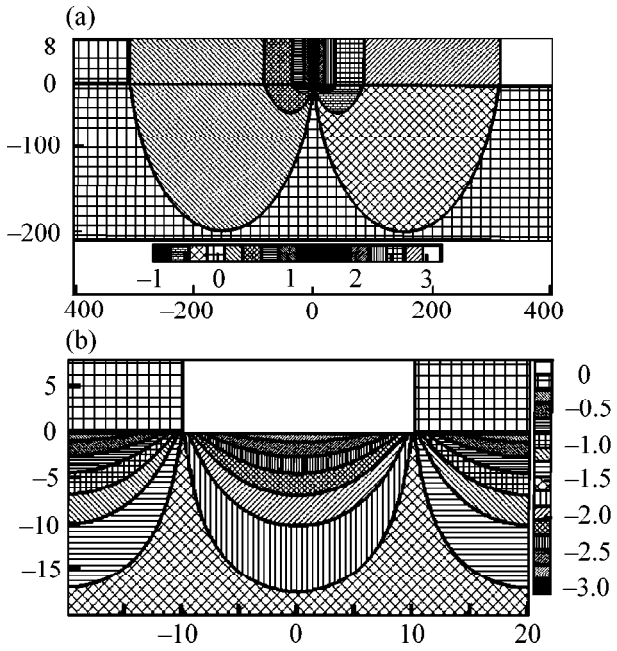

Fig. 1. Order parameter distributions in (a) domain wall and (b) vortex phase. Zero ordinate corresponds to the film–substrate interface. All distances are given in lattice constants. The ratio between the hatching and the θ_i value in radians is shown in the inset.

This picture is consistent with the results of work [4] devoted to studying the phase diagram "thickness–vicinal angle (β)" for the iron film on Cr (001). For β values close to zero, a multidomain phase was observed in films of thicknesses $a < a_c = 3.5$ nm. In a film of critical thickness a_c, the characteristic distance R between the edges of randomly distributed steps corresponds to the γa value. At larger a values, a single-domain phase with magnetization aligned perpendicular to the step edges was observed. According to the theory presented above, the antiferromagnetic vector should be parallel to the steps. It would be of interest to experimentally determine its orientation.

At $\beta \neq 0$, the randomly distributed atomic steps are complemented by regularly arranged parallel steps. As their concentration becomes dominant ($\beta \geq 1°$), the α_c value starts to decrease. According to our theory, $a_c \approx R/\gamma \propto \tan^{-1}\beta \propto \beta^{-1}$.

At larger β values, an orientational phase transition into a phase with magnetization parallel to the steps was observed in [4]. It is due to the step-induced anisotropy caused by the relativistic effects, e.g., dipole–dipole interactions [8].

The main results and conclusions of this work can be summarized as follows.

(1) A simple model is proposed allowing the determination of spin distribution in frustrated layered ferromagnet–antiferromagnet structures.

(2) A "thickness–roughness" phase diagram is obtained for a thin ferromagnetic film on an antiferromagnetic substrate.

(3) The transition from a multidomain state of ferromagnetic layers to the single-domain state proceeds smoothly with decreasing separation between the atomic steps at the interface, but it is not a phase transition in the strict sense of this word.

This work was supported in part by the Russian Foundation for Basic Research, project no. 00-02-17162.

REFERENCES

1. M. N. Baibich, J. M. Broto, A. Fert, *et al.*, Phys. Rev. Lett. **61**, 2472 (1988).
2. A. Berger and H. Hopster, Phys. Rev. Lett. **73**, 193 (1994).
3. E. J. Escorcia-Aparicio, H. J. Choi, W. L. Ling, *et al.*, Phys. Rev. Lett. **81**, 2144 (1998).
4. E. J. Escorcia-Aparicio, J. H. Wolfe, H. J. Choi, *et al.*, Phys. Rev. B **59**, 11892 (1999).
5. M. Freyss, D. Stoeffler, and H. Dreyssé, Phys. Rev. B **56**, 6047 (1997).
6. V. D. Levchenko, A. I. Morozov, A. S. Sigov, and Yu. S. Sigov, Zh. Éksp. Teor. Fiz. **114**, 1903 (1998) [JETP **87**, 985 (1998)].
7. J. C. Slonczewski, J. Magn. Magn. Mater. **150**, 13 (1995).
8. R. Arias and D. L. Mills, Phys. Rev. B **59**, 11871 (1999).

Translated by V. Sakun

JETP Letters, Vol. 71, No. 9, 2000, pp. 377–379. Translated from Pis'ma v Zhurnal Éksperimental'noĭ i Teoreticheskoĭ Fiziki, Vol. 71, No. 9, 2000, pp. 550–553.

CONDENSED MATTER

Anomalous Magnetic-Field Effect on the Thermal Expansion of $Ba_{1-x}K_xBiO_3$, $BaPb_xBi_{1-x}O_3$, and $La_{2-x}Sr_xCuO_4$ at Low Temperatures

N. V. Anshukova*, A. I. Golovashkin*, L. I. Ivanova, I. B. Krynetskiĭ***, and A. P. Rusakov****

** Lebedev Institute of Physics, Russian Academy of Sciences, Leninskiĭ pr. 53, Moscow, 117924 Russia*
e-mail: golov@sci.lebedev.ru
*** Moscow Institute of Steel and Alloys, Leninskiĭ pr. 4, Moscow, 117936 Russia*
**** Moscow State University, Vorob'evy gory, Moscow, 119899 Russia*
Received January 20, 2000; in final form, March 23, 2000

The anomalous magnetic-field effect on the thermal expansion of the BaKBiO, BaPbBiO, and LaSrCuO systems was observed at low temperatures. The effect is explained by superstructural ordering in the oxygen sublattices of these systems and its suppression in a magnetic field. © *2000 MAIK "Nauka/Interperiodica".*

PACS numbers: 72.15.Jf; 65.70.+y

Many properties of the $Ba_{1-x}K_xBiO_3$ (BKBO) and $BaPb_xBi_{1-x}O_3$ (BPBO) systems are similar to the properties of high-temperature superconducting (HTSC) cuprates [1–3], in spite of the fact that these systems are dominated by the Bi–O bonds, in contrast to the cuprate Cu–O bonds. It was demonstrated in [2, 3] that this similarity is largely due to superstructural ordering in the oxygen sublattices of both cuprate and bismuthate compounds. A physical model suggested in [2, 3] for such superstructural oxygen sublattice ordering (aside from the well-known ordering in the Cu and Bi sublattices) was recently experimentally justified by neutron diffraction studies [4].

Anomalous (negative) thermal expansion at low temperatures is among the properties that are common to both systems (cuprate and bismuthate). This effect was observed only for high-quality BKBO [1], BPBO [5], $La_{2-x}Sr_xCuO_4$ (LSCO) [1], $YBa_2Cu_3O_{7-x}$ [6], and $Bi_2Sr_2CaCu_2O_8$ [7–9] samples. In this work, the anomalously strong magnetic-field effect on the thermal expansion of the $Ba_{0.6}K_{0.4}BiO_3$, $La_{1.9}Sr_{0.1}CuO_4$, and $BaPb_{0.75}Bi_{0.25}O_3$ compounds was observed at low temperatures in the range H = 2–4 T. The effect was observed for polycrystalline BKBO samples with cubic symmetry, for a BPBO polycrystal, and for a single-crystal LSCO sample.

The synthesis of the samples and their certification were described in [1]. An analysis of the BKBO and BPBO samples on a LAMMA-1000 laser microprobe mass spectrometer with a sensitivity threshold of 10^{17} cm^{-3} did not detect even traces of copper or magnetic contamination. The linear thermal expansion $\Delta L/L$ was measured using a tensometric dilatometer with sensitivity of ~10^{-7} (L is the sample length) [10].

The dependences of $\Delta L/L$ on temperature T are displayed in Figs. 1 and 2 for two $Ba_{0.6}K_{0.4}BiO_3$ samples in different magnetic fields. The magnetic field in these measurements was perpendicular to the direction in which the deformation was measured. One can see that the temperature T^* corresponding to the minimum of $\Delta L/L$ decreases in the fields H = 2–4 T. In addition, the anomalous (negative) thermal expansion coefficient α decreases with an increase in H. A change in the $\Delta L/L$ value was observed in the fields H = 2–4 T for both the

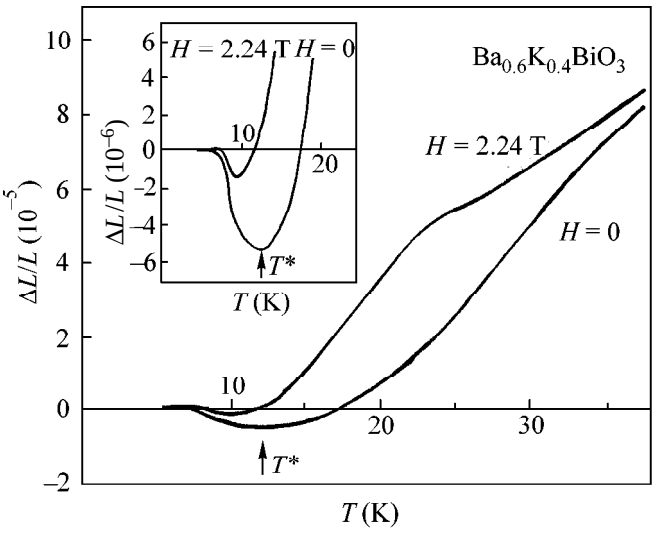

Fig. 1. Temperature dependences of the thermal expansion $\Delta L/L$ for $Ba_{0.6}K_{0.4}BiO_3$ sample no. 1 at H = 0 and 2.24 T. The functions $\Delta L/L$ at low temperatures T < 20 K are shown in the inset. The temperature T^* corresponds to the minimum of $\Delta L/L$.

0021-3640/00/7109-0377$20.00

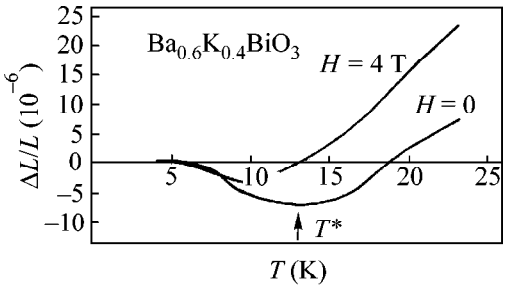

Fig. 2. Temperature dependences of $\Delta L/L$ for $Ba_{0.6}K_{0.4}BiO_3$ sample no. 2 at $H = 0$ and 2.24 T.

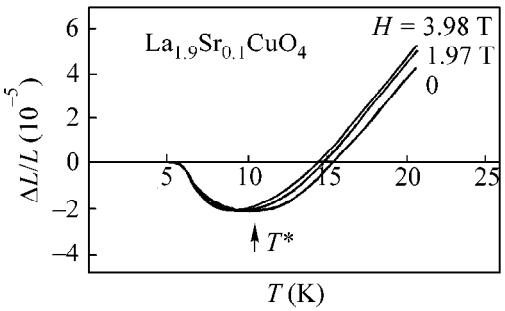

Fig. 3. Temperature dependences of the thermal expansion $\Delta L/L$ for the $La_{1.9}Sr_{0.1}CuO_4$ single crystal at $H = 0$, 1.97, and 3.98 T.

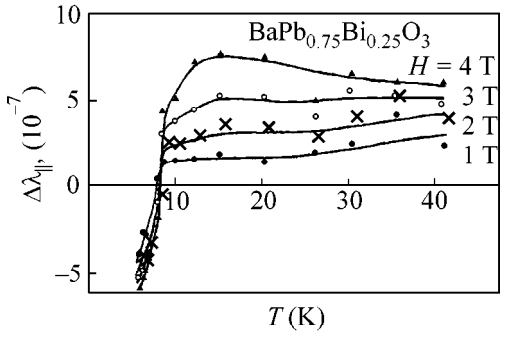

Fig. 4. Temperature dependences of the relative change in $\Delta L/L$ for $BaPb_{0.75}Bi_{0.25}O_3$ at four H values.

superconducting and normal metallic states of BKBO below $T \approx 50$ K. Considering that the temperature of transition to the superconducting state for BKBO is $T_c \leq 30$ K, the observed effect cannot be assigned to the ordinary magnetostriction of a superconductor.

An analogous magnetic-field–induced change in $\Delta L/L$ was observed at $H = 2$–4 T for the single-crystal $La_{1.9}Sr_{0.1}CuO_4$ sample. In the chosen geometry, the deformation was measured perpendicularly to the c axis of a single crystal, while the magnetic field was parallel to the direction in which the deformation was measured. The results are presented in Fig. 3. As seen from Fig. 3, the minimum of $\Delta L/L$ undergoes a low-temperature shift of 1.5–2 K with an increase in H to $H \approx 4$ T.

For the $BaPb_{0.75}Bi_{0.25}O_3$ compound, the magnetostriction $\lambda_{\|} = \lambda(H) = \Delta L/L(H)$ was measured as a function of H at a fixed temperature. Measurements were made in the fields parallel to the measured deformation. These data were used to construct the curves for the relative change $\Delta\lambda_{\|} = \Delta L/L(H) - \Delta L/L(0)$ in the temperature range 6 K $\leq T \leq$ 41 K, shown in Figs. 4 and 5 for four H values. The curves reflect the H-dependence not of the thermal expansion $\Delta L/L(H)$ but of the relative change in this value at a fixed temperature. It is seen that the relative change $\Delta L/L$ in the field H is appreciable at $T > T_c$ in the normal metal state. Another interesting feature is that the sign of $\Delta\lambda_{\|}$ changes at $T \approx 8$ K. These data are indicative of the more complicated behavior of the BPBO sample in a magnetic field.

We attribute the observed strong magnetic-field effect on thermal expansion to the field-induced decrease in lattice stability. It is known that the temperature dependence of the thermal expansion coefficient α is governed by the Grüneisen parameter γ, i.e., the logarithmic derivative of phonon frequencies with respect to the sample volume. The positive α values correspond to positive γ, i.e., to the increase in phonon frequency with temperature T. The negative α values observed for the HTSC oxide systems indicate that their phonon spectra have anomalous branches whose frequencies decrease with elevating temperature [1, 2, 4]. The fact that $\alpha < 0$ is observed at low temperatures is evidence that $\gamma < 0$ corresponds to the lowest frequency phonon branch [11], i.e., to the transverse acoustic mode ω_{TA}. Considering, first, that the phonon density of states for $\omega_{TA}(\mathbf{Q})$ is maximum near the Brillouin zone boundary and, second, that the superstructural ordering in the oxygen sublattice occurs [2–4] in the [100] direction, one can assert that $\omega_{TA}(\mathbf{Q})$ is anomalous for the wave vectors $\mathbf{Q}$ in the vicinity of the wave vector $\mathbf{Q}_n = (\pi/a)[100]$. Therefore, the "anomalous" phonons are transverse acoustic phonons with frequencies $\omega_{TA}(\mathbf{Q})$ and wave vectors $\mathbf{Q} \approx \mathbf{Q}_n$ near the Brillouin zone boundary. The BKBO and LSCO experiments showed that the temperature T^* corresponding to the minimum value of $\Delta L/L$ decreases with increasing H. Since $kT^* \sim \omega_{TA}(\mathbf{Q}_n)$, this implies that $\omega_{TA}(\mathbf{Q}_n)$ decreases with increasing H. Thus, the crystal instability increases with H; i.e., $\omega_{TA} \longrightarrow 0$.

At the same time, the superstructural ordering in the oxygen sublattice (i.e., ordering of the oxygen ions with different valences; more precisely, ordering of the ionic–covalent Cu–O or Bi–O bonds [2–4]) is equivalent to the appearance of a charge-density wave (CDW) in this sublattice. The CDW amplitude is proportional to $\omega_{TA}(\mathbf{Q}_n)$ [2]. Such a CDW ensures lattice stability; i.e., $\omega_{TA}(\mathbf{Q}_n) > 0$. Thus, the experimental results (a decrease in T^* and ω_{TA} with an increase in H) suggest that the magnetic field reduces the CDW amplitude.

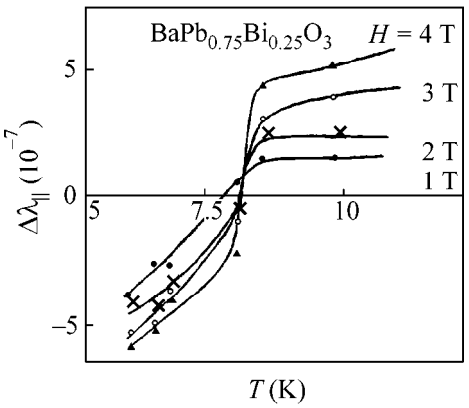

Fig. 5. Temperature dependences of the relative change in $\Delta L/L$ for $BaPb_{0.75}Bi_{0.25}O_3$ at four H values in the low-temperature range $T \leq 10$ K.

The magnetic-field effect on the thermal expansion anomaly is analogous to the heavy-doping effect [2]. In our opinion, such a magnetic-field effect on the CDW amplitude in the oxygen sublattice is caused by breaking the electron–hole pairs, which appear in the HTSC oxides because of the specificity of their electronic structure [2], and ensuing strengthening of the CDW screening by free charge carriers.

In summary, an anomalously strong magnetic-field effect on the thermal expansion of HTSC oxide systems was observed. The effect is attributed to the field-induced decrease in the amplitude of a lattice-stabilizing CDW in the oxygen sublattice, causing an anomalous thermal expansion at lower temperatures.

We are grateful to L.I. Leonyuk for providing us with single-crystal LaSrCuO samples. This work was supported by the Scientific Council of the State Scientific and Technical Program "Topical Directions in Physics of Condensed Matter" ("Superconductivity" subprogram).

REFERENCES

1. N. V. Anshukova, A. I. Golovashkin, L. I. Ivanova, *et al.*, Physica C (Amsterdam) **282–287**, 1065 (1997).
2. A. I. Golovashkin, N. V. Anshukova, L. I. Ivanova, and A. P. Rusakov, Physica C (Amsterdam) **317–318**, 630 (1999).
3. A. I. Golovashkin, N. V. Anshukova, L. I. Ivanova, and A. P. Rusakov, Int. J. Mod. Phys. B **12**, 2999 (1998).
4. R. J. McQueeney, Y. Petrov, T. Egami, *et al.*, Phys. Rev. Lett. **82**, 628 (1999).
5. N. V. Anshukova, A. I. Golovashkin, L. I. Ivanova, *et al.*, Int. J. Mod. Phys. B **12**, 3251 (1998).
6. H. You, U. Welp, and Y. Fang, Phys. Rev. B **43**, 3660 (1991).
7. M. Mouallem-Bahout, J. Gaude, G. Calvarin, *et al.*, Mater. Lett. **18**, 181 (1994).
8. Z. J. Yang, M. Yewondwossen, D. W. Lawther, *et al.*, J. Supercond. **8**, 233 (1995).
9. T. Asahi, H. Suzuki, M. Nakamura, *et al.*, Phys. Rev. B **55**, 9125 (1997).
10. N. V. Anshukova, Yu. V. Boguslavskiĭ, A. I. Golovashkin, *et al.*, Fiz. Tverd. Tela (St. Petersburg) **35**, 1415 (1993) [Phys. Solid State **35**, 714 (1993)].
11. H. Wendel and R. M. Martin, Phys. Rev. B **19**, 5251 (1979).

Translated by V. Sakun

JETP Letters, Vol. 71, No. 9, 2000, pp. 380–382. Translated from Pis'ma v Zhurnal Éksperimental'noĭ i Teoreticheskoĭ Fiziki, Vol. 71, No. 9, 2000, pp. 554–557.

CONDENSED MATTER

Dynamic Shift of the Phase-Transition Temperature in $(Sn_{1-x}In_{(2/3)x})_2P_2S_6$ Crystals with Incommensurate Phase

P. P. Guranich, P. M. Lukach, V. V. Tovt, E. I. Gerzanich, A. G. Slivka, V. S. Shusta, and V. M. Kedyulich

Uzhgorod State University, Podgornaya ul. 46, Uzhgorod, 294000 Ukraine

e-mail: optics@univ.uzhgorod.ua

Received March 23, 2000

The dielectric properties of ferroelectric $(Sn_{1-x}In_{(2/3)x})_2P_2S_6$ crystals were studied in the region of incommensurate phase transitions occurring upon fast cooling and heating (0.2–11 K/min). The dynamic phase-transition shift observed in these materials was examined. © *2000 MAIK "Nauka/Interperiodica".*

PACS numbers: 64.70.Rh; 77.22.-d

To date, the phenomenon of dynamic phase-transition (PT) temperature shift in the domain of existence of modulated structures has been studied for Ag_3AsS_3 [1, 2] and $Sn_2P_2Se_6$ [3] crystals. Owing to the difference in the PT temperature-shift coefficients for the cooling and heating regimes, an inverted PT hysteresis (as wide as 15 K for rates of 6.8 K/min in proustite crystals) is observed in these systems. Although the nature of these phenomena remains to be clarified, several attempts to explain them were undertaken, e.g., by the influence of electronic subsystem in semiconductor ferroelectrics [3] or by the occurrence of a nonuniform heating–induced internal stress in ferroelectrics [4]. It is worth noting that the number of objects exhibiting inverted hysteresis is as yet quite limited. The question also arises of whether these phenomena are typical only of the incommensurate structures or they have the more general character.

This work presents the results of experimental studies of the dynamic PT temperature shift and the properties of the inverted hysteresis in ferroelectric $(Sn_{1-x}In_{(2/3)x})_2P_2S_6$ crystals—new objects whose p, T diagrams contain both commensurate and incommensurate PT regions.

Single crystals of $(Sn_{1-x}In_{(2/3)x})_2P_2S_6$ (x = 0.028, 0.05, and 0.07) were grown by gas-transport reaction using iodine as a transporting agent. The sample dimensions were ca. 8 mm. The crystals were colored light orange, typical of $Sn_2P_2S_6$. For the dielectric measurements, silver contacts were applied to the plane-parallel faces that were cut perpendicularly to the polar direction. The studies of the dielectric constant ϵ and the dielectric-loss tangent $\tan\delta$ were carried out at a frequency of 1 MHz in the dynamic mode with controlled temperature-variation rate in the range 0.2–20 K/min. The sample for measurements was placed in a high-hydrostatic-pressure chamber. Kerosene was used as a pressure-transmitting medium. The temperature was measured with a copper–constantan thermocouple. To reduce temperature gradients to a minimum, the sample was heated and cooled together with the chamber.

The $(Sn_{1-x}In_{(2/3)x})_2P_2S_6$ crystals are ferroelectric (of the displacement type) solid solutions based on tin hexathiohypodiphosphate. They were identified as substitutional solid solutions with subtraction. The substitution of indium for tin is accompanied by the appearance of vacancies in the tin sublattice ($3Sn^{2+} \longrightarrow 2In^{3+}$). A series of solid solutions were limited by the concentration $x \approx 0.07$. High-hydrostatic-pressure studies of the PTs in these crystals [5] showed that the ferroelectric PT at T_0 splits into two phase transitions occurring at $p = p_L \approx 200$ MPa at T_i and T_c to form an incommensurate (IC) phase (with temperature width $T_i - T_c = 15$ K at a pressure of $p = 400$ MPa for $x = 0.028$). It was found that the phase-transition temperature in the domain of existence of the incommensurate PTs strongly depends on the cooling and heating rates and that an inverted hysteresis appears. We will exploit the term "inverted hysteresis," because, in our opinion, it adequately reflects the external manifestations of this phenomenon, namely, the fact that the PT temperature on heating is lower than the PT temperature on cooling, owing to the difference in the dynamic shift dT_c/dV for the cooling and heating regimes.

At pressures $p > p_L$, where the incommensurate PTs occur, the temperature dependences of ϵ were examined for an $(Sn_{1-x}In_{(2/3)x})_2P_2S_6$ ($x = 0.028$) crystal at different temperature-variation rates V (Fig. 1). One can see that an increase in the rate of temperature variation results in shifting of the ϵ maximum to high temperatures for both cooling $T = T_c^c$ and heating $T = T_c^h$, with different coefficients $dT_c^c/dV > dT_c^h/dV$. The $T_c^c - T_c^h$ difference reaches 15 K at a rate of $V = 11$ K/min. Thus,

0021-3640/00/7109-0380$20.00

the inverted PT hysteresis at T_c becomes more pronounced with increasing V. The temperature T_i of the paraelectric phase–incommensurate phase transition shifts analogously to T_c, which is also typical of Ag_3AsS_3 crystals [1].

At a fixed rate of temperature variation, inverted hysteresis in the crystals being studied was observed only at pressures $p > p_L$, i.e., in the p range where the incommensurate PTs occur. It is worth noting that the magnitude of the effect smoothly increases upon moving away from the splitting point. This suggests that inverted hysteresis can be observed only for the IC structures. It should also be noted that inverted hysteresis was not detected for pure $Sn_2P_2S_6$ crystals even in the domain of existence of the IC phase at $p > p_L$. The presence of In ions apparently stimulates the appearance of inverted hysteresis.

It was found that the magnitude of the inverted hysteresis in the $(Sn_{1-x}In_{(2/3)x})_2P_2S_6$ crystals does not depend on the temperature T_R of passing from the cooling to the heating regime, provided that T_R is outside the $T_c^h - T_c^c$ interval. Near the temperature T_R, the $\epsilon(T)$ curves form loops corresponding to the transition from the cooling to the heating curve. Of particular interest is the case when one passes from the cooling to the heating regime at temperatures below T_c^c but above T_c^h (Fig. 2). The shapes of the corresponding curves in the immediate vicinity of temperature $T = T_R$ are noteworthy. Inasmuch as, experimentally, one cannot instantaneously pass from cooling to heating, there is a certain temperature range (denoted by *1* in Fig. 2) where the $V = dT/dt$ value changes sign (i.e., decreases, passes through zero, and again increases but with opposite sign). As seen in Fig. 2, the $\epsilon(T)$ curve in this region exhibits an additional maximum that is associated with the reverse transition of the crystal to the initial high-temperature phase $T = T_{c2}$. Therefore, on cooling, the crystal undergoes two PTs: the first one at T_{c1} from the high-temperature to the ferroelectric phase and the second, reverse transition, at T_{c2} from the ferroelectric to the "high-temperature" phase. Upon a further rise in temperature, the $\epsilon(T)$ curve merges with the heating curve corresponding to the chosen V value. The occurrence of the second anomaly in the temperature dependence of ϵ in the region where the cooling rate decreases becomes understandable from Fig. 3. The $V(T)$ curve shows schematically a change in V with temperature for such an experiment. This curve twice intersects the $T_c^c(V)$ curve, and the points of intersection correspond to two PTs. Clearly, by changing V in a more intricate fashion, one can obtain a series of successive PTs. It should be noted that such a pattern can only be observed if the relaxation time of the metastable state is very short. This differentiates the above crystals from proustite [6].

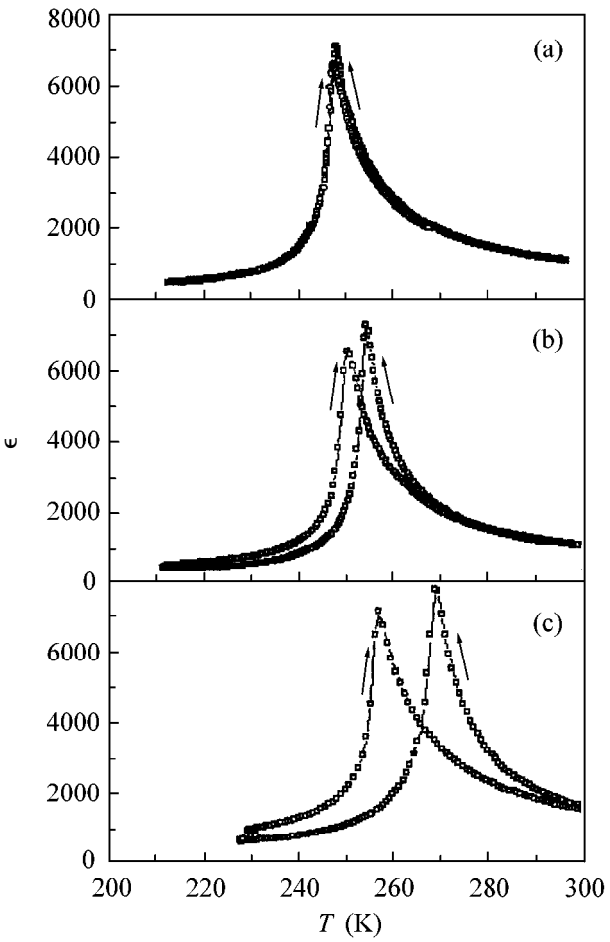

Fig. 1. Temperature dependence of ϵ for the $(Sn_{1-x}In_{(2/3)x})_2P_2S_6$ (x = 0.028) crystal at a pressure of 415 MPa and different rates of temperature variation: (a) 0.8, (b) 3.3, and (c) 10 K/min.

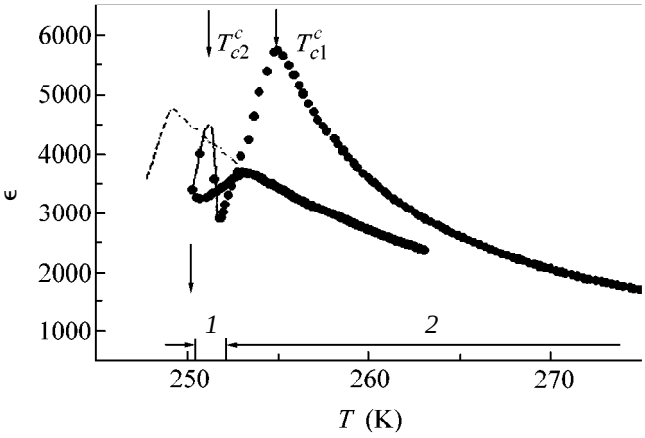

Fig. 2. Temperature dependence of ϵ for the $(Sn_{1-x}In_{(2/3)x})_2P_2S_6$ (x = 0.028) crystal upon passing from cooling to heating at temperature T_R ($T_c^c < T_R < T_c^h$). The dot-and-dash curve is for the $\epsilon(T)$ dependence corresponding to heating at a given rate V. Temperature ranges are (*1*) $V \neq$ const and (*2*) V = const.

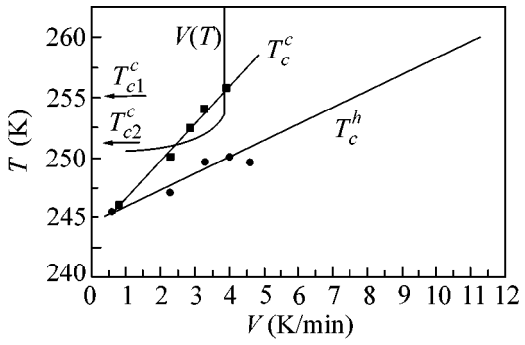

Fig. 3. The PT temperatures on cooling, T_c^c, and heating, T_c^h, as functions of the rate V of temperature variation for the $(Sn_{1-x}In_{(2/3)x})_2P_2S_6$ ($x = 0.028$) crystal at $p = 415$ MPa.

Compared to Ag_3AsS_3 and $Sn_2P_2Se_6$, the dynamic shift of PT temperatures in $(Sn_{1-x}In_{(2/3)x})_2P_2S_6$ has its own specificities. A substantial PT temperature shift in $(Sn_{1-x}In_{(2/3)x})_2P_2S_6$ occurs at the rates $V = 0.2$–10 K/min, in contrast to $Sn_2P_2Se_6$, where V is higher by an order of magnitude [3]. An increase in V brings about an increase in both T_c^c and T_c^h, whereas the PT temperature for Ag_3AsS_3 and $Sn_2P_2Se_6$ decreases upon heating [3, 6]. The studies of the inverted PT hysteresis in these crystals indicate that this phenomenon is typical only of the incommensurate structures.

REFERENCES

1. N. S. Afonikova, S. S. Khasanov, and I. M. Shmyt'ko, Pis'ma Zh. Éksp. Teor. Fiz. **41**, 256 (1985) [JETP Lett. **41**, 314 (1985)].
2. B. Sh. Bagautdinov and I. M. Shmyt'ko, Pis'ma Zh. Éksp. Teor. Fiz. **59**, 171 (1994) [JETP Lett. **59**, 182 (1994)].
3. Yu. S. Greznev, R. F. Mamin, and S. F. Motrya, Fiz. Tverd. Tela (St. Petersburg) **35**, 96 (1993) [Phys. Solid State **35**, 51 (1993)].
4. V. M. Rudyak and N. N. Bol'shakova, Kristallografiya **39**, 93 (1994) [Crystallogr. Rep. **39**, 82 (1994)].
5. P. P. Guranich, P. M. Lukach, V. V. Tovt, *et al.*, Fiz. Tverd. Tela (St. Petersburg) **41**, 1276 (1999) [Phys. Solid State **41**, 1166 (1999)].
6. I. M. Shmyt'ko, N. S. Afonikova, and N. A. Dorokhova, Fiz. Tverd. Tela (St. Petersburg) **40**, 2217 (1998) [Phys. Solid State **40**, 2013 (1998)].

Translated by V. Sakun

JETP Letters, Vol. 71, No. 9, 2000, pp. 383–386. Translated from Pis'ma v Zhurnal Éksperimental'noĭ i Teoreticheskoĭ Fiziki, Vol. 71, No. 9, 2000, pp. 558–563.

CONDENSED MATTER

Anomalous Fluctuations of 2D-Electron Recombination Radiation Intensity in the Quantum Hall Regime

O. V. Volkov*, I. V. Kukushkin*, M. V. Lebedev*,
G. B. Lesovik, K. von Klitzing***, and K. Eberl*****

** Institute of Solid-State Physics, Russian Academy of Sciences, Chernogolovka, Moscow region, 142432 Russia*
e-mail: volkov@issp.ac.ru
*** Landau Institute of Theoretical Physics, Russian Academy of Sciences, Chernogolovka, Moscow region, 142432 Russia*
**** Max-Planck-Institut für Festkörperforschung, 70569 Stuttgart, Germany*
Received March 27, 2000

Anomalous intensity fluctuations are observed in the spectrum of radiative recombination of quasi-two-dimensional (2D) electrons with photoexcited holes in a single quantum well. The fluctuations are observed exclusively under the conditions of the quantum Hall effect (QHE). It is shown that, if the QHE conditions are not fulfilled, the radiation intensity fluctuates strictly following the Poisson distribution ($\langle\delta N^2\rangle/\langle N\rangle = 1$), whereas in the QHE regime the fluctuation amplitude increases by several orders of magnitude ($\langle\delta N^2\rangle/\langle N\rangle \sim 10^2$). It is demonstrated that the maxima of the emission noise amplitude coincide with the maxima of inverse magnetoresistance of 2D electrons in the QHE regime and correspond to establishing an anomalously high uniformity of the system. © *2000 MAIK "Nauka/Interperiodica".*

PACS numbers: 73.20.Dx; 73.40.Hm; 78.66.-w; 05.40.-a

1. It is well known that the statistical characteristics of quantum objects largely govern the properties of the physical system they comprise. Photon statistics is one such important and experimentally well-studied characteristic. If the individual photon-emission events are statistically independent, the number N of photons on a detector obeys the well-known Poisson statistics, for which the mean-square deviation (variance) $D = \langle\delta N^2\rangle = \langle N^2\rangle - \langle N\rangle^2$ coincides with the mean value $\langle N\rangle$. At the same time, if the elements of a photoexcited system strongly interact with each other, so that the characteristic correlation length is comparable with the separation between the recombining particles, the statistical independence of photons is violated, thus making possible the observation of appreciable deviations of photon statistics from the Poisson description.

A system of quasi-two-dimensional (2D) electrons in a perpendicular magnetic field is among the objects in which the strong correlation effects may occur. This is precisely the system where the fractional quantum Hall effect (QHE) and Wigner crystallization, i.e., phenomena based exclusively on the electron–electron interaction, were discovered. In recent years, there has been much discussion of the possibility of explaining the QHE by the formation of a strongly correlated state analogous to a second-kind superconductor [1]. Electron pairing can be assisted not only by the three-dimensional phonons but also by the surface 2D phonons or 2D plasmons [2]. The formation of a coherent superconducting condensate or another strongly correlated state should be manifested in the fluctuations of the physical parameters of a system. It is the studies of electric noise that made it possible to reveal the fractional electron effective charge [3]. Nevertheless, the fluctuations in the luminescence spectra have not been investigated so far, although the optical methods of studying the QHE in a 2D electron system provide information that is beyond the reach of the transport methods [4].

In this work, we report the observation of anomalously large intensity fluctuations of the radiative recombination of two-dimensional electrons confined to GaAs/AlGaAs quantum wells. It is shown that beyond the QHE regime the emission intensity fluctuates strictly in accordance with the Poisson distribution, whereas, in the QHE regime, the fluctuation amplitude increases by several orders of magnitude. It is demonstrated that this is accompanied by establishment of an anomalously high uniformity of the 2D electron concentration, suggesting the formation of a strongly correlated electronic system in the QHE regime.

2. We investigated the radiative recombination of 2D electrons with photoexcited holes in a single high-quality heterojunction. The samples were grown by molecular-beam epitaxy on a GaAs substrate according to the following scheme: a 3000-Å-thick GaAs buffer layer, an undoped GaAs–$Al_{0.3}Ga_{0.7}As$ (30–100 Å) superlattice with a total thickness of 13000 Å, a 250-Å-wide GaAs quantum well, a 400-Å $Al_{0.3}Ga_{0.7}As$ spacer, and a 650-Å-thick $Al_{0.3}Ga_{0.7}As$: Si doped (at a level of 10^{18} cm^{-3}) layer. A characteristic mobility of 2D elec-

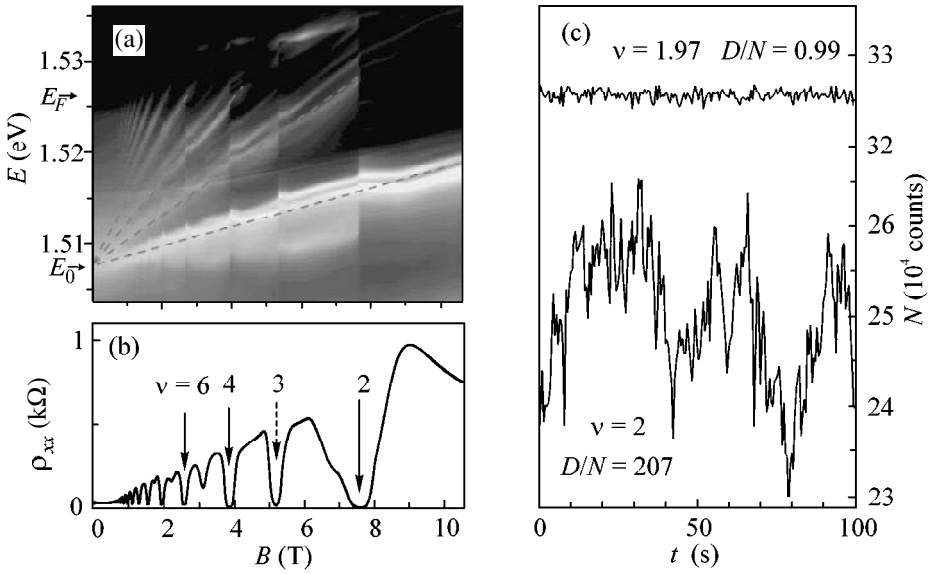

Fig. 1. (a) Diagram of luminescence spectra measured in the range of magnetic fields from 0 to 10.6 T. The color from black to white corresponds to the luminescence intensity from zero to its maximum value. (b) Shubnikov–de Haas oscillations measured under the same conditions as in (a). (c) Time dependences of the emission intensity for two different values of magnetic field in the vicinity of filling factor ν = 2; measurements are carried out for the maximum of emission line corresponding to the zero Landau level.

trons in these structures was 1.3×10^6 cm^2/(V s) at n_S = 3.8×10^{11} cm^{-2}. The system was optically excited by a laser diode with photon energy of 1.653 eV and output power time instability of less than 10^{-4}. A Ramanor U-1000 double monochromator was used as a spectral instrument providing spectral resolution of 0.03 meV. To record the radiative recombination spectrum and analyze the intensity fluctuations, a photon-counting photomultiplier and a semiconductor charge-coupled detector (CCD) were used; the results of both measurements fully coincided. The fluctuation amplitude was measured with a CCD detector by recording, under the same experimental conditions, 100 spectra that were thereafter used to determine (for every wavelength) the mean radiation intensity (the number of photon counts) ($\langle N \rangle$) and the mean-square deviation (variance) $D = \langle N^2 \rangle - \langle N \rangle^2$ of intensity. The transport characteristics of the samples were measured in parallel with the optical studies (under continuous laser illumination). The measurements were carried out at a low frequency (14 Hz), with the flowing current not exceeding 10 nA. To measure the magnetoresistance at the Shubnikov–de Haas oscillation minima corresponding to the QHE, electrometers with internal resistance of up to 10^{15} Ω were used. The experiments were conducted in the range of magnetic fields 0–10.6 T at a temperature of 1.5 K.

3. The diagram of the magnetic-field dependence of optical transition energies is shown in Fig. 1a for a sample studied in the range from 0 to 10.6 T. It represents a set of emission spectra measured at small steps of 0.1 T. The contrast in the diagram reflects the recombination intensity: the higher intensity corresponds to white, and the black color corresponds to a weak intensity. For clearness, linear approximations corresponding to different Landau levels of 2D electrons are shown in this panel by dashes; also indicated are the bottom E_0 of the lowest subband and the Fermi level E_F. It is seen in Fig. 1a that each filled Landau level appears in the optical spectra as several emission lines corresponding to different hole energy levels involved in the recombination [5]. Because of the complex structure of the valence band, a number of transitions from the same electronic Landau level to different hole Landau levels are allowed [6], resulting in the splitting of emission lines. To accurately control the 2D-electron filling factor (ν), we simultaneously carried out transport and optical measurements. Figure 1b shows the resistance of 2D electrons (ρ_{xx}) measured as a function of magnetic field under optical excitation conditions. One can see that the QHE is manifested in the transport measurements as the well-known deep ρ_{xx} minima and appears in the optical spectra as very sharp (on the magnetic-field scale) jumps in the spectral positions of all emission lines. The one-to-one correspondence between the transport and optical QHE manifestations for ν = 2, 3, 4, 6, and 8 is clearly seen from the comparison of Figs. 1a and 1b.

Statistical analysis of the time dependence of luminescence spectra suggests that, under rigorous QHE conditions, the intensity of radiative recombination of 2D electrons undergoes, for ν = 2, 4, 6, and 8, giant amplitude fluctuations that occur within an exceedingly narrow magnetic-field interval (0.02 T) and almost fully disappear upon moving away at only $\Delta\nu \sim 0.005$ (!)

from the integer filling factor. Figure 1c shows the time-dependent emission intensities measured with fixed experimental parameters at the maximum of the emission line corresponding to the lowest Landau level and to the filling factors $\nu = 1.97$ and 2. One can see that the fluctuation amplitude is small at $\nu = 1.97$ (the relative deviation from the mean value is $\delta N/N = \sqrt{D}/N \approx 0.002$) and the variance D fits the Poisson distribution $D/N \approx 1$. However, in spite of having nearly the same intensity, the relative fluctuation amplitude increases at $\nu = 2$ by more than an order of magnitude ($\delta N/N \approx 0.03$), while the variance by no means fits the Poisson distribution ($D/N = 207$).

A similar increase in the fluctuation amplitude under QHE conditions is observed not only for the emission line maximum but also throughout the emission spectrum. Figure 2 shows the energy-dependent luminescence intensity N (shown by grey) and variance D measured in magnetic fields $B = 0$ T and $B = 7.7$ T ($\nu = 2$). One can see that these quantities virtually coincide in zero magnetic field and that the emission statistics exactly fit the Poisson distribution at any wavelength. However, in the QHE regime ($\nu = 2$), the picture changes drastically and the energy dependences of luminescence intensity and variance become different: the variance is more than an order of magnitude in excess of the mean value at the emission line maximum, and the ratio of the N and D values satisfies the Poisson statistics only at the line wings.

4. At first sight, the anomalously large fluctuations of emission intensity could have been associated with the QHE-induced abrupt jumps of emission line positions or with the instability of the external magnetic field. However, this scenario is in conflict with the experimental evidence. First, fluctuations with the same amplitude were observed when the solenoid current was "frozen" with the help of a superconducting valve. Second, despite the fact that the spectral positions of emission lines undergo an abrupt jump at $\nu = 3$ similar to the features at $\nu = 2$, 4, 6, and 8 (Fig. 1a), we failed to detect the anomalous emission fluctuations for $\nu = 3$. And third, if the observed noise anomalies were caused by the jumps of emission lines, the fluctuation spectrum would not coincide with the luminescence spectrum (see Fig. 2b) but rather would be reminiscent of the squared derivative of the emission spectrum. Therefore, one is forced to conclude that the anomalous fluctuations observed for the 2D electron system are caused by a certain internal parameter that is appreciably different for $\nu = 2$ and $\nu = 3$ and is a sharp function of ν in the vicinity of $\nu = 2$. One can naturally assume that the inverse magnetoresistance of the 2D electron system is such a parameter. In Fig. 3, the measured magnetic-field dependence of $\ln(1/\rho_{xx})$ (upper curve) is compared with a similar dependence of the $\ln(D/N)$ parameter characterizing the emission intensity fluctuation amplitude (lower curve). The spikes at $\nu = 2$, 4, 6, and 8 exhibit remarkable similarity (in width and position) in the transport and optical measurements. In addition, it is seen from Fig. 3 that the anomalous fluctuations arise upon reaching a certain minimum $1/\rho_{xx}$ level. That is why the noise is not detected for $\nu = 3$ and $\nu = 10$, 12, ….

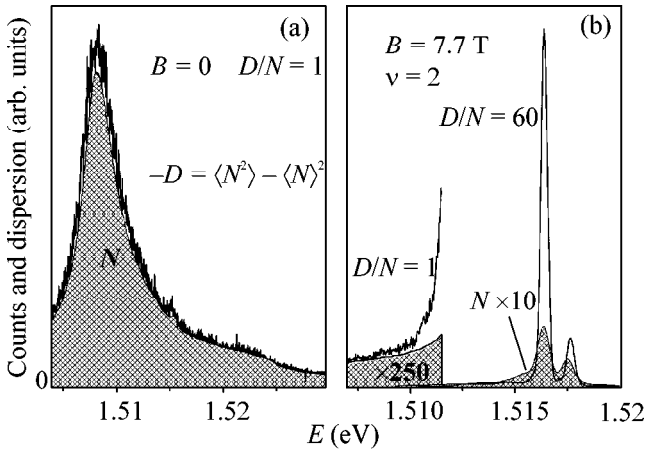

Fig. 2. Energy-dependent emission intensity N (shown by grey) and variance $D = \langle N^2 \rangle - \langle N \rangle^2$ measured (a) in zero magnetic field and (b) in the field $B = 7.7$ T corresponding to the filling factor $\nu = 2$.

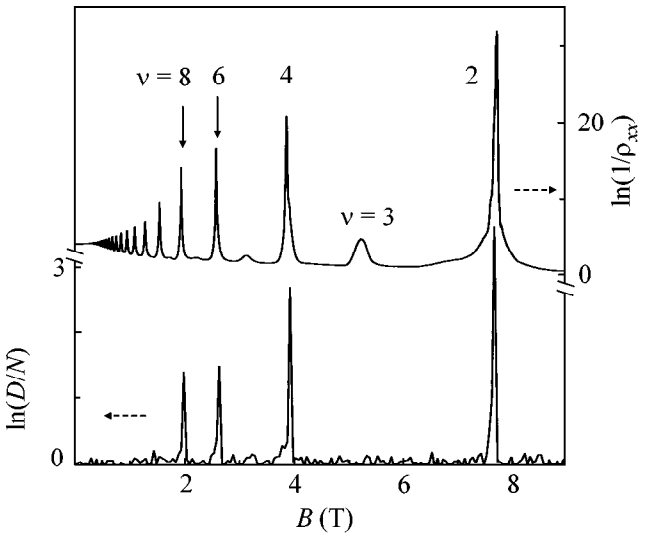

Fig. 3. A comparison of the magnetic-field dependences of the logarithms of (upper curve) the inverse longitudinal magnetoresistance $1/\rho_{xx}$ and (lower curve) variance-to-mean ratio D/N in the luminescence spectra.

The anomalously small widths of the spikes in the $\ln(D/N)$ vs. magnetic field curve (Fig. 3) call for special analysis, because they were found to be equal to the jumps of emission line positions (Fig. 1a). On the one hand, these jumps can uniquely be assigned to the chemical potential jumps between the Landau levels and, hence, the appearance (or disappearance) of electrons or "holes" at the upper Landau level. Accordingly,

the energy of the exciton formed by the photoexcited hole and the Fermi-level electrons alters. However, the occurrence of jumps as sharp as those observed in our work suggests that the 2D electron density of states (DOS) has a gap between the Landau levels, where the DOS is close to zero. The formation of such a gap can be caused, e.g., by the Coulomb repulsion of the equal-energy states (in the presence of a random potential) belonging to the different Landau levels. It is worth noting that direct transport measurements of the DOS between the Landau levels are hampered due to the low conductance of the system in the QHE regime and to edge effects. Nevertheless, the results obtained for structures of a considerably lower quality than ours are evidence that the DOS can reduce to almost zero at a magnetic field as low as 1.8 T (see Fig. 3b in [7]). On the other hand, observation of the features of relative width (on the magnetic-field scale) on the order of 10^{-3} is possible only if the degree of uniformity of the 2D electron concentration across the sample surface is as high as that. This is quite surprising, the more so as we did not take any care in making the optical excitation spatially uniform. It remains to assume the presence of a mechanism that levels off with a high degree of accuracy the concentration across the illuminated surface of the sample photoexcited under QHE conditions.

5. The following conclusions can be drawn from the statistical analysis of the recombination radiation spectra of a 2D electron gas.

- Photoexcitation at low temperatures gives rise to the gaps in the density of states between the Landau levels. The chemical potential undergoes jumps at the integer filling factors, while the inverse magnetoresistance $1/\rho_{xx}$ exhibits sharp maxima.
- The 2D electron concentration becomes anomalously uniform in the vicinity of the integer filling factors, so that the chemical potential jump occurs simultaneously throughout the sample within an exceedingly narrow ($\sim 10^{-3}$) range of filling factors.
- The recombination radiation intensity undergoes giant fluctuations in the magnetic-field range where the chemical potential jump occurs.

The phenomena observed in this work may be regarded as evidence for the formation of a strongly correlated electronic system in the QHE regime.

We are grateful to L.V. Kulik for helpful discussions. This work was supported by the Russian Foundation for Basic Research and the INTAS (grant no. 99-1146).

REFERENCES

1. L. B. Rigal, D. K. Maude, M. Potemski, *et al.*, Phys. Rev. Lett. **82**, 1249 (1999).
2. S. M. Girvin and A. H. MacDonald, Phys. Rev. Lett. **58**, 1252 (1987); R. B. Laughlin, Phys. Rev. Lett. **60**, 2677 (1988); S. C. Zhang, T. H. Hansson, and S. Kivelson, Phys. Rev. Lett. **62**, 82 (1989).
3. L. Saminadayar, D. C. Glattli, Y. Jin, and B. Etienne, Phys. Rev. Lett. **79**, 2526 (1997); G. de Picciotto, M. Reznikov, M. Heiblum, *et al.*, Nature **389**, 162 (1997).
4. I. V. Kukushkin and V. B. Timofeev, Adv. Phys. **45**, 147 (1996).
5. O. V. Volkov, V. E. Zhitomirskiĭ, I. V. Kukushkin, *et al.*, Pis'ma Zh. Éksp. Teor. Fiz. **65**, 38 (1997) [JETP Lett. **65**, 38 (1997)].
6. O. V. Volkov, V. E. Zhitomirskiĭ, I. V. Kukushkin, *et al.*, Phys. Rev. B **56**, 7541 (1997).
7. T. P. Smith, B. B. Goldberg, P. J. Stiles, *et al.*, Phys. Rev. B **32**, 2696 (1985).

Translated by V. Sakun

JETP Letters, Vol. 71, No. 9, 2000, pp. 387–390. Translated from Pis'ma v Zhurnal Éksperimental'noĭ i Teoreticheskoĭ Fiziki, Vol. 71, No. 9, 2000, pp. 564–569.

CONDENSED MATTER

Intersubband Resonance Polarons in Al/δ-GaAs Tunneling Junctions

I. N. Kotel'nikov*, **, V. A. Kokin*, Yu. V. Fedorov*, A. V. Hook*, and D. T. Talbaev*

** Institute of Radio Engineering and Electronics, Russian Academy of Sciences, Mokhovaya ul. 11, Moscow, 103907 Russia*
e-mail: igor@mail.cplire.ru

*** International Laboratory of High Magnetic Fields and Low Temperatures, 53-421 Wrocław, Poland*

Received March 29, 2000

Tunneling spectra of the Al/δ-GaAs junctions fabricated by molecular-beam epitaxy in the regime of "intimate" contact of Al with GaAs (100) were studied at 1.6 K in a magnetic field B parallel to the two-dimensional electron-gas layer. The concentration of 2D electrons in the δ-layer grown at a distance of 20 nm from the Al/GaAs interface was 1.1×10^{12} cm^{-2} and corresponded to a partial filling of only the lowest subband E_0. The tunneling spectra exhibited many-particle features, viz., a zero-bias anomaly, lines of longitudinal optical (LO) phonons, and characteristic "dips" corresponding to the energies E_i of the 2D subbands. In the B fields below the critical value $B_c \cong 11$ T, the levels of 2D subbands underwent the usual diamagnetic shifts. At $B \geq B_c$, the $E_1(B)$ term pinning and the anticrossing of the $E_1(B)$ and $E_0(B) + 2\hbar\omega_{LO}$ terms were observed, where $\hbar\omega_{LO}$ is the LO-phonon energy in GaAs. The observed effects are interpreted as manifestations of resonance intersubband polarons arising in the δ-layer upon reaching the $E_1(B_c) - E_0(B_c) = 2\hbar\omega_{LO}$ resonance. © *2000 MAIK "Nauka/Interperiodica".*

PACS numbers: 71.38.+i; 73.40.Gk; 73.61.Ey

Structures of the metal/δ-doped GaAs type are promising, although scantily studied, tunnel systems with a two-dimensional (2D) electron gas (2DEG). A self-consistent quantum well confining the 2D electron gas is formed in the vicinity of a metal/GaAs interface by doping one of the crystal planes of GaAs. Due to the self-consistent potential profile of a barrier near the Fermi level, the contribution of the interparticle interactions in δ-GaAs to the tunnel current can be enhanced, as compared to the structures with "rigid" barriers [1, 2]. However, up to now, the many-particle features have not been observed in the tunneling spectra of metal/δ-GaAs structures. Nor have these systems been studied in a quantizing magnetic field, although the separations between the 2D subbands in such a system are close to the energy $\hbar\omega_{LO}$ of the longitudinal optical (LO) phonons, which is favorable to the observation of a resonant polaron interaction occurring upon diamagnetic level shifting [3]. The threshold (resonance) polaron effects in polar semiconductors have been studied for quite a long time. In recent years, much attention has been given to the 2D systems, where these effect are expected to be more pronounced than in the 3D case [4]. As a rule, the resonance conditions in the 2D systems are achieved by applying a magnetic field perpendicular to the 2DEG layer, when the spacing between the Landau levels is a multiple of $\hbar\omega_{LO}$ (2D magnetopolaron). In recent years, the term-pinning and anticrossing effects, typical of magnetopolarons, were discovered in experiments with tunnel-resonance structures [5] and superlattices [6] and in structures with quantum wells [7] and quantum dots [8]. However, the intersubband resonance polarons in the structures with 2DEG have not as yet been reported. It is shown in this work that the 2D electrons in different subbands can resonantly interact with the LO phonons when the intersubband separation changes due to the diamagnetic shift of the size-quantization levels in tunnel Al/δ-GaAs structures. This has made possible the use of tunnel spectroscopy for the observation of the threshold polaron effects occurring in a 2DEG under conditions of intersubband resonance [3].

Samples and measurement techniques. Investigations were carried out with tunnel Al/δ-GaAs structures fabricated at the Institute of Radio Engineering and Electronics RAS by molecular-beam epitaxy (MBE). A δ-doped layer (Si) was situated 20 nm beneath the GaAs surface ($N_{Si} = 5.2 \times 10^{12}$ cm^{-2}; $N_a \approx 10^{15}$ cm^{-3} outside the δ-layer). After the completion of GaAs growth and a special procedure of cleaning the GaAs (100) surface from excessive As, the substrate was cooled for quite a long time to temperature $T < 100$°C. Then Al was sputtered onto the GaAs surface from the Knudsen cell directly in a MBE chamber. The tunneling Al/δ-GaAs junctions with 0.7-mm-diameter Al electrodes were fabricated by the photolitography technique. Ohmic contacts made from Au–Ge–Ni were alloyed to the δ layer at 400°C in an N_2 atmosphere.

The tunneling characteristics were taken from the potentiometric contacts. The junction differential resistance $R_d = dU/dI$ was 30–40 kΩ at $T = 4.2$ K and $U = 0$. The resistance between the ohmic contacts of the struc-

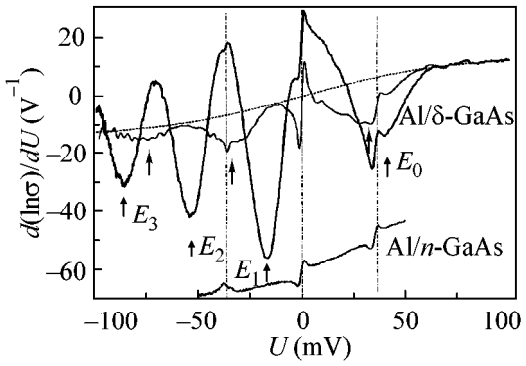

Fig. 1. The tunneling spectra $d(\ln\sigma)/dU$ measured at temperature 4.2 K for the tunneling junctions of Al/δ-GaAs [upper curves; B = 0 (heavy line) and 9.9 T (thin line)] and Al/*n*-GaAs (lower curve; shifted by –50 V^{-1}, B = 0). The dashed line is for the background curve $F(U)$. Magnetic field B is parallel to the δ-layer. The arrows indicate the positions of the 2D subbands of δ-GaAs in the tunneling spectra of the Al/δ-GaAs junctions. The vertical dash-and-dot lines indicate the many-particle features in the spectra (eU = 0 bias on the junction and $\pm\hbar\omega_{LO}$ = 36.5 meV).

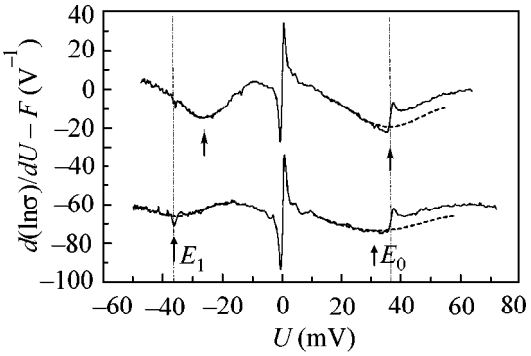

Fig. 2. The background [$F(U)$, see Fig. 1]-subtracted tunneling spectra of the Al/δ-GaAs junctions in a magnetic field B parallel to the δ-layer at T = 1.6 K. The upper curve is for B = 7.8 T, and the lower curve (shifted by –60 V^{-1}) is for B = 10.7 T. The arrows indicate the minima corresponding to the energies of the 2D subbands in the δ-layer. The vertical dash-and-dot lines indicate the bias voltages $eU = \pm\hbar\omega_{LO}$ = 36.5 meV. The dashed lines are the polynomials (of degree 3–5) approximating the spectra near the minima. In performing the least-squares polynomial fit to the E_0 dips, the neighborhoods of the phonon lines were eliminated from the approximation regions and the right edges were shifted downward by a distance equal to the "jump" in the LO-phonon lines (the difference between the dashed and solid lines).

ture did not exceed 2 kΩ. The tunneling spectra were measured by the standard method of modulation of the junction current at a frequency of f and the use of synchronous detection for recording the ac voltages proportional to dU/dI (at a frequency of f) and d^2U/dI^2 ($2f$).

The magnetic measurements were made in a superconducting solenoid ($B \le 15$ T) at the International Laboratory of High Magnetic Fields and Low Temperatures (Wrocław, Poland). The electron concentration in the δ-layer under the Al electrode was determined from the period of Shubnikov–de Haas-like oscillations of tunneling conductance at U = 0 in a magnetic field $B \parallel I$ and found to be 1.1×10^{12} cm^{-2}, which corresponded to the filling of only the lowest 2DEG subband.

Results. The tunneling spectrum (TS) of the Al/δ-GaAs junction at B = 0 and T = 4.2 K is shown in Fig. 1. The characteristic "dips" caused by size quantization in the δ-layer are clearly seen in the TS. The qualitative considerations suggest that the tunneling conductance $\sigma = dI/dU$ of a junction with 2DEG in one of the electrodes is the sum of the subband conductances $\sigma_i(U) \propto \rho_{\|i}(E_i, U)D(E_i, \mu - eU)$, where $\rho_{\|i} = (m/\pi\hbar^2)\theta(\mu - eU - E_i) - 2D$ is density of states, D is the barrier transmission, and μ is the Fermi energy. The minima in the tunneling spectrum $d(\ln\sigma)/dU$ on the eU scale correspond to the subband energies. Since U = 0 corresponds to the Fermi level in the semiconductor electrode, the minima at $U < 0$ (electron tunneling from the metal to the δ-layer) correspond to the unoccupied size-quantization levels, while the minima at $U > 0$ correspond to the filled levels. One can see from the TS at B = 0 that only a single (lowest) subband (i = 0) is filled in our samples. The Fermi energy of this subband is equal to ≈40 meV, in compliance with the data on the electron concentration $n = \mu(m/\pi\hbar^2)$ in the δ-layer ($n = 1.1 \times 10^{12}$ cm^{-2}). The 2D-subband energies derived from the TS at B = 0 are close to the results of self-consistent calculations [9] with the following parameters of the Al/δ-GaAs structure: barrier height Φ = 0.86 eV, distance between Al and the δ-layer L = 20 nm, $N_{Si} = 4.7 \times 10^{12}$ cm^{-2}, and $N_a = 5.5 \times 10^{15}$ cm^{-3}.

Many-particle features are also clearly visible in the spectrum of the tunneling junctions with the δ-layer: a zero-bias anomaly (ZBA) and phonon lines (PLs). Although these features are qualitatively similar in aspect to those for the uniformly doped tunnel structures (see the bottom curve in Fig. 1), their behavior with changing magnetic field is radically different and will be analyzed in detail elsewhere. For the Me/*n*-GaAs junctions, these features are usually related to the electron–electron interaction (ZBA [1, 2]) and the breaking of the electron dispersion law in GaAs for energies $E = \mu \pm \hbar\omega_{LO}$ because of the polaron interaction (PL [10]).

The minima in the TS undergo shifts (diamagnetic shift [11]) upon applying the magnetic field parallel to the 2DEG plane ($B \perp I$) (cf. the TS for B = 9.9 T in Fig. 1); i.e., the 2D subbands are expelled from the quantum well of the δ-layer [12]. Simultaneously, the dip magnitudes in the spectrum diminish. For this reason, it is desirable to eliminate the influence of a smooth background F (the dashed curve in Fig. 1) in the spectra, because it becomes substantial at high fields and, as follows from our data, is virtually independent of B. To a first approximation, the background is determined by the barrier transmission $D(\mu - eU)$ at the Fermi level.

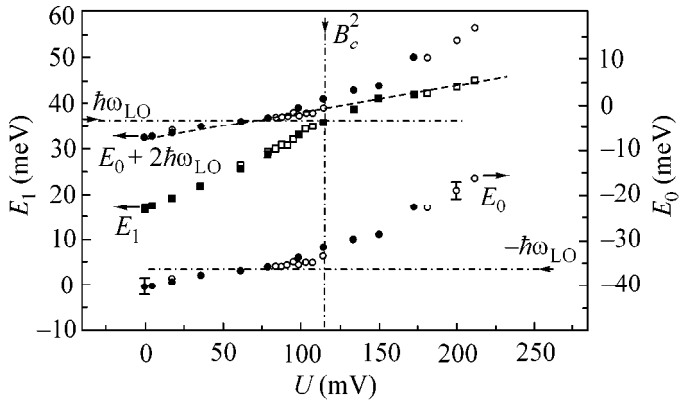

Fig. 3. The energies of the E_0 [T = (○) 1.6 and (●) 4.2 K] and E_1 [(□ 1.6 and (■) 4.2 K] subbands as functions of magnetic field B parallel to the δ-layer in the Al/δ-GaAs structure. The instrumental errors are given for the first and the last $E_0(B^2)$ points and correspond to the mark sizes for E_1. The energies are measured from the Fermi level of δ-GaAs. The small black and empty circles show the $E_0 + 2\hbar\omega_{LO}$ term. The vertical dash-and-dot line corresponds to the threshold field B_c.

The WKB calculation of the transmission at the Fermi level for a linear potential barrier without size quantization yields a simple formula for the tunnel current $I(U)$: $I \propto \exp(eU/E_{oo})(1 - \exp(-eU/\beta E_{oo})$, where $E_{oo} = 3/2(\Phi + \mu)^{0.5}(\hbar^2/2mL^2)^{0.5}$ and β is a dimensionless constant. The $F(U)$ function calculated with the use of this formula (for E_{oo} = 71 meV and β = 2) is presented in Fig. 1 and allows one to describe the behavior of the background. In what follows, the subband features are separated by subtracting the $F(U)$ curve from the measured spectra.

Figure 2 shows the background-subtracted tunneling spectra in the ranges of the lowest (i = 0) and the first excited (i = 1) subbands. These curves were used to determine the minimum positions $eU_i = -E_i$ as functions of magnetic field. To improve the accuracy of determining the minimum positions, the dips in the TS were approximated by polynomials of degree 3–5, as shown in Fig. 2. The errors in determining U_0 and U_1 from the TS were ±2 and ±0.5 mV, respectively. Note that the bottom of the lowest subband in our structures was located near the LO PL ($-E_o = eU_0 \approx \hbar\omega_{LO}$), whereas $E_1 < \mu + \hbar\omega_{LO}$ for B = 0 and achieved the value of $\mu + \hbar\omega_{LO}$ for $B_c \cong 11$ T (see Figs. 1, 2).

The resulting $E_i(B^2)$ functions for the two lowest subbands are shown in Fig. 3. The equality $E_i(B^2) = -eU_i(B^2)$ used above implies that the weak linear dependence of the level positions E_i on the bias on the junction is ignored. It follows from the self-consistent calculation for B = 0 that the inclusion of this dependence changes the initial slopes of $E_i(B^2)$ by no more than 10% toward their decrease and corrects the true level positions by several meV. The collisional level broadening in the δ-layers of our structures ($\hbar/\tau \approx$ 3–5 meV) and the errors in determining eU_i are of the same order of magnitude. However, strictly speaking, the curves presented in Fig. 3 reflect the behavior of the E_o and E_1 subbands as functions of B^2 for different biases near 40 and – 40 mV, respectively.

These functions are linear at weak magnetic fields; i.e., the levels undergo a standard diamagnetic shift [11, 13] $E_i = E_i(0) + (e^2B^2/2m)\Delta z_i^2$. In this expression, $\Delta z_i = (\langle z_i^2\rangle - \langle z_i\rangle^2)^{0.5}$ is the extent of the wave function in the z-direction perpendicular to the δ-layer for the ith subband at B = 0. The Δz_0 and Δz_1 values were determined from the initial slopes of the curves in Fig. 3 to give 5.6 and 11 nm ($m = 0.07m_0$), respectively.

The $E_o(B^2)$ and $E_1(B^2)$ dependences are drastically modified at magnetic fields above the critical field $B_c \cong 11$ T. One can see from Figs. 2 and 3 that the E_1 energy reaches the polaron feature (phonon line) in the tunneling spectrum at $B = B_c$. This corresponds to the $E_1 - E_0(k_F) = \hbar\omega_{LO}$ resonance of the Fermi-surface states with the bottom of the excited subband. Moreover, the $E_1 - E_o$ difference is close to twice the optical phonon energy. In our structures, the $E_1 - E_0 \cong 2\hbar\omega_{LO}$ condition is fulfilled near $B = B_c$ to within collisional level broadening and the accuracy of measuring E_1 and E_o. Consequently, one can expect that the threshold polaron effects (pinning and term anticrossing [14]) occur even in the systems with a weak electron–phonon coupling (coupling constant α = 0.07 for GaAs).

Indeed, the pinning of the E_1 subband at $B > B_c$ is clearly seen in Fig. 3. The asymptotic behavior of $E_1(B^2)$ at $B > B_c$ is described by the straight line with a slope coinciding with that for $E_o(B^2)$ in its low-field portion (see the dashed line for the $E_o + 2\hbar\omega_{LO}$ term in Fig. 3). It is known (see, e.g., [14, 15]) that the lowest-level (E_o) states in combination with the optical phonons dominate the new near-threshold polaron state at the E_1 level. In other words, the electron tunneling into the upper subband should "feel" the wave function of the lower state. It is this behavior which is demon-

strated by the data presented in Fig. 3. Therefore, the seed 2DEG spectrum is renormalized above the B_c threshold to account for the resonance 2D polaron. Note that the upper Landau level exhibits an analogous B dependence in the case of a 2D magnetopolaron, when the magnetic field is perpendicular to the 2DEG plane. According to calculations [15], the upper Landau level $(3/2)\hbar\omega_c$ should be pinned to the $(1/2)\hbar\omega_c + \hbar\omega_{LO}$ energy at $\hbar\omega_c > \hbar\omega_{LO}$, where $\omega_c = eB/m$ is the cyclotron frequency. In our case, an analogous dependence is observed for the magnetic field parallel to the 2DEG layer, with the $E_1(B)$ term pinning to the unperturbed energy of the $E_o(B) + 2\hbar\omega_{LO}$ term. Moreover, one can see from Fig. 3 that the shift of $E_o(B)$ by $2\hbar\omega_{LO}$ (small circles in Fig. 3) leads to the typical anticrossing pattern, also characteristic of the resonance polaron in a two-level system.

The above-threshold behavior of $E_o(B)$ likely reflects the fact that the effective mass in this subband increases with inclusion of the resonant electron–phonon interaction. As a result, the density of states increases and the Fermi energy lowers at a fixed 2DEG concentration in the δ-layer. Since, at present, the theory of the resonance intersubband polaron is lacking, the above-mentioned considerations have only a qualitative character. It should also be taken into account that the 2DEG in the system studied is strongly degenerate, whereas the magnetopolarons considered in [14, 15] are those for a one-electron system.

The data presented in this work suggest that the observed effects are mainly caused by the intersubband $E_1 - E_o = 2\hbar\omega_{LO}$ resonance, which is achieved because the diamagnetic shifts of the different 2D subbands in the δ-layer are different. A pinning at multiple frequencies ($2\omega_{LO}$) was predicted for a magnetopolaron in [14], while the resonance polaron effects involving two LO phonons were recently observed for a system of InAs quantum dots on GaAs [8]. However, the single-phonon resonance $E_1 - E_o(k_F) = \hbar\omega_{LO}$ may also be substantial in our case. To reveal the contributions of the single- and two-phonon processes, we are planning experiments on structures with lower or higher 2D-electron concentrations compared to our samples, when these resonances arise in different magnetic fields.

In summary, a qualitative picture of the effect observed in Al/δ-GaAs structures, on the whole, is consistent with the expected renormalization of the 2DEG spectrum under the conditions of resonant intersubband interaction of electrons with the LO phonons. Nevertheless, additional experiments and calculations are necessary for constructing the ultimate model for the intersubband resonance 2D polaron in δ-doped systems.

We are grateful to A.Ya. Shul'man and V.A. Volkov for helpful discussions, to V.G. Mokerov for attention to the work, and to V.I. Nizhankovskiĭ whose support and useful recommendations aided successful measurements. This work was supported by the Russian Foundation for Basic Research (project nos. 99-02-17592 and 00-02-17059) and the INTAS (grant no. 97-11475).

REFERENCES

1. I. N. Kotel'nikov, A. Ya. Shul'man, D. K. Maude, *et al.*, Pis'ma Zh. Éksp. Teor. Fiz. **60**, 849 (1994) [JETP Lett. **60**, 863 (1994)].
2. A. Ya. Shul'man and I. N. Kotel'nikov, in *Proceedings of the 12th International Conference on High Magnetic Fields in Semiconductors* (World Scientific, Singapore, 1997), p. 461.
3. I. N. Kotel'nikov and V. A. Volkov, in *Proceedings of the 7th International Symposium "Nanostructures: Physics and Technology," TP-07p* (St. Petersburg, 1999), p. 272.
4. A. Petrou and B. D. McCombe, in *Landau Level Spectroscopy*, Ed. by G. Landwehr and E. I. Rashba (North-Holland, Amsterdam, 1991), Chap. 12, p. 679.
5. G. S. Boebinger, A. F. J. Levi, S. Schmitt-Rink, *et al.*, Phys. Rev. Lett. **65**, 235 (1990).
6. R. K. Hayden, A. Nogaret, L. Eaves, *et al.*, Physica B (Amsterdam) **256–258**, 540 (1998).
7. G. D. Hai, F. M. Peeters, N. Studart, *et al.*, Phys. Rev. B **58**, 7822 (1998).
8. S. Hameau, Y. Guldner, O. Verzelen, *et al.*, Phys. Rev. Lett. **83**, 4152 (1999).
9. I. N. Kotel'nikov, V. A. Kokin, B. K. Medvedev, *et al.*, Fiz. Tekh. Poluprovodn. (St. Petersburg) **26**, 1462 (1992) [Sov. Phys. Semicond. **26**, 821 (1992)].
10. J. W. Conley and G. D. Mahan, Phys. Rev. **161**, 681 (1967).
11. D. C. Tsui, Solid State Commun. **9**, 1789 (1971).
12. A. Zrenner, H. Reisinger, F. Koch, *et al.*, Phys. Rev. B **33**, 5607 (1986).
13. F. Stern and W. E. Howard, Phys. Rev. **163**, 816 (1967).
14. I. B. Levinson and E. I. Rashba, Usp. Fiz. Nauk **111**, 683 (1973) [Sov. Phys. Usp. **16**, 892 (1973)].
15. F. M. Peeters and J. T. Devreese, Phys. Rev. B **31**, 3689 (1985).

Translated by V. Sakun

JETP Letters, Vol. 71, No. 9, 2000, pp. 391–394. Translated from Pis'ma v Zhurnal Éksperimental'noĭ i Teoreticheskoĭ Fiziki, Vol. 71, No. 9, 2000, pp. 570–575.

CONDENSED MATTER

Charge Oscillations in a Double Quantum Dot in the Coulomb Blockade Regime

V. A. Burdov

Lobachevskiĭ State University, Nizhni Novgorod, 603600 Russia

Received April 5, 2000

The two-electron dynamics in a symmetric double quantum dot placed in a constant electric field is considered. It is shown that, despite the Coulomb blockade, interdot electron-density oscillations are possible. In these oscillations, a charge equal to the charge of a single electron is periodically transferred from one quantum dot to the other. © *2000 MAIK "Nauka/Interperiodica".*

PACS numbers: 73.20.Dx; 03.65.-w

Studies of the electron properties in tunneling-coupled quantum dots are the subject of numerous recent works. In particular, the charge distribution in such systems [1–3] and the effect of constant external magnetic [3] and electric [2, 4] fields on the spectrum and the electron density were investigated. The time evolution of a one-electron wave packet in a double quantum dot and the periodic interdot charge oscillations were discussed in [5–7], and the experimental observation of these oscillations was reported in [8].

Generally speaking, in a system of coupled quantum dots (especially when the dimensions of the dots are as large as hundreds of nanometers), the number of electrons is much greater than one, which automatically leads to a Coulomb blockade of interdot tunneling and to the suppression of interdot charge oscillations. This work shows that, if the system is placed in a constant electric field, the charge oscillations are possible even in the Coulomb blockade regime, although only in a relatively narrow interval of field strengths.

We consider the simplest symmetric double quantum dot, namely, a system of two identical tunneling-coupled quantum dots of small dimensions (several nanometers [9, 10], which will allow us to obtain analytical results) with two electrons; the system is placed in a constant electric field **E** oriented along the structure axis (the *z*-axis). If the size of a quantum dot does not exceed several nanometers, the spacing between the dimensional quantization levels in an isolated quantum dot is on the order of 1 eV, which is almost an order of magnitude greater than the characteristic Coulomb energy of charge interaction at distances close to the quantum dot size ($\sim e^2/R$). In turn, the Coulomb energy also proves to be about an order of magnitude greater than both the tunnel level splitting Δ in a double quantum dot and the thermal energy (at room temperature).

In compliance with the latter condition, one can infer that the whole electron dynamics is confined to the two lowest one-electron levels $E_{0,1} = \pm\Delta/2$ that are formed due to electron ground-level splitting in an isolated quantum dot. We also assume that the electric field is not strong enough to cause level mixing with the higher energy states, and therefore we will use the two-level approximation.

The Hamiltonian of a two-electron system can be written as

$$\hat{H}(\mathbf{r}_1, \mathbf{r}_2) = \hat{H}_0(\mathbf{r}_1) + \hat{H}_0(\mathbf{r}_2) + e\mathbf{E}(\mathbf{r}_1 + \mathbf{r}_2) + \frac{e^2}{\epsilon|\mathbf{r}_1 - \mathbf{r}_2|}, \quad (1)$$

where $\hat{H}_0(\mathbf{r})$ is the one-particle two-level Hamiltonian of the double quantum dot, with eigenfunctions and eigenvalues $\chi_{0,1}(\mathbf{r})$ and $\pm\Delta/2$, respectively; ϵ is the dielectric constant of a medium; and e is the electron charge. It is natural to represent the wave function as an expansion in the two-electron basis consisting of four orthonormalized vectors (the spin part is omitted):

$$\Psi(\mathbf{r}_1, \mathbf{r}_2) = \sum_{i,j=0}^{1} C_{ij}\chi_i(\mathbf{r}_1)\chi_j(\mathbf{r}_2), \quad (2)$$

where C_{ij} are the constant expansion coefficients.

The one-electron functions $\chi_{0,1}(\mathbf{r})$ of the stationary states are symmetric and antisymmetric (with respect to z) functions having virtually identical spatial distributions: $\chi_0^2(\mathbf{r}) \approx \chi_1^2(\mathbf{r})$. The difference between the functions $\chi_0^2(\mathbf{r})$ and $\chi_1^2(\mathbf{r})$ is roughly determined by the ratio of the splitting Δ to the potential barrier height, which is on the order of 10^{-2} (e.g., for silicon dots in silicon dioxide [9]) or even less. Below, this difference is neglected.

The determination of the two-electron spectrum and the wave functions of the stationary states amounts to the calculation of the eigenfunctions (i.e., the coeffi-

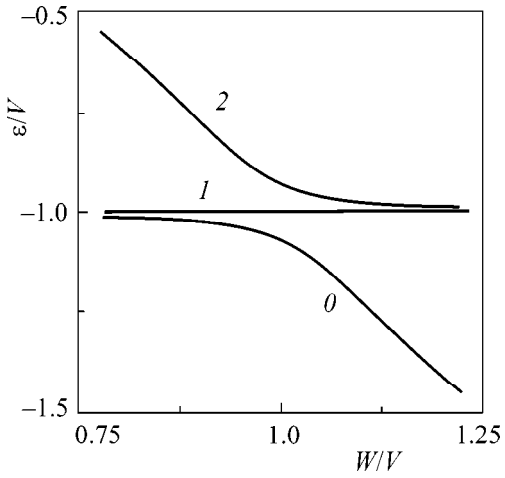

Fig. 1. Energies of the (*0*) ground, (*1*) first excited, and (*2*) second excited states for $\Delta/V = 0.1$.

cients C_{ij}) and the eigenvalues $\mathscr{E}$ of Hamiltonian (1). Using the standard procedure (see, e.g., [11]), we arrive at the following equation for the energy:

$$(\varepsilon + V)$$
$$\times [(\varepsilon + V)(\varepsilon - V)^2 - 4W^2(\varepsilon + V) - (\varepsilon - V)\Delta^2] = 0. \quad (3)$$

Here, $\varepsilon = \mathscr{E} - U$ and U and V are the pair (two-particle) matrix elements of the Coulomb operator $\hat{V} = e^2/\epsilon|\mathbf{r}_1 - \mathbf{r}_2|$, where $U = V_{00}^{00} = V_{11}^{11} = V_{11}^{00} = V_{00}^{11}$ and $V = V_{01}^{01} = V_{01}^{10} = V_{10}^{01} = V_{10}^{10}$ (the subscripts number the wave functions of electron no. 1, and the superscripts are for electron no. 2). The one-particle off-diagonal matrix element of the potential energy operator of an electron in an external electric field, denoted in Eq. (3) by W, is equal to eEz_{01}.

An analysis of Eq. (3) shows that (in the roughest approximation, the term containing Δ^2 can be ignored) the energy of the third excited state is separated from the zeroth and the first levels by a wide gap (on the order of $2V \sim e^2/R$), which increases with an increase in electric field. At temperatures below or close to room temperature, this level is unoccupied, so that we exclude it from consideration. By contrast, the energy of the second excited state decreases with increasing electric field and closely approaches the two lower levels in the vicinity of the point $W = V$, resulting in the formation of a set of three levels that can be populated. Let us consider in more detail the behavior of the energies and wave functions of the stationary states near this point.

Setting small deviations of W and ϵ from V and $-V$, respectively, and taking into account the smallness of Δ relative to V, we reduce the fourth-degree equation to a third-degree one that separates into linear and quadratic equations. As a result, we obtain the following expressions for the three lowest energy states:

$$\mathscr{E}_1 = U - V,$$
$$\mathscr{E}_{0,2} = U - W \mp \sqrt{(W - V)^2 + \Delta^2/2}. \quad (4)$$

The expression for $\mathscr{E}_1$ is exact. Figure 1 shows the energy branches corresponding to the first three states as functions of the ratio W/V proportional to the external electric field strength. One can see that the energy branches of the ground state and the second excited state look as if they were repelled from each other (the so-called avoided level anticrossing), asymptotically approaching the branch of the first excited state at $V - W \gg \Delta$ and $W - V \gg \Delta$, respectively.

The wave functions of the ground state and the two excited states take the form

$$\Psi_0(\mathbf{r}_1, \mathbf{r}_2) = \frac{\sin\alpha}{\sqrt{2}}[\chi_0(\mathbf{r}_1)\chi_0(\mathbf{r}_2) - \chi_1(\mathbf{r}_1)\chi_1(\mathbf{r}_2)]$$
$$+ \frac{\cos\alpha}{2}[\chi_0(\mathbf{r}_1)\chi_0(\mathbf{r}_2) + \chi_1(\mathbf{r}_1)\chi_1(\mathbf{r}_2)$$
$$- \chi_0(\mathbf{r}_1)\chi_1(\mathbf{r}_2) - \chi_1(\mathbf{r}_1)\chi_0(\mathbf{r}_2)],$$
$$\Psi_1(\mathbf{r}_1, \mathbf{r}_2) = \frac{\chi_0(\mathbf{r}_1)\chi_1(\mathbf{r}_2) - \chi_1(\mathbf{r}_1)\chi_0(\mathbf{r}_2)}{\sqrt{2}}, \quad (5)$$
$$\Psi_2(\mathbf{r}_1, \mathbf{r}_2) = \frac{\cos\alpha}{\sqrt{2}}[\chi_0(\mathbf{r}_1)\chi_0(\mathbf{r}_2) - \chi_1(\mathbf{r}_1)\chi_1(\mathbf{r}_2)]$$
$$- \frac{\sin\alpha}{2}[\chi_0(\mathbf{r}_1)\chi_0(\mathbf{r}_2) + \chi_1(\mathbf{r}_1)\chi_1(\mathbf{r}_2)$$
$$- \chi_0(\mathbf{r}_1)\chi_1(\mathbf{r}_2) - \chi_1(\mathbf{r}_1)\chi_0(\mathbf{r}_2)],$$

where the angle α is determined by the relationships

$$\cos 2\alpha = \frac{W - V}{\sqrt{(W - V)^2 + \Delta^2/2}},$$
$$\sin 2\alpha = \frac{\Delta/\sqrt{2}}{\sqrt{(W - V)^2 + \Delta^2/2}}$$

and varies from zero to $\pi/2$ as the difference $W - V$ varies from $+\infty$ to $-\infty$.

According to Eqs. (5), the wave functions of the ground state and the second excited state are symmetric with respect to the particle permutation and depend on the strength of the applied electric field, in contrast to the antisymmetric function of the first excited state (the corresponding expression is rigorous, as is the expression for the energy $\mathscr{E}_1$). The energies of these states also depend on the external field, unlike the energy of the first excited state.

The fact that the energy and the wave function of the first excited state are independent of the electric field is explained by the use of the two-level one-electron

approximation, which yields only four two-electron states, three of them being symmetric (it can be readily shown that the third excited state is also symmetric) and one antisymmetric. Due to the particle identity principle, the wave function of a system placed in an external electric field should also be either strictly symmetric or strictly antisymmetric. Hence, it is clear that, in an external field, the symmetric states can be composed of only symmetric states (e.g., corresponding to the zero electric field) and the antisymmetric states, of only antisymmetric ones. Since there is only a single antisymmetric state, it remains unchanged and retains its energy in a varying external field.

Now, we proceed to considering the time evolution of a wave packet having the form of a superposition of three states (5) with certain constant expansion coefficients $\rho_j \exp(i\varphi_j)$:

$$\Psi(\mathbf{r}_1, \mathbf{r}_2, t) = \sum_{j=0}^{2} \rho_j \Psi_j(\mathbf{r}_1, \mathbf{r}_2) \exp\left\{-i\left(\frac{\mathscr{E}_j}{\hbar}t - \varphi_j\right)\right\}. \quad (6)$$

The quantities ρ_j^2 specify the occupation probability for the jth level.

Using the wave function (6), we determine the charge in each quantum dot as a function of time. To be definite, we calculate the charge in the left quantum dot $Q_L(t)$. For this purpose, we take the integral of a one-particle distribution density over the region $z < 0$ and multiply it by $-2e$.

Using Eqs. (5) for the wave functions, we arrive at the following expression for the charge:

$$\begin{aligned} Q_L(t) &= -e\{1 + \rho_0^2 \cos\alpha + \rho_2^2 \sin^2\alpha \\ &\quad - \rho_0\rho_2 \sin 2\alpha \cos(\nu t + \varphi_0 - \varphi_2)\}. \end{aligned} \quad (7)$$

As one can see from this expression (7), the charge periodically oscillates between the two quantum dots with the frequency ν coinciding with the frequency of transition from the ground state to the second excited state ($0 \longrightarrow 2$):

$$\nu = \frac{\mathscr{E}_2 - \mathscr{E}_0}{\hbar} = \frac{2}{\hbar}\sqrt{(W-V)^2 + \Delta^2/2}, \quad (8)$$

and with the amplitude

$$Q = e\rho_0\rho_2 \sin 2\alpha. \quad (9)$$

Both these quantities depend on the external electric field.

According to Eqs. (7) and (8), the charge oscillations in a double quantum dot are purely harmonic. The first excited state contributes almost nothing to the charge oscillations, and the frequencies corresponding to the quantum transitions $0 \longrightarrow 1$ and $1 \longrightarrow 2$ do not manifest themselves. The effect of the first excited state is significant only for ρ_0 and ρ_2 because of the normalization condition $\rho_0^2 + \rho_1^2 + \rho_2^2 = 1$.

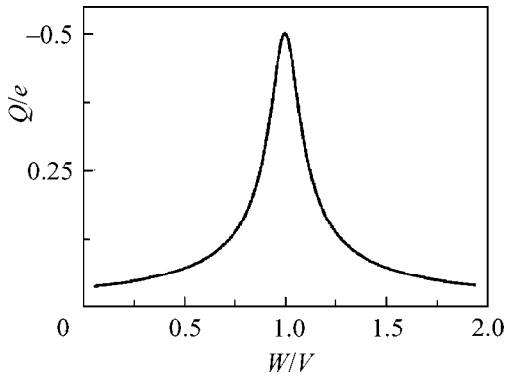

Fig. 2. Amplitude of charge oscillations (in units of electron charge e) for $\Delta/V = 0.1$ and $\rho_0 = \rho_2 = 1/\sqrt{2}$; $\rho_1 = 0$.

This result is explained by the difference in the symmetry of the wave functions of the first excited state and all other states with respect to the particle permutations. When the interaction operator is strictly symmetric, the symmetry of the wave function cannot be changed by the given perturbation and, hence, the states with different symmetries cannot be coupled by a symmetric action. The presence of frequencies corresponding to the transitions $0 \longrightarrow 1$ or $1 \longrightarrow 2$ in the charge oscillations would mean that, at these frequencies, emission or absorption of energy quanta is possible, which would result in the transitions from the symmetric states of the system to the antisymmetric ones and vice versa.

As for the amplitude of the charge oscillations in Eq. (9), it is determined by the initial populations of the ground and second excited stationary states, as well as by the parameters of the system and (as was mentioned above) by the external electric field strength.

Evidently, the most favorable situation for the appearance of the interdot oscillations of electron density will occur when the populations of the zeroth and the second levels are be equal and the population of the first level is be zero. In this case, the product $\rho_0\rho_2$ will be maximum and equal to 0.5.

The dependence of the oscillation amplitude on the matrix element ratio W/V, i.e., on the external electric field strength, is shown in Fig. 2 for $\rho_0 = \rho_2 = 1/\sqrt{2}$. This dependence has a pronounced Lorentz-type resonance structure. The greatest oscillation amplitude is reached precisely at the anticrossing point $W = V$ and is equal to $e/2$, i.e., half the electron charge (by contrast, the oscillation frequency is minimal and equal to $\Delta\sqrt{2}/\hbar$ at this point). Hence, the total charge in the left quantum dot will periodically vary by one electron charge, i.e., between $-e$ and $-2e$.

The characteristic width of the resonance peak is determined by the level splitting energy Δ; since (as was mentioned above) $\Delta \ll V$, this peak proves to be rather narrow on the W/V axis. When the quantity W increases so that the condition $|W - V| \sim \Delta$ fails, the

amplitude of the oscillations sharply decreases; and, in the region where $|W - V| \gg \Delta$, the charge oscillations are virtually absent. As a result, the static charge distribution among the quantum dots is established in such a way that a charge of $-3e/2$ is concentrated in the left dot and a charge of $-e/2$ in the right dot.

Let us clarify the particular role of the anticrossing point $W = V$. For this purpose, we set $\rho_2 = 0$ and $\rho_0 = 1$ in Eq. (7) and consider the charge variation in the left dot as a function of W. If the electric field is not too strong, $W < V$ and $|W - V| \gg \Delta$; the angle α is close to $\pi/2$; and, hence, the electrons are in the different quantum dots. From Eq. (7) it follows that, as the quantity W passes through the anticrossing point ($W > V$) and away from it ($|W - V| \gg \Delta$), both charges are transferred to the left quantum dot and remain there. [For the second excited state, if we set $\rho_2 = 1$ and $\rho_0 = 0$ in Eq. (7), an inverse transition takes place]. Therefore, the value of W coinciding with V corresponds to the electric field strength "removing" the Coulomb blockade of electron tunneling from one quantum dot to the other.

Thus, in the case $W < V$ and the ground state, the electric field "confines" the electrons in different quantum dots, while, in the second excited state, the electrons are confined in the left quantum dot. In the case $W > V$, the situation is reversed. Only in a narrow interval of the electric field strengths corresponding to the condition $|W - V| \ll \Delta$ does a kind of mutual compensation of the Coulomb interaction and the effect of the external electrostatic field take place, which leads to free oscillations of the electron density in the double quantum dot.

Estimates show that the external electric field strength necessary to satisfy the condition $W = V$ is about 10^5 V/cm, and the width of the transition region within which charge oscillations take place is an order of magnitude less.

REFERENCES

1. J. Q. You and H.-Z. Zheng, Phys. Rev. B **60**, 8727 (1999).
2. S. Nagaraja, J.-P. Leburton, and R. M. Martin, Phys. Rev. B **60**, 8759 (1999).
3. H. Imamura, P. A. Maksym, and H. Aoki, Phys. Rev. B **59**, 5817 (1999).
4. G. W. Bryant, Phys. Rev. B **48**, 8024 (1993).
5. N. Tsukada, M. Gotoda, and M. Nunoshita, Phys. Rev. B **50**, 5764 (1994).
6. N. Tsukada, M. Gotoda, M. Nunoshita, and T. Nishino, Phys. Rev. B **52**, 17005 (1995).
7. C.-K. Wang, I. Yakymenko, I. V. Zozoulenko, and K.-F. Berggren, Phys. Rev. B **57**, 2632 (1998).
8. R. H. Blick, D. W. van der Weide, R. J. Hang, and K. Eberl, Phys. Rev. Lett. **81**, 689 (1998).
9. Q. Ye, R. Tsu, and E. H. Nicollian, Phys. Rev. B **44**, 1806 (1991).
10. A. D. Andreev and A. A. Lipovskiĭ, Phys. Rev. B **59**, 15402 (1999).
11. L. D. Landau and E. M. Lifshitz, *Quantum Mechanics: Non-Relativistic Theory* (Nauka, Moscow, 1989, 4th ed.; Pergamon, Oxford, 1977, 3rd ed.).

Translated by E. Golyamina